JSCSEN 74(6)707–845(2009)

Journal of the Serbian Chemical Society

Electronic version

VOLUME 74

No 7

BELGRADE 2009

Available on line at

www.shd.org.rs/JSCS

The full search of JSCS is available through

DOAJ DIRECTORY OF OPEN ACCESS JOURNALS

www.doaj.org

Journal of the Serbian Chemical Society
JSCS@tmf.bg.ac.rs • www.shd.org.rs/JSCS

J. Serb. Chem. Soc. Vol. 74, No. 7 (2009)

CONTENTS

Published by the Serbian Chemical Society
Karnegijeva 4/III, 11000 Belgrade, Serbia
Printed by the Faculty of Technology and Metallurgy
Karnegijeva 4, P.O. Box 35-03, 11120 Belgrade, Serbia

Journal of the Serbian Chemical Society
JSCS@tmf.bg.ac.rs • www.shd.org.rs/JSCS

J. Serb. Chem. Soc. 74 (7) 707–716 (2009)
JSCS–3869

UDC 618.36+612.6:612.349.8:576.314
Original scientific paper

IGFBP-1 forms associated with placental cell membranes

ROMANA MASNIKOSA*#, BOGOVID ŽIVKOVIĆ and OLGICA NEDIĆ#

INEP-Institute for the Application of Nuclear Energy, University of Belgrade, Banatska 31 b, 11080 Belgrade, Serbia

(Received 9 March, revised 7 April 2009)

Abstract: Fetal growth *in utero* depends on the proper development and function of the placenta. Insulin-like growth factors (IGFs) are critically involved in placental development. During pregnancy, an IGF-binding protein, IGFBP-1, which is produced by maternal decidua, plays an important role in the control of the bioavailability of IGFs. It has recently been proposed that cleavage of decidual IGFBP-1 by matrix metalloproteases is a novel mechanism in the control of placental development. The presence of IGFBP-1 in solubilized placental cell membranes, *i.e.* its association with the membranes, was detected in an earlier work. Herein, it is shown that IGFBP-1 from the solubilized membranes forms dimers, as well as high molecular mass complexes. IGFBP-1 dimers preferably contain the non-phosphorylated form of IGFBP-1. The high molecular mass forms are polymers of IGFBP-1 or its complexes with other membrane proteins. Dimerization of IGFBP-1, together with its association with the placental cell membrane, could serve as an additional mechanism of the regulation of IGF availability to the type 1 IGF receptors.

Keywords: IGFBP-1 dimers; placenta; IGFBP-1 phosphoisoforms.

INTRODUCTION

The insulin-like growth factor (IGF) axis is an important regulator of fetal growth and it has been suggested that IGF-I and -II may, in part, mediate this effect by promoting proper placental development and function.[1] For IGFs to exert their effects, they must interact with cell-surface receptors, principally the type 1 IGF receptor (IGF1R).[2] IGF-II can also bind to the type 2 IGF receptor (IGF2R) and insulin receptor isoform A (IR-A).[2] Ligand access to these receptors is controlled by a family of six IGF binding proteins (IGFBPs 1–6).[2,3] IGFBPs have similar or higher affinities for IGFs than IGF1R, suggesting that the formation of IGF–IGFBP complexes is favored over the formation of IGF–IGF1R complexes. Acting through this mechanism, IGFBPs would sequester

* Corresponding author. E-mail: romana@inep.co.rs
# Serbian Chemical Society member.
doi: 10.2298/JSC0907707M

IGFs and act as inhibitors of IGF actions.[4] In certain physiological situations, IGFBPs can enhance biological actions of IGFs, which was shown for IGFBP-3.[3] However, there are many physiological situations (*e.g.*, pregnancy), in which IGFs must be released from IGFBPs, principally through decreasing their affinities for IGFs. This could be realized by the binding of IGFBPs to extracellular matrix components or by post-translational modifications of IGFBPs.[4]

Immunohistochemical studies showed IGFBP-2 in the syncityotrophoblast cells of the placenta.[5] IGFBP-1 and IGFBP-3 are produced in abundance by the maternal–fetal interface.[5] IGFBP-1 was found to associate with the membrane of placental trophoblast cells.[6] It is thought that IGFBP-1 regulates the biological activity of IGFs within the local environment of the human placenta by modulating their interaction with the IGF1R.[7] The role of IGFBP-1 in the placenta is not yet elucidated and the mechanisms involved are under vigorous research. Post-translational modifications, including phosphorylation,[8] proteolysis,[9] and polymerization,[10] have been shown to alter the affinity of IGFBP-1 for IGF-I. Three phosphorylation sites have been identified in human IGFBP-1: Ser 101, 119 and 169.[11] When human IGFBP-1 purified from amniotic fluid or a cell culture supernatant is analyzed by non-denaturing gel electrophoresis, one non-phosphorylated (np-IGFBP-1) and four phosphorylated isoforms (p-IGFBP-1) can be identified.[12] In the circulation of non-pregnant women, IGFBP-1 almost exclusively exists as p-IGFBP-1, which has high affinity for IGFs. During pregnancy, however, IGFBP-1 becomes dephosphorylated by placental alkaline phosphatase to np-IGFBP-1 and lesser phosphorylated isoforms, which have a reduced affinity for IGF-I. Whereas p-IGFBP-1 is inhibitory, np-IGFBP-1 stimulates the action of IGF-I.[8]

Sakai and co-workers[10] demonstrated the formation of covalently linked multimers of IGFBP-1 by a tissue transglutaminase *in vitro*, as well as by a fibroblast membrane extract. They also detected the polymerized forms of IGFBP-1 in human amniotic fluid. These findings prompted the herein described examination of the association/polymerization of the IGFBP-1 protein associated with placental cell membranes.

EXPERIMENTAL

Materials

$Na^{125}I$ was supplied by Isotope (Budapest, Hungary). Human IGF-I and des(1–3)IGF-I (IGF-I lacking the three amino acid residues at the *N*-terminus) were from GroPep (Adelaide, Australia). Affinity purified goat polyclonal anti-human IGFBP-1 antibodies were from DSL (Webster, USA). Horse radish peroxidase-conjugated (HRP) anti-goat IgG was supplied by Biosource (Camarillo, USA). Enhanced chemiluminescence (ECL) detection reagents were the products of Amersham Biosciences (Aylesbury, UK) and MXB films and developing reagents were from Kodak (Paris, France). All other chemicals were purchased from Sigma-Aldrich (Steinheim, Germany). ^{125}I–IGF-I and ^{125}I–des(1–3)IGF-I were prepared using the chloramine T method.[13]

Human placental tissue was obtained from uncomplicated pregnancies at term, according to protocols approved by the local ethical committee. The tissue was collected in ice cold 0.10 M phosphate buffered saline (pH 7.4) and brought to laboratory within 60 min. After washing the placenta free of blood, the amniotic and chorionic membranes were dissected away. The placental tissue was minced and homogenized in a 0.25 M sucrose solution with protease inhibitors. After a short centrifugation to remove the cell debris, the supernatant was centrifuged at 18000 x *g* for 30 min. The pellet was resuspended and solubilized by Triton X-100. The solubilized membranes were recovered in the supernatant after centrifugation at 100,000 x *g* for 90 min. The detailed procedure was described in a previous article.[14]

Gel filtration

Solubilized membranes (2 mg of membrane protein) were incubated with ^{125}I–IGF-I or ^{125}I–des(1–3)IGF-I (1 pmol, 10^6 cpm) at 4 °C overnight. In some cases, the solubilized membranes were incubated with the tracers in the presence of high concentrations of unlabeled IGF-I or des(1–3)IGF-I (4 μg). The samples were then subjected to gel filtration on a Sephadex G-100 column, exactly as described previously.[15] In some cases, the solubilized membranes (45 mg of membrane proteins) were applied on the column without prior incubation with the tracer and the collected fractions were employed in electrophoresis and in binding assays with ^{125}I-labeled IGF-I and des(1–3)IGF-I. In a separate experiment, fractions from 9 to 15 were pooled and the pool was designated as peak 1 proteins. The binding assays commenced by incubating aliquots (50 μL) of the fractions obtained after gel filtration with ^{125}I–IGF-I or ^{125}I–des(1–3)IGF-I (10^5 cpm) and were performed as described earlier.[16] The protein concentrations were determined using the Bradford protein assay[17] with ovalbumin standards.

Gel electrophoresis and blotting

Aliquots of the fractions obtained from gel filtration were subjected to both non-reducing sodium dodecyl sulfate-polyacrylamide gel electrophoresis (SDS PAGE, in 8 % gel) and to non-denaturing PAGE (in 10 % gel). The samples were mixed with an equal volume of sample buffer (0.125 M Tris-HCl, 4 % SDS, 20 % glycerol, 0.010 % bromphenol blue, pH 6.8) and boiled for 7 min before being applied onto the gels. The non-denaturing PAGE was performed following the procedure for SDS PAGE,[18] except that the SDS was omitted from all the buffers, including the sample buffer. The proteins were transferred to Immobilon P membranes (Millipore, Billerica, USA) and probed with anti-human IGFBP-1 antibodies as described previously.[18] The immunoreactive proteins were visualized using HRP-conjugated anti--goat IgG antibodies and an ECL detection system, followed by autoradiography. Before the ligand blotting, the solubilized membranes and peak 1 proteins were subjected to SDS PAGE using an 8 % gel and then the membranes were probed with ^{125}I–IGF-I (2.5×10^6 cpm in 50 mL of 0.010 M Tris-HCl, 0.15 M NaCl, pH 7.4) and visualized by autoradiography as described previously.[19]

Immunoradiometric assay (IRMA) of IGFBP-1

The IGFBP-1 concentration in the fractions eluted from the Sephadex G-100 column was determined by a DSL (Webster, USA) Total IGFBP-1 IRMA kit.

RESULTS AND DISCUSSION

The proteins which interacted with ^{125}I–IGF-I and with ^{125}I–des(1–3)IGF-I were detected after separation by gel filtration of the solubilized placental cell membranes pre-incubated with the tracers (Fig. 1). The first peak (peak 1), which

appears at the void volume (V_0) of the column, is known to contain complexes of IGF1R with ^{125}I-labeled IGF-I or des(1–3)IGF-I, whereas the second peak contains ^{125}I–IGF-I/IGFBP-1 complexes.[15] Peak 2 is missing in the elution profile of the solubilized membranes pre-incubated with ^{125}I–des(1–3)IGF-I, because it has a markedly reduced affinity for IGFBPs.[20] Peak 3 represents unbound ^{125}I--labeled ligand.

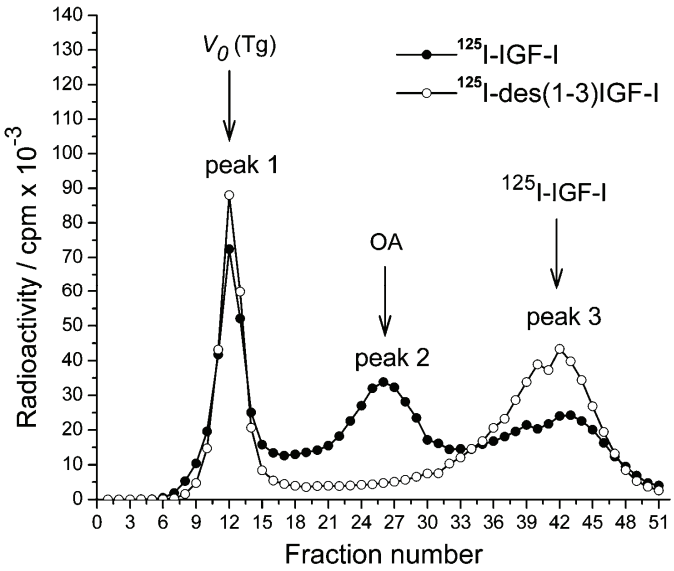

Fig. 1. Two identical samples of solubilized membranes (2 mg of total membrane protein) were incubated with 1×10^6 cpm of ^{125}I–IGF-I (full circles) and ^{125}I–des(1–3)IGF-I (empty circles) before being applied to a Sephadex G-100 column ((1.8×60) cm) and eluted using 0.050 M sodium phosphate buffer, pH 7.5, containing 0.10 M NaCl and 0.10 % Triton X-100. The flow rate was 20 mL/h. Following the pre-elution of 20 mL, 2 mL fractions were collected and the radioactivity in each was measured. The positions of molecular mass markers (Tg-thyroglobulin, OA-ovalbumin) are indicated. The results from representative experiments are illustrated.

The specificity of ligand binding to peak 1 and peak 2 proteins was analyzed by gel-filtration of the solubilized membranes, which were pre-incubated with ^{125}I-labeled ligands in the presence of high concentrations of unlabeled ligands. The ^{125}I–des(1–3)IGF-I binding in peak 1 was specific, as this peak disappeared upon gel filtration in the presence of 4 μg of either unlabeled IGF-I or des(1––3)IGF-I (results not shown). This pattern of cross-reactivity reflects the fact that des(1–3)IGF-I binds to IGF1R with a similar affinity to the full length IGF-I.[21] In contrast, ^{125}I–IGF-I bound to the proteins in peak 1 could not be completely displaced by unlabeled des(1–3)IGF-I, whereas unlabeled IGF-I reduced the binding of the ligand to the level of non-specific binding (Fig. 2). In other words, a

proportion of ^{125}I–IGF-I binds to the protein(s) of peak 1 to which des(1–3)IGF-I does not bind.

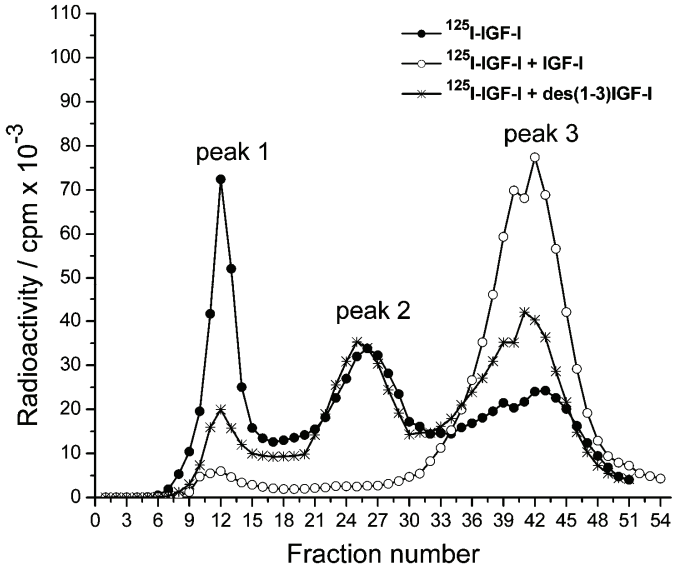

Fig. 2. Solubilized membranes (2 mg of total membrane protein) were incubated with 1×10^6 cpm of ^{125}I–IGF-I, without competing ligand (full circles) or in the presence of unlabeled competitor: IGF-I (empty circles), des(1–3)IGF-I (asterisks), applied to a Sephadex G-100 column and eluted as described (see legend under Fig. 1).

To investigate whether IGFBP-1 was also present among the proteins of high molecular mass in peak 1, the concentration of IGFBP-1 in the fractions eluted after chromatography of 45 mg of solubilized membrane proteins was measured immunoradiometrically. The results are shown in parallel with the graph that represents the binding of ^{125}I–IGF-I in fractions eluted after the preparative gel filtration (Fig. 3). The highest IGFBP-1 concentrations, according to the DSL Total IGFBP-1 IRMA, were detected in fractions 24–28, with the maximal value in fraction 26 (above 230 ng/mL), coinciding with peak 2. Fractions that belonged to peak 1 also contained IGFBP-1. In other words, IGFBP-1 eluted within V_0, among the other high molecular mass proteins, such as IGF1Rs, IGF2Rs and IRs.[14]

To examine the possibility that IGFBP-1 from placental cell membranes existed in the form of a high molecular mass species, the fractions of peak 1 and peak 2 were analyzed by SDS PAGE, followed by immunoblotting using affinity purified polyclonal anti-human IGFBP-1 antibodies (Fig. 4). Several molecular forms of IGFBP-1 from the solubilized placental cell membranes were visible on the immunoblots (Fig. 4). The 60 kD-band on the blot in Fig. 4 most probably originated from dimeric IGFBP-1, which peaked in fractions 18 to 21. The existence of covalently linked monomers of IGFBP-1, which formed dimers follow-

ing exposure to pure tissue transglutaminase, was reported.[10] Monomeric IGFBP-1 (molecular mass of 29 kD) bands were seen at the bottom of the gel, with the greatest abundance in fractions eluting after fraction 21. Some of these fractions also showed the greatest IGFBP-1 concentration in IRMA (Fig. 3). However, the concentration of IGFBP-1 in the fractions in which IGFBP-1 was present mostly as a dimer was low. In other words, the antibodies used in IRMA poorly recognized the dimeric IGFBP-1 forms. According to the immunoblot in Fig. 4, high molecular mass proteins (of approximately 150 and 220 kD) that were immunoreactive with anti-IGFBP-1 antibodies were also detected (gel filtration fractions 12 to 15). These proteins are either polymers of IGFBP-1 or its complexes with other proteins from placental cell membranes.

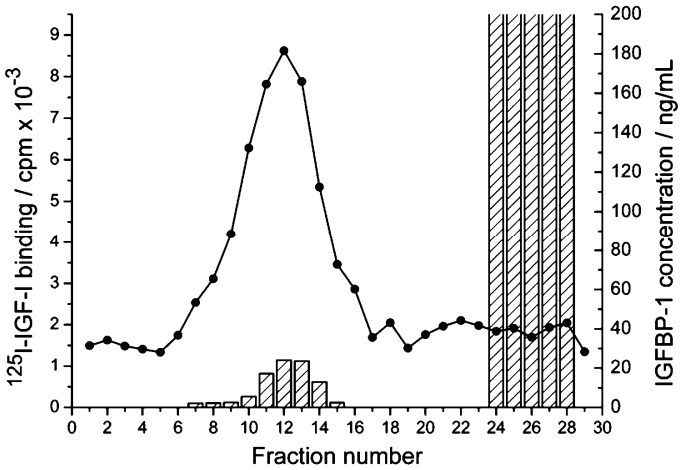

Fig. 3. Solubilized membranes (45 mg of total membrane protein) were chromatographed on a Sephadex G-100 column as usual, but without pre-incubation with ^{125}I–IGF-I. The binding of ^{125}I–IGF-I in each fraction was measured by ligand binding assay. The result from a representative experiment is illustrated. The concentration of IGFBP-1 in the fractions, measured by DSL Total IGFBP-1 IRMA, is shown in parallel (ng/mL).

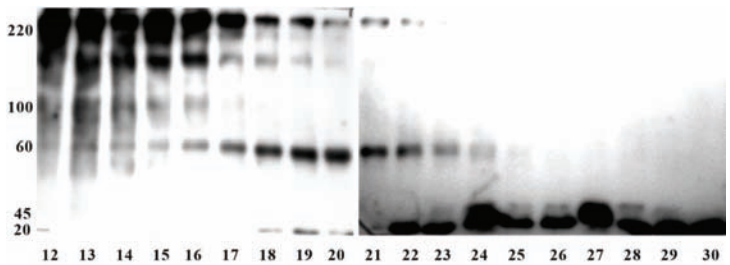

Fig. 4. The fractions eluted from the Sephadex G-100 column were analyzed by SDS PAGE (8 % gels) followed by immunoblotting using affinity purified goat polyclonal anti-human IGFBP-1 antibodies. The blots are of two gels that were run simultaneously in one electrophoretic unit. Molecular mass markers (in kD) are shown on the left.

A further step was to check whether np-IGFBP-1 and p-IGFBP-1 were differently distributed between the peak 1 and peak 2 proteins. Non-denaturing PAGE followed by immunoblotting for IGFBP-1 was undertaken to analyze the phosphoisoform pattern of IGFBP-1 in the fractions eluted after gel filtration (Fig. 5). The results presented in Fig. 5 clearly show that the fractions contained different isoforms of IGFBP-1. The band positions of p- and np-IGFBP-1 isoforms upon non-denaturing PAGE were established knowing that the phosphorylated forms, due to their charge density, migrate towards the anode faster than the np-IGFBP--1.[22] The same pattern of bands was obtained by others upon non-reducing PAGE of IGFBP-1 from human amniotic fluid.[22,23] np-IGFBP-1 was mostly present in fractions number 18 to 21, which were the same fractions that contained the dimeric form of IGFBP-1 (see Fig. 4). These results strongly suggest that the dimeric form of IGFBP-1, associated with the placental cell membranes, consists almost exclusively of the np-IGFBP-1 isoform. These findings are in accordance with those obtained by others, who observed that np-IGFBP-1 polymerized more rapidly and to a greater extent than phosphorylated isoforms.[10] Monomeric IGFBP-1, however, mostly contained phosphorylated isoforms of IGFBP-1 (fractions 24 to 28). Fraction 26, which had the greatest amount of IGFBP-1 in IRMA and which bound the most ^{125}I-labeled IGF-I when pre-incubated with the tracer (see Fig. 1), showed the strongest bands on the immunoblots following non-denaturing electrophoresis.

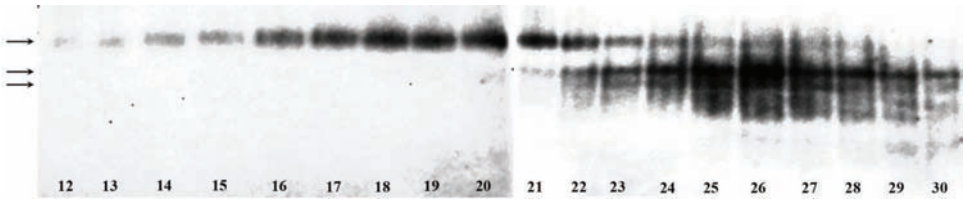

Fig. 5. The fractions eluted from the Sephadex G-100 column were applied to two 10 % gels, which were simultaneously subjected to non-denaturing PAGE, and then to immunoblotting for IGFBP-1. The upper arrow denotes the position of np-IGFBP-1. The two lower arrows indicate the positions of the phosphorylated isoforms of IGFBP-1.

The ligand binding properties of IGFBP-1 forms were also examined in this study. The affinity of IGFBP-1 isoforms present in the solubilized placental membranes and in peak 1 for ^{125}I-labeled IGF-I was assessed using ligand blot. As can be seen in Fig. 6, the monomeric IGFBP-1 was the only protein able to bind ^{125}I–IGF-I, giving a strong single band. The binding of ^{125}I-labeled IGF-I to the IGFBP-1 dimer or to some other high molecular mass proteins could not be demonstrated. The binding of the tracer to IGF1R was also lacking. It is generally believed that polymeric forms of IGFBP-1 do not bind the ligand,[10] but some of the present results indicate that a proportion of ^{125}I–IGF-I bound to the

protein(s) of peak 1 to which des(1–3)IGF-I did not bind, most probably IGFBP-1. Although the ligand blot result suggests the monomeric form of IGFBP-1 as the sole molecular species able to bind the ligand, the technique might not be as sensitive as gel filtration of the pre-labeled placental membrane proteins.

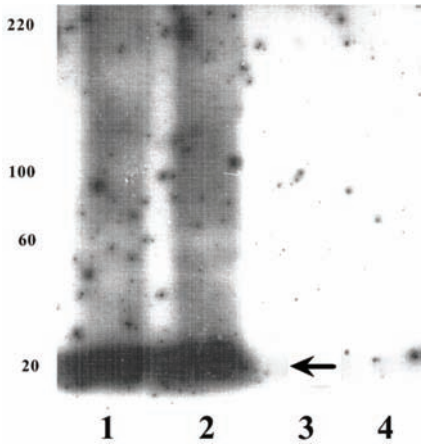

Fig. 6. The solubilized placental membrane proteins and proteins eluted in peak 1 after gel filtration on Sephadex G-100 were analyzed by 8 % SDS PAGE followed by ligand blotting using ^{125}I–IGF-I. Lanes 1 and 2 contained solubilized membranes and lanes 3 and 4, peak 1 proteins (pooled fractions 9 to 15 from preparative gel filtration). Molecular mass markers (in kD) are shown on the left. The arrow denotes the position of monomeric IGFBP-1.

These results are in accordance with those presented in Fig. 1, where fractions containing dimers of IGFBP-1 resided between peaks 1 and 2. These results, however, may be taken into account in the light of the finding of others who demonstrated that the formation of multimers of IGFBP-1 led to a reduction or loss of IGF-I binding.[10] Since the ability of IGFBP-1 to polymerize was also shown to be related to the loss of its capacity to inhibit IGF-I actions, it was suggested that this may be one mechanism by which phosphorylation of IGFBP-1 may enhance its inhibitory potential.[10] The deletion of twenty C-terminal amino acids from the IGFBP-1 molecule was also reported to result in a loss of IGF binding and the formation of dimeric IGFBP-1 molecules.[24]

Tissue transglutaminase is an enzyme which is widely distributed in many tissues and organs and which has been localized to the cytoplasm,[25] cell surface[26] and extracellular matrix.[27] Polymerization of IGFBP-1 is catalyzed not only by the isolated enzyme, but also by fetal fibroblast cell cultures and their membrane extract.[10] The expression of tissue transglutaminase at the embryo-maternal interface was recently discovered,[28] hence, this enzyme might be responsible for the presence of the IGFBP-1 dimers detected in this study.

Relevant literature data were sought in order to find protein candidates that might associate with the IGFBP-1 in the placental cell membranes. In human plasma, α_2-macroglobulin (α_2-M) forms high molecular mass complexes with IGFBP-1, it preferentially associates with p-IGFBP-1 and these complexes can still bind IGF-I.[29] On the other hand, the high molecular mass complexes of IGFBP-1 detected in this study consisted almost exclusively of np-IGFBP-1. Fur-

thermore, these forms bound only small amounts of ^{125}I-labeled IGF-I. α_2-M was detected in placental trophoblast.[30] It is known that some anti-IGFBP-1 antibodies recognize IGFBP-1 even when it is engaged in a complex with α_2-M, but some cannot.[29] The association of IGFBP-1 with α_2-M is suggested to be of low affinity, resulting in the dissociation of the complex during gel filtration,[29] whereas the high molecular mass complexes of IGFBP-1, which were immune-detected in the present experiments, survived the 7-min heating with SDS prior to SDS PAGE. An association of IGFBP-1 with α_2-M still cannot be ruled out.

When the phosphoisoforms of IGFBP-1 were separated by anion exchange chromatography, the fractions that contained phosphorylated forms inhibited IGF-I actions, whereas those that were enriched in np-IGFBP-1, potentiated IGF-I actions.[22] Taking this into account, it can be presumed that phosphorylation is the major factor modulating the affinity of IGFBP-1 for IGFs. It is suggested that the generation of non-phosphorylated and phosphorylated isoforms of IGFBP-1 and their association with cell membranes are involved in the regulation of IGF availability to IGF1R. Dimerization of IGFBP-1 may be a reversible process, catalyzed by membrane-associated tissue transglutaminase. Since IGFBP-1 and IGF1R compete for the ligand, increased binding of IGF-I to the IGF1R could be achieved through increased sequestering of high-affinity p-IGFBP-1 in dimers. The biological significance of dimeric IGFBP-1 forms has yet to be revealed.

CONCLUSIONS

Previously, the presence of IGFBP-1 in solubilized placental cell membranes was detected, *i.e.* its association with the membranes. Herein, it is reported that IGFBP-1 forms dimers, which preferably contain np-IGFBP-1. Polymerization of IGFBP-1 *in vitro* can be catalyzed by tissue transglutaminase, which was recently detected at the embryo-maternal interface. This enzyme might be responsible for the presence of the IGFBP-1 dimers detected in this study.

Acknowledgments. This work was supported by the Ministry of Science and Technological Development of the Republic of Serbia (Grant No. 143019).

ИЗВОД

ФОРМЕ ИГФБП-1 У МЕМБРАНАМА ПЛАЦЕНТНИХ ЋЕЛИЈА

РОМАНА МАСНИКОСА, БОГОВИД ЖИВКОВИЋ и ОЛГИЦА НЕДИЋ

ИНЕП–Институт за примену нуклеарне енергије, Банатска 31б, 11080 Београд

Унутарматерични раст фетуса зависи од правилног развоја и ваљаног функционисања плаценте. Инсулину-слични фактори раста (IGF) су важни фактори за развој плаценте. За време гестације, измењени ендометријум материце (децидуа) синтетише IGF-везујући протеин-1 (IGFBP-1), који контролише биолошко дејство IGF молекула. Разградња IGFBP-1 пореклом из децидуе, дејством металопротеаза из матрикса, сматра се новим механизмом контроле развића плаценте. У нашем ранијем раду утврдили смо присуство IGFBP-1 у солубилизованим мембранама ћелија из плаценте, што смо објаснили везивањем IGFBP-1 за

ћелијске мембране. У овом раду показано је да IGFBP-1 из солубилизованих мембрана образује димере, као и комплексе великих молекулских маса. Димери IGFBP-1 претежно садрже нефосфориловане молекуле мономерног IGFBP-1, док облици IGFBP-1 великих молекулских маса представљају агрегате IGFBP-1, и/или његове комплексе са другим мембранским протеинима. Димеризација IGFBP-1, као и његова асоцијација са ћелијским мембранама из плаценте, могла би да представља додатни механизам за регулацију доступности IGF молекула за тип 1 IGF рецептора.

(Примљено 9. марта, ревидирано 7. априла 2009)

REFERENCES

1. K. Forbes, M. Westwood, *Horm. Res.* **69** (2008) 129
2. D. LeRoith, C. Bondy, S. Yakar, J.-L. Liu, A. Butler, *Endocrine Rev.* **22** (2001) 53
3. S. M. Firth, R. C. Baxter, *Endocrine Rev.* **23** (2002) 824
4. R. C. Bunn, J. L. Fowlkes, *Trends Endocrinol. Metab.* **14** (2003) 176
5. D. J. Hill, D. R. Clemmons, S. C. Riley, N. Bassett, J. R. G. Challis, *Placenta* **14** (1993) 1
6. J. Fang, T. C. Furesz, C. H. Smith, M. E. Fant, *Growth Horm. IGF Res.* **9** (1999) 438
7. J. M. Gibson, J. D. Aplin, A. White, M. Westwood, *Mol. Hum. Reprod.* **7** (2001) 79
8. M. Westwood, J. M. Gibson, A. J. Davies, R. J. Young, A. White, *J. Clin. Endocrinol. Metab.* **79** (1994) 1735
9. H. A. Coppock, A. White, J. D. Aplin, M. Westwood, *Biol. Reprod.* **71** (2004) 438
10. K. Sakai, W. H. Busby Jr., J. B. Clarke, D. R. Clemmons, *J. Biol. Chem.* **276** (2001) 8740
11. J. I. Jones, W. H. Busby Jr., G. Wright, C. E. Smith, N. M. Kimack, D. R. Clemmons, *J. Biol. Chem.* **268** (1993) 1125
12. R. A. Frost, L. Tseng, *J. Biol. Chem.* **266** (1991) 18082
13. W. M. Hunter, F. C. Greenwood, *Nature* **194** (1962) 495
14. R. Masnikosa, I. Baričević, D. R. Jones, O. Nedić, *Growth Horm. IGF Res.* **16** (2006) 174
15. R. Masnikosa, J. A. Nikolić, O. Nedić, *J. Serb. Chem. Soc.* **68** (2003) 811
16. R. Masnikosa, A. Nikolić, O. Nedić, *J. Biochem.* **143** (2008) 813
17. M. M. Bradford, *Anal. Biochem.* **72** (1976) 248
18. I. Baričević, D. R. Jones, J. A. Nikolić, O. Nedić, *Horm. Metab. Res.* **38** (2006) 22
19. P. Hossenlopp, D. Seurin, B. Segovia-Quinson, S. Hardouin, M. Binoux, *Anal. Biochem.* **154** (1986) 138
20. D. R. Clemmons, M. L. Dehoff, W. H. Busby Jr., M. L. Bayne, M. A. Cascieri, *Endocrinology* **131** (1992) 890
21. B. E. Forbes, P. J. Hartfield, K. A. McNeil, K. H. Surinya, S. J. Milner, L. J. Cosgrove, J. C. Wallace, *Eur. J. Biochem.* **269** (2002) 961
22. J. Yu, M. Iwashita, Y. Kudo, Y. Takeda, *Growth Horm. IGF Res.* **8** (1998) 65
23. K. Sakai, A. J. D'Ercole, L. J. Murphy, D. R. Clemmons, *Diabetes* **50** (2001) 32
24. A. Brinkman, D. J. Kortleve, E. C. Zwarthoff, S. L. Drop, *Mol. Endocrinol.* **5** (1991) 987
25. C. S. Greenberg, P. J. Birckbichler, R. H. Rice, *FASEB J.* **5** (1991) 3071
26. C. A. Gaudry, E. Verderio, R. A. Jones, C. Smith, M. Griffin, *Exp. Cell Res.* **252** (1999) 104
27. C. Barsigian, A. M. Stern, J. Martinez, *J. Biol. Chem.* **266** (1991) 22501
28. M. Kabir-Salmani, S. Shiokawa, Y. Akimoto, K. Sakai, K. Sakai, M. Iwashita, *J. Clin. Endocrinol. Metab.* **90** (2005) 4694
29. M. Westwood, J. D. Aplin, I. A. Collinge, A. Gill, A. White, J. M. Gibson, *J. Biol. Chem.* **276** (2001) 41668
30. M. E. Gafvels, G. Coukos, R. Sayegh, C. Coutifaris, D. K. Strickland, J. F. Strauss 3rd, *J. Biol. Chem.* **267** (1992) 21230.

Journal of the Serbian Chemical Society
JSCS@tmf.bg.ac.rs • www.shd.org.rs/JSCS

J. Serb. Chem. Soc. 74 (7) 717–732 (2009)
JSCS–3870

UDC 635.71+635.74:546.264–31+66.061
Original scientific paper

Supercritical carbon dioxide extraction of antioxidants from rosemary (*Rosmarinus officinalis* L.) and sage (*Salvia officinalis* L.)

JASNA IVANOVIĆ[1*#], SONJA ĐILAS[2#], MILKA JADRANIN[3#], VLATKA VAJS[3#], NADA BABOVIĆ[1,4], SLOBODAN PETROVIĆ[1,5#] and IRENA ŽIŽOVIĆ[1#]

[1]*University of Belgrade, Faculty of Technology and Metallurgy, Karnegijeva 4, 11000 Belgrade,* [2]*University of Novi Sad, Faculty of Technology, Bulevar Cara Lazara 1, 21000 Novi Sad,* [3]*Institute for Chemistry, Technology and Metallurgy, Njegoševa 12, 11000 Belgrade,* [4]*Faculty of Applied Ecology, Singidunum University, Bulevar Mihaila Pupina 12a, 11000 Belgrade and* [5]*Hemofarm group, Vršac, Serbia*

(Received 20 November 2008, revised 13 January 2009)

Abstract: The aim of the present study was to isolate and characterize antioxidant extracts obtained from dried leaves of rosemary (*Rosmarinus officinalis* L.) and sage (*Salvia officinalis* L.), originating from the southern Balkan Region. The antioxidant fraction was isolated from the plant material by supercritical carbon dioxide (SC-CO_2) fractional extraction under a pressure of 30 MPa and at temperatures of 40 and 100 °C. In the present study, kinetic data and yields of antioxidant extracts obtained from dried leaves of rosemary and sage under different conditions were determined. Electron spin resonance (ESR) spectroscopy assay on the ability of the extracts to scavenge stable 2,2--diphenyl-1-picrylhydrazyl (DPPH) free radicals and reactive hydroxyl radicals during the Fenton reaction trapped by 5,5-dimethyl-1-pyrroline-*N*-oxide (DMPO) showed that the investigated extracts had antioxidant activity comparable to that of butylated hydroxyanisole (BHA) and commercial rosemary extract. The antioxidant fractions isolated at the higher temperature had higher antioxidant activities. A tentative analysis of the chemical composition of the antioxidant fractions obtained at the higher temperature was accomplished by LC-DAD and LC-MS analytical methods. Abietane-type diterpenoids, flavonoids and fatty acids were identified in the SC-CO_2 extract of rosemary and sage.

Keywords: rosemary; sage; supercritical extraction; antioxidant; DPPH; hydroxyl radicals.

* Corresponding author. E-mail: jasnai@tmf.bg.ac.rs
# Serbian Chemical Society member.
doi: 10.2298/JSC0907717I

INTRODUCTION

Herbs and spices have traditionally been used to impart flavour and aroma to food and for the prevention and treatment of a wide range of diseases. Recently, they have been extensively studied for their antiradical activities as well. Spices can be added to food as whole spices, as ground spices, or as isolates from their extracts. Whole and ground spices contain aromas, pigments, pungent components and other impurities and therefore their use as antioxidants is limited.[1] In order to produce plant extracts without flavour, odour and colour and with sufficient antioxidant activity to allow usage at levels equivalent to those of synthetic antioxidants (0.01–0.05 %), a number of different techniques for the isolation and concentration of antioxidants from rosemary and sage were proposed: solvent extraction (with polar and non-polar solvents),[2–5] aqueous alkaline extraction,[6] extraction with MCT (medium-chain triglycerides),[7] steam distillation and molecular distillation.[8] Almela *et al*.[3] and Erkan *et al*.[4] investigated the chemical composition and antioxidant activity of methanol extracts isolated from rosemary leaves. Haworth *et al.*[2] showed that a blend of tetrafluoroethane, acetone and methanol improved the total yield while a tetrafluoroethane and acetone blend had a higher efficacy but comparatively lower yields. The study of Tena *et al*.[5] indicated that the hydrogen-bonding ability of acetone and methanol was crucial for the extraction of the phenolic diterpenes responsible for antioxidant activity from rosemary leaves. Solvent extraction, which is generally used for the extraction of antioxidants from plant material, has some drawbacks, including antioxidant transformation, quite low selectivity, the extract is rich in compounds which may interfere with HPLC analysis, co-extracted aroma compounds must be eliminated, and extraction solvent residues are quite often prohibited by food regulations.[9] Molecular and steam distillation used to concentrate active fraction and to remove colour, aroma and flavour components result in different dilution effects due to the presence of the distillation carrier, which has a detrimental impact on the solubility of the extract in fats and oils,[10] while extraction with animal and vegetable oils suffers from low selectivity.[11]

Compared to mentioned methods, supercritical carbon dioxide (SC-CO_2) extraction appears to be an advantageous technology for the isolation of natural antioxidants from rosemary[5,9,10,12–15] and sage.[10,16–18] Tuning the process parameters (pressure, temperature) enables the tuning of the selectivity of SC-CO_2 towards the desirable components, as well as phase separation so that solvent-free extracts are obtained. In order to increase yields of antioxidants from rosemary at similar conditions, some authors added modifiers (co-solvents) such as ethanol. The use of modifiers generally increases the solubility of polar substances in carbon dioxide, although higher concentrations of modifiers can affect the selectivity.[10,12] Modifiers are not recommendable for supercritical extraction of antioxidants from Lamiaceae herbs at higher pressures (*e.g.*, 50 MPa and

higher) because of the significant decrease of the carbon dioxide selectivity and thus lower antioxidant activity of the supercritical extracts.[10] Nguyen *et al.*[10] isolated antioxidant fractions with a high efficiency from Lamiaceae herbs (rosemary, sage, thyme and oregano) with SC-CO_2 extraction under pressures in the range 50–100 MPa and at temperatures in the range 90–110 °C without using modifiers. In the same study, volatiles were recovered in a second separator at 3–3.5 MPa and 5–20 °C. Cavero *et al.*[12] isolated an antioxidant fraction from rosemary leaves with SC-CO_2 extraction under lower pressures and temperatures (15–35 MPa; 40–60 °C) without modifier and with 4 and 7 % of ethanol. The same authors used fractional separation whereby the volatiles were recovered in a second separator at 2 MPa and 20 °C. Ibanez *et al.*[13] used fractional extraction to isolate volatiles at 10 MPa and 40 °C and the antioxidant fraction at 40 MPa and 60 °C without using a modifier. Senorans *et al.*[14] isolated antioxidant extracts from rosemary at 30–35 MPa and temperatures in the range 40–60 °C with 0–2 % ethanol as modifier, while the volatiles were collected in a second separator at 2–5.5 MPa and 25 °C. Several authors used extraction of crude extracts of rosemary obtained by conventional methods (distillation, solvent extraction) to concentrate the antioxidant fraction.[17,19–21] Thereby, Braida *et al.*[19] concentrated extracts with antioxidative properties derived from Labiatae family herbs by means of an extraction–adsorption–desorption procedure using supercritical carbon dioxide as the solvent. Celiktas *et al.*[20] used SC-CO_2 to extract antioxidant fractions from distilled rosemary leaves collected from different locations and at different harvesting time intervals. In order to improve the antioxidant properties of a bleached alcoholic extract of sage, Djarmati *et al.*[17] used SC-CO_2 extraction to obtain antioxidant fractions at 60 °C and pressures of 20, 30 and 40 MPa and at 100 °C and 50 MPa. It was reported that antioxidant extracts obtained by SC-CO_2 extraction from rosemary and sage have an equivalent or stronger antioxidant activity than synthetic antioxidants.[10,16,17] The obtained supercritical extracts of rosemary and sage are semi-solid at ambient temperature. Furthermore, they can be ground at a temperature of –18 °C and dissolved or dispersed in animal or vegetable oils and fats.[10]

Earlier studies reported that the antioxidant activity of rosemary and sage is attributable to: phenolic diterpenes, such as carnosic acid, carnosol, rosmanol, epirosmanol, 7-methyl-epirosmanol and methyl carnosate, rosmadial;[22,23] rosmaridiphenol and rosmariquinone;[24,25] flavonoids, such as genkwanin, cirstimaritin and scutellarein[12,14] and phenolic acids, such as rosmarinic acid.[26] The list of the components with antioxidant properties isolated from sage is growing, *e.g.*, rosmanol 9-ethyl ether,[17] a range of rosmarinic acid derivatives (salvianolic acid K, salvianolic acid I, sagecoumarin and sagerinic acid) and flavone glycosides (luteolin 7-glucoside, luteolin 7-glucuronide, luteolin 3'-glucuronide, 6-hydroxyluteolin 7-glucoside, apigenin 6, 8-di-C-glucoside).[27] It was reported that SC-CO_2 ex-

traction provides the highest recovery of carnosic acid and carnosol from rosemary leaves compared to acetone, methanol, hexane and dichlormethane extraction.[5,9] Cavero *et al.*[12] and Senorans *et al.*[14] investigated the chemical composition of SC-CO_2 extracts of rosemary isolated under pressures in the range 15–35 MPa and at temperatures in the range 40–60 °C with the addition of ethanol as a modifier. Cuvelier *et al.*[28] studied the chemical composition of the antioxidant extracts of sage and rosemary obtained by different methods, including SC-CO_2 extraction, originating from pilot-plant or commercial sources. The study of Djarmati *et al.*[17] was aimed at isolating and identifying rosmanol-9-ethyl ether from *Salvia officinalis* by SC-CO_2 extraction of ethanol extracts and column-chromatographic isolation.

The present study was aimed at studying the kinetics of the isolation of the antioxidant fraction from dried leaves of wild growing rosemary and sage originating from the southern Balkan region using SC-CO_2 extraction and investigating the antioxidant activity of the SC-CO_2 extracts. The antioxidant activities of the plant extracts were evaluated by the scavenging activities of 2,2-diphenyl--1-picrylhydrazyl (DPPH) and of the hydroxyl radical using electron spin resonance (ESR) spectroscopy. Additionally, both liquid chromatography (LC)-mass spectrometry (MS) with an electrospray (ES) and liquid chromatography (LC) with a diode-array detector (DAD) were employed to perform the analysis and identification of the compounds responsible for the antioxidant activity of the rosemary and sage extract obtained at 30 MPa and 100 °C, which exhibited the highest antioxidant activity amongst the investigated supercritical extracts. As far as a literature survey ascertained, there have been no reports on the chemical composition of SC-CO_2 antioxidant extracts isolated from rosemary and sage at 30 MPa and 100 °C.

EXPERIMENTAL

Plant material

Dried leaves of wild growing rosemary (*Rosmarinus officinalis* L.) and sage (*Salvia officinalis* L.), originating from the southern Balkan region, were used for experimental studies. Commercial carbon dioxide (99 % purity, Tehno-gas, Novi Sad, Serbia) was used for the extractions.

Chemicals

2,2-Diphenyl-1-picrylhydrazyl (DPPH), 5,5-dimethyl-1-pyrroline-*N*-oxide (DMPO) and butylated hydroxyanisole (BHA) were purchased from the Sigma Chemical Co. (St. Louis, MO, USA). Commercial rosemary antioxidant, Flavor'Plus™, was purchased from Naturex, France. Methanol for HPLC, GC, pesticide residue analysis and spectrophotometry, purchased from Burdick & Jackson (Mashegon, MI, USA), acetonitrile gradient grade for liquid chromatography, purchased from Merck KG (Darmstadt, Germany), formic acid, 85 % pure, purchased from Lach-Ner, s.r.o. (Neratovice, Czech Republic) and Milli Q water 18.2 MΩ cm, obtained from a Millipore Simplicity 185 purification system, were used for the LC-MS

analyses. Carnosol and carnosic acid (≥91 % purity) were purchased from Sigma-Aldrich (USA).

Extraction method

Extractions with SC-CO_2 were preformed in a pilot-plant-scale supercritical fluid system (Autoclave Engineers SCE Screening System) with a previously described 150 ml extraction cell.[29] The plant material was fine milled to an average particle diameter of 0.4 mm. Fractional extraction was applied in order to obtain the antioxidants separately from the essential oil. The first fraction comprising essential oils was extracted at a pressure of 11.5 MPa and at a temperature of 40 °C. Thereafter, the antioxidant fraction was extracted at 30 MPa and at temperatures of 40 and 100 °C. The initially used mass of the plant samples was 64.05 g for rosemary and 56.20 g for sage. The mass flow rate of SC-CO_2 was 0.3 kg/h.

DPPH radical assay

A blank probe was obtained by mixing 400 µl of a 0.40 mM methanolic solution of DPPH and 200 µl of DMF (*N*,*N*-dimethylformamide). A volume of *x* µl of a 10 mg/ml DMF solution of the investigated extracts was added to a mixture of (200 – *x*) µl of DMF and 400 µl of 0.40 mM methanolic solution of DPPH radical (probe). The range of concentrations of the investigated extracts was 0.05–1.0 mg/ml for rosemary and 0.25–3.0 mg/ml for sage. Then the mixture was stirred for 2 min and transferred to a quartz flat cell ER-160FT. The ESR spectra were recorded on a Bruker 300E ESR spectrometer (Rheinstetten, Germany) under the following conditions: field modulation 100 kHz, modulation amplitude 0.256 G, receiver gain 2×10^4, time constant 40.96 ms, conversion time 327.68 ms, centre field 3440.00 G, sweep width 100.00 G, *x*-band frequency 9.64 GHz, power 20 mW, temperature 23 °C.

The SA_{DPPH} value of an extract is defined as:

$$SA_{DPPH}\ (\%) = 100(h_0 - h_x)/h_0$$

where h_0 and h_x are the height of the second peak in the ESR spectrum of DPPH radicals of the blank and the probe, respectively.

Hydroxyl radical assay

Hydroxyl radicals were obtained by the Fenton reaction in the system: 0.20 ml of 2.0 mM H_2O_2, 0.20 ml of 0.30 mM $FeCl_2{\cdot}4H_2O$ and 0.20 ml of 112 mM DMPO as the spin trap (blank). The influence of the investigated extracts of rosemary and sage on the formation and transformation of hydroxyl radicals was conducted by adding DMF solutions of the extracts to the Fenton reaction system in the concentrations range 0.25–10 mg/ml. The ESR spectra were recorded after 2.5 min, with the following spectrometer settings: field modulation 100 kHz, modulation amplitude 0.512 G, receiver gain 1×10^4, time constant 81.92 ms, conversion time 163.84 ms, centre field 3440.00 G, sweep width 100.00 G, *x*-band frequency 9.64 GHz, power 20 mW, temperature 23 °C.

The SA_{OH} value of an extract is defined as:

$$SA_{OH}\ (\%) = 100(h_0 - h_x)/h_0$$

where h_0 and h_x are the height of the second peak in the ESR spectrum of the DMPO-OH spin adduct of the blank and the probe, respectively.

LC analysis of the rosemary extracts with DAD and MS detection

In the present study, the chemical characterization of the supercritical fluid extracts of rosemary and sage obtained at 30 MPa and 100 °C was accomplished using both liquid chromatography (LC)-mass spectrometry (MS) with electrospray ionisation (ESI) and liquid chro-

matography (LC) with a diode-array detector (DAD). The samples were prepared by dissolving rosemary and sage supercritical extracts into methanol (c = 5.000 mg/ml). The analysis was performed using an HPLC instrument (Agilent 1200 Series, Agilent Technologies) with a degasser, an autosampler, a Zorbax Eclipse Plus C18 (150 mm×4.6 mm i. d.; 1.8 µm) column and a diode-array detector (DAD) coupled with a 6210 Time-of-Flight LC/MS system (Agilent Technologies). The mobile phase was a mixture of solvent A (0.20 % formic acid in water) and solvent B (acetonitrile) according to a combination of isocratic and gradient modes of elution: 0–1.5 min, 95 % A, 1.5–26 min, 95–5 % A, 26–35 min, 5 % A, at a flow rate of 1.40 ml/min. Detection was accomplished by using diode-array detector system (DAD), storing the signals in the wavelength range from 190–400 nm. The injection volume was 5 µl and the column temperature was 40 °C. A personal computer system running Mass Hunter Workstation software was used for data acquisition and processing. In the atmospheric pressure ionization ESI method, the eluted compounds were mixed with nitrogen in a heated nebuliser interface and the polarity was tuned to negative. An adequate calibration of the ESI parameters (capillary voltage, gas temperature, nebuliser pressure, and fragmentor voltage) was required to optimise the response and to obtain a high sensitivity of the molecular ion. The MS conditions were as follows: capillary voltage, 4000 V; gas temperature, 350 °C; drying gas, 12 ml/min; nebuliser pressure, 45 psig; fragmentor voltage, 140 V; mass range, 100–2000 m/z.

RESULTS AND DISCUSSION

Fractional extraction using SC-CO_2 was performed with the view to isolate and concentrate the antioxidant fraction from the rosemary and sage separately from the essential oils. The first fraction, which comprised the essential oil, was extracted at 11.5 MPa and a temperature of 40 °C in order to collect the aromatic and highly volatile components, mostly mono- and sesquiterpenes, and their oxygennated derivates. The obtained yields of the first fraction were 2.26 % (w/w) for sage and 1.03 % (w/w) for rosemary. The antioxidant fraction was isolated at a pressure of 30 MPa and at temperatures of 100 and 40 °C. The extraction yields of the antioxidant fraction obtained from rosemary and sage in the performed experiments are presented in Table I.

TABLE I. Yields of rosemary and sage antioxidant fractions in the performed experiments

Herbaceous material	p / MPa	t / °C	w / wt. %
Rosemary	30	40	1.10
		100	1.57
Sage	30	40	1.35
		100	1.74

The extraction yield curves of the antioxidant fractions extracted from rosemary and sage, performed at a pressure of 30 MPa and at temperatures of 40 and 100 °C, are presented in Figs. 1 and 2, respectively. Comparative extraction curves of rosemary and sage antioxidant extracts isolated under a pressure of 30 MPa at a temperature of 40 and 100 °C are presented in Figs. 3 and 4, respectively. As expected, at the lower operating temperature, lower yields of the antioxidant fraction from rosemary and sage were obtained. It was previously sug-

gested that the optimum rates and yields of SC-CO_2 extraction of antioxidants from Lamiaceae herbs are attained at temperatures between 90 and 110 °C at pressures above 30 MPa.[10] At extraction temperatures above 110 °C, heat damage can occur to the extracted compounds as well as to the extracted residue.[10] In the mentioned work,[10] the obtained yields of rosemary and sage supercritical extract isolated under a pressure of 50 MPa at a temperature of 100 °C were 5.2 and 5.7 %, respectively. Lower extraction temperatures are recommendable for economic reasons and especially for fractional separation when the aroma fraction is to be used further.[30]

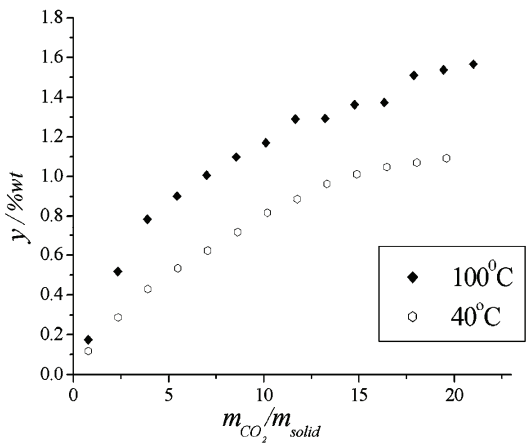

Fig. 1. Yields of rosemary antioxidant fractions as a function of the specific amount of solvent (kg CO_2/kg herbaceous material) for SC-CO_2 extraction at 30 MPa and different temperatures.

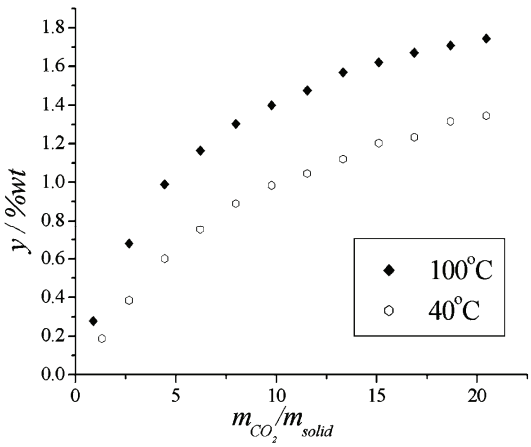

Fig. 2. Yields of sage antioxidant fractions as a function of the specific amount of solvent (kg CO_2/kg herbaceous material) for SC-CO_2 extraction at 30 MPa and different temperatures.

Daukşas *et al.*[16] investigated the influence of modifier (0–2 % of ethanol) on the yield of the SC-CO_2 extract of sage isolated under pressures of 25 and 35 MPa and at a temperature of 100 °C. They reported a significant increase in the total yield of SC-CO_2 extract after the addition of 1 % ethanol, while further

addition of ethanol was not efficient. In the same study,[16] the results clearly show that a large part of the sage substances is soluble at 30 MPa and higher pressures. A pressure between 25 and 30 MPa can be considered as a critical one in terms of the solubility of approximately 50 % of the sage extractives isolated at 35 MPa with CO_2 enriched with 1 % of ethanol.[16]

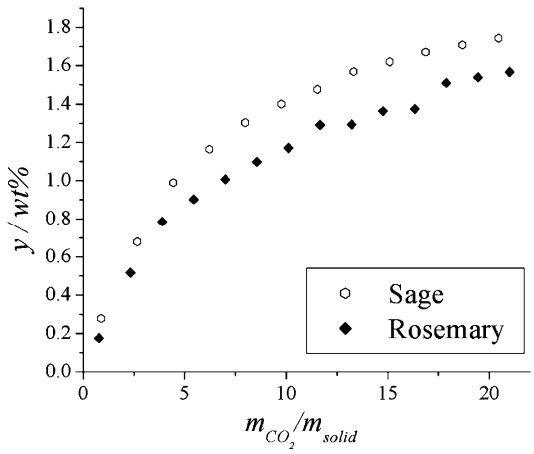

Fig. 3. Yields of antioxidant fraction as a function of the specific amount of solvent (kg CO_2/kg herbaceous material) for SC-CO_2 extraction from rosemary and sage at 30 MPa and 100 °C.

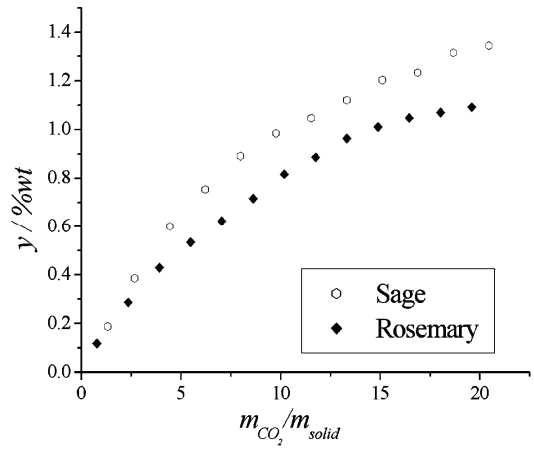

Fig. 4. Yields of antioxidant fraction as a function of the specific amount of solvent (kg CO_2/kg herbaceous material) for SC-CO_2 extraction from rosemary and sage at 30 MPa and 40 °C.

In the previously published paper, it was reported that the yield of rosemary antioxidant extract obtained by a one-step supercritical extraction under a pressure of 30 MPa was 3.3 and 5 % at a temperature of 30 and 40 °C, respectively.[16] Ibanez *et al.*[13] isolated rosemary antioxidant extract by a two-step extraction at a pressure of 40 MPa at a temperature of 60 °C and obtained 1.0–1.8 % yields. Under similar conditions (pressures in the range 15–35 MPa and temperature in the range 40–60 °C), Cavero *et al.*[12] obtained yields of rosemary antioxidant

extract of 3.93–6.78 %. The yield of SC-CO_2 sage extract (Lithuania) isolated by Dapkevicius *et al.*[18] at a pressure of 30 MPa and temperature of 40 °C was 5.02 %.

The yields of antioxidant extracts of rosemary and sage reported in this study were lower than the yields of antioxidant extracts of rosemary and sage reported in previously published papers. This could be explained in terms of different cultivation conditions, geographical locations and climate conditions. Celiktas *et al.*[20] also reported that the geographical location and seasonal variation have a great influence on the amount of active components in SC-CO_2 extracts. In this study, wild growing rosemary and sage from the southern Balkan region were used to obtain antioxidant extracts. Therewith, in order to achieve higher selectivity of the SC-CO_2 extraction and thus higher antioxidant activity of the SC--CO_2 extracts, no modifiers were used in this study. This could also be the reason for the lower yields of antioxidant extracts reported in this study.

According to the ESR data, all the investigated extracts scavenged DPPH and hydroxyl radicals in a concentration dependent manner. The scavenging activity (SA_{DPPH}, %) measured by the ability of different concentrations of antioxidant fractions isolated from rosemary leaves to scavenge the stable DPPH radicals is presented in Fig. 5. When the concentration of the SC-CO_2 extract from rosemary was increased from 0.010 to 1.0 mg ml^{-1}, the scavenging effect on the DPPH radicals was increased from 30 to 100 %. In the case of sage extracts, when the concentration was increased from 0.25 to 5.0 mg ml^{-1}, the scavenging effect on the DPPH radicals was increased from 32 to 100 % (for the extract isolated at a temperature of 100 °C) and from 18 to 100 % (for the extract isolated at a temperature of 40 °C). As can been seen, the scavenging activity of the rosemary and sage antioxidant extracts obtained at 30 MPa showed the same scavenging activity as a synthetic antioxidant (BHA) and a commercial rosemary extract (Flavor'Plus™) at a concentration of 1.0 mg ml^{-1} (for the rosemary extracts) and at concentrations in the range of 3.0–5.0 mg ml^{-1} (for the sage ex-

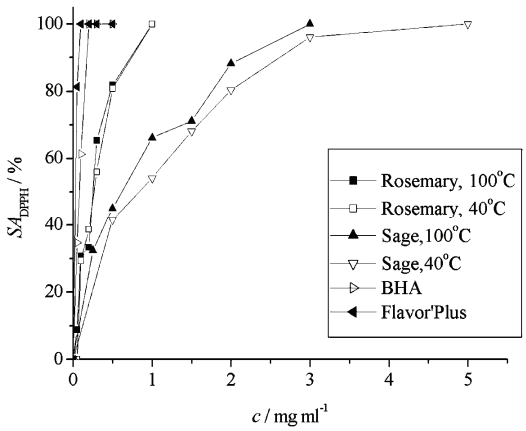

Fig. 5. The scavenging activity (SA_{DPPH}, %) of different concentrations of rosemary and sage antioxidant fractions, Flavor'Plus™ and BHA on DPPH radicals.

tracts). According to this method, rosemary antioxidant fractions exhibited higher antioxidant activities than the sage ones. It can be seen that even a concentration of 0.5 mg ml^{-1} of rosemary extracts reduced 81 % of the DPPH radicals. Sage extracts reduced 80–88 % of the DPPH radical molecules at a concentration of 2 mg ml^{-1}.

The antioxidative activities of the rosemary and sage extracts were investigated by the ability of the extracts to scavenge hydroxyl radicals as well (Fig. 6) because of the fact that hydroxyl radicals were mentioned as the major active oxygen species causing lipid oxidation.[31] To test the reactions of hydroxyl radicals with the investigated extracts, the Fenton reaction ($Fe^{2+} + H_2O_2 \rightarrow Fe^{3+} + OH^- + {}^{\bullet}OH$) was used as a source of hydroxyl radicals. Using a spin trap such as DMPO, it is possible to convert the reactive hydroxyl radicals into stable nitroxide radicals (DMPO–OH adducts). The relative intensity of the free radical formation can be determined because the intensity of the ESR spectroscopy signal is directly related to the concentration of the spin adducts. The scavenging activity (SA_{OH}, %) increased in the presence of 0.25–10 mg ml^{-1} SC-CO_2 extracts of rosemary from 18 to 100 % (for the extract isolated at 100 °C) and from 11 to 100 % (for the extract isolated at 40 °C). The scavenging effect (SA_{OH}, %) of the same concentrations of sage extracts increased from 20 to100 % (for the sage extract obtained at 100 °C) and from 6 to 100 % (for the sage extract obtained at 40 °C). The scavenging activities (SA_{OH}, %) of the sage and rosemary antioxidant fractions were the same as those of BHA and a commercial rosemary antioxidant (Flavor'Plus^{TM}) at concentrations from 5 to 6 mg ml^{-1} and higher. The rosemary extract obtained at 40 °C showed a much lower ability to scavenge reactive hydroxyl radicals in comparison to the other extracts at concentrations from 3 to 6 mg ml^{-1}. The rosemary extract isolated at 100 °C and the sage extracts showed satisfactory scavenging activity (82–91 %) at a concentration of 3 mg ml^{-1}.

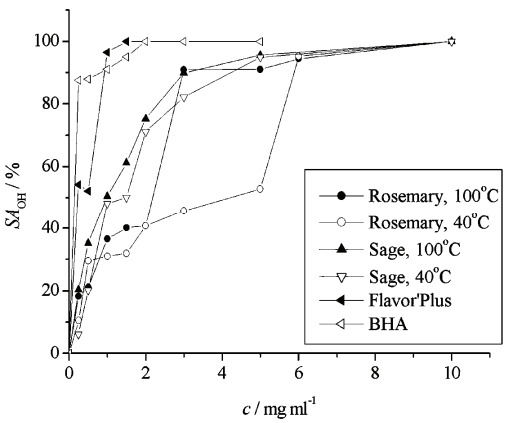

Fig. 6: The scavenging activity (SA_{OH}, %) of different concentrations of rosemary and sage antioxidant fractions, Flavor'Plus^{TM} and BHA on the DMPO--OH spin adduct.

Antioxidant fractions from rosemary and sage isolated at the higher temperature (100 °C) showed higher scavenging activities (SA_{DPPH} and SA_{OH}, %) than those obtained at the lower temperature. This is in accordance with previously published results on the antioxidant activity of SC-CO_2 extracts of Lamiaceae herbs.[10] Namely, the supercritical antioxidant extracts of rosemary and sage isolated at higher pressures 35–50 MPa at a temperature of 100 °C showed the highest levels of antioxidant activity, at least equal to BHA/BHT (1:1).[10] The SC-CO_2 extracts of rosemary isolated by Peng *et al.*[32] at 34.5 MPa and 80 °C showed a higher antiradical activity than BHA, trolox and ascorbic acid at all concentration levels according to the DPPH radical assay.

The rosemary and sage antioxidant fractions isolated at 30 MPa and 100 °C were chemically characterized by means of LC-MS.

The preliminary results of the LC–MS analysis are shown in Tables II and III. According to the tentative analysis of the chemical composition by means LC–MS, the most abundant components in the rosemary SC-CO_2 extract were abietane-type diterpenoids (*e.g.*, carnosic acid, carnosol, rosmadial, cafestol, rosemaridiphenol, methyl carnosate, 12-methoxycarnosic acid, *seco*-hinokiol, *etc.*) and flavonoids (wogonin, 7-methylapigenin, oroxylin A, biochanin A, genkwanin, negletin, acacetin, 5,6-dihydroxy-7-methoxyflavone). Similar components were identified in rosemary extracts isolated at pressures of 15–35 MPa and at temperatures of 40–60 °C [12,14] with ethanol as modifier and sub-critical water under pressures of 4–7 MPa and at temperatures of 25–200 °C.[65] Among the compounds in the SC-CO_2 extract of sage identified by the tentative analysis of chemical composition by means of LC–MS, abietane diterpenoids (carnosol, epiisorosmanol, royleanonic acid, royleanone, epirosmanol methyl ether, rosmanol, rosmadial, galdosol, carnosol *p*-quinone, safficinolide), fatty acids (C_{18}) and a triterpene (allobetulonlactone-1-en-2-ol) were identified.

TABLE II. Results of a preliminary LC-MS analysis of the chemical composition of rosemary antioxidant fraction isolated at 30 MPa and 100 °C

Formula	M_r / g mol^{-1}	t_R /min	Compounds
$C_{12}H_{18}O_3$	210	12.33	Jasmonic acid[33], vanillyl butyl ether[34]
$C_{16}H_{12}O_5$	284	15.08	Wogonin[35], genkwanin[12,36,37], oroxylin A[35], Biochanin A[38], acacetin[35], prunetin[39], 5,7 dihydroxy-6-methoxyflavone[35]
$C_{18}H_{32}O_4$	312	17.27	Oxiraneoctanic acid[40]
$C_{19}H_{28}O_4$	320	17.89	Ubiquinol-10[41]
$C_{20}H_{26}O_4$	330	18.41	Carnosol
$C_{20}H_{26}O_4$	330	18.64	Carnosol isomer
$C_{20}H_{24}O_5$	344	19.16	Rosmadial[42]
$C_{20}H_{28}O_3$	316	19.98	Rosemaridiphenol[43], cafestol[44], *seco*-hinokiol[45]
$C_{20}H_{28}O_4$	332	20.53	Carnosic acid
$C_{21}H_{30}O_4$	346	21.75	Methyl carnosate[46], 12-methoxycarnosic acid[46]
$C_{20}H_{30}O_3$	318	22.83	[9]-Shogaol[47]

TABLE III. Results of a preliminary LC-MS analysis of the chemical composition of sage antioxidant fraction isolated at 30 MPa and 100 °C

Formula	Mass	t_R / min	Compounds
$C_{10}H_{16}O_3$	184.23	9.62	*α*-Camphlonic acid[48], *cis*-pinonic acid[49]
$C_{20}H_{26}O_5$	346.42	13.96; 14.50; 15.19; 18.16	Rosmanol[43], epirosmanol[50], isorosmanol[51], royleanonic acid[52], epiisorosmanol[28]
$C_{20}H_{28}O_4$	332.43	14.66	Horminone[53], hydroxyroyleanone[54]
$C_{20}H_{24}O_5$	344.16	17.72;19.27; 19.77	Rosmadial[28], galdosol[55], carnosol *p*-quinone[56], safficinolide[57]
$C_{21}H_{28}O_5$	360.44	18.27	7-Methoxyrosmanol[52], epirosmanol methyl ether[28]
$C_{20}H_{26}O_4$	330.18	18.53	Carnosol (picrosalvin)
$C_{20}H_{26}O_4$	330.18	19.07	11,12-di-*O*-Methyl-picrosalvin[58]
$C_{20}H_{28}O_3$	316.44	19.90	Royleanone[59], rosmaridiphenol[48], 20-deoxocarnosol[60]
$C_{20}H_{28}O_4$	332.20	20.64	Carnosic acid (salvin)
$C_{21}H_{30}O_4$	346.21	21.88	12-*O*-Methylcarnosic acid[55], Methyl carnosate[43]
$C_{20}H_{30}O_3$	318.22	21.96; 22.97	2-Hydroxy-6-((6*Z*)-6-tridecenyl)-benzoic acid[61]
$C_{20}H_{28}O_2$	300.44	23.66	Retinoic acid[62], dehydroabietic acid[63], dehydro-4-epiabietic acid[63]
$C_{18}H_{30}O_2$	279.44	23.97; 25.36	Linolenic acid[64], trans-10-*cis*-12-octadecadienoic acid, *trans*-11-*cis*-9-Octadecadienoic acid[65]
$C_{30}H_{44}O_4$	468.32	28.68; 30.12; 30.49	Allobetulonlactone-1-en-2-ol[66]

As can been seen, both the rosemary and sage antioxidant fraction contained carnosic acid and its derivative carnosol. Miura *et al.*[55] reported that the antioxidant activity of carnosic acid, carnosol, rosmanol, isorosmanol, epirosmanol and galdosol (isolated from sage), measured by the OSI method using methyl linoleate at 90 °C and the DPPH method, were comparable to those of *α*-tocopherol and ascorbic acid. According to previously published results of Cavero *et al.*[12] carnosic acid is considered the main component in the rosemary extract isolated by SC-CO_2 responsible for the antioxidant activity determined by the DPPH test and the *β*-carotene bleaching assay.

The identification of carnosic acid and of carnosol was based on the retention time and authentic samples. The other compounds were tentatively identified in accordance with the molecular formula and data found by the Substance Identifier and Molecular Formula Search in SciFinder Scholar. The most probable compounds found in *R. officinalis* and *S. officinalis* related to adequate molecule formulas of detected compounds are given in Tables II and III.

CONCLUSIONS

This study showed that the yields of the antioxidant fraction from rosemary and sage obtained by SC-CO_2 extraction at 30 MPa and 100 °C were much higher than those obtained at a lower temperature (40 °C). Despite the somewhat lower yields, the SC-CO_2 extracts isolated from wild growing rosemary and sage from the southern Balkan region at a pressure of 30 MPa and at temperatures of 40 and 100 °C showed significant free radical scavenging activities towards the stable DPPH and highly reactive hydroxyl radicals, comparable to those of BHA and a commercial rosemary antioxidant. According to the DPPH assay, rosemary and sage antioxidant extracts obtained at 30 MPa showed the same scavenging activity as a synthetic antioxidant (BHA) and a commercial rosemary extract (Flavor'Plus™) at a concentration of 1.0 mg/ml (for the rosemary extracts) and at concentrations in the range 3.0–5.0 mg ml^{-1} (for the sage extracts). The hydroxyl radical assay showed that the rosemary and sage antioxidant fractions had a scavenging activity the same as those of BHA and a commercial rosemary antioxidant (Flavor'Plus™) at concentrations from 5 to 6 mg ml^{-1} and higher. Thereby, the antioxidant fractions of rosemary and sage isolated under a pressure of 30 MPa at the higher temperature (100 °C) of SC-CO_2 extraction exhibited somewhat higher antioxidant activities than those obtained at the lower temperature (40 °C). The rosemary antioxidant fractions had a higher antioxidant activity than those of sage towards stable DPPH radicals when used at same level. However, the rosemary and sage antioxidant fractions had a similar ability to scavenge hydroxyl radicals. In conclusion, this study indicates that supercritical extracts isolated from wild growing rosemary and sage from the southern Balkan region can be promising alternatives to synthetic antioxidants, although they need to be tested for the specific application in food.

Acknowledgments. The financial support of the Serbian Ministry of Science and Technological Development (EUREKA Project E! 3490 HEALTHFOOD) is gratefully acknowledged.

ИЗВОД

НАТКРИТИЧНА ЕКСТРАКЦИЈА АНТИОКСИДАНАСА ИЗ РУЗМАРИНА (*ROSMARINUS OFFICINALIS* L.) И ЖАЛФИЈЕ (*SALVIA OFFICINALIS* L.)

ЈАСНА ИВАНОВИЋ[1], СОЊА ЂИЛАС[2], МИЛКА ЈАДРАНИН[3], ВЛАТКА ВАЈС[3], НАДА БАБОВИЋ[1,4], СЛОБОДАН ПЕТРОВИЋ[1,5] и ИРЕНА ЖИЖОВИЋ[1]

[1]*Универзитет у Београду, Технолошко–металуршки факултет, Карнегијева 4, 11000 Београд,*
[2]*Универзитет у Новом Саду, Технолошки факултет, Булевар Цара Лазара 1, 21000 Нови Сад,*
[3]*Институт за хемију, технологију и металургију, Његошева 12, 11000 Београд,*
[4]*Факултет за примењену екологију, Универзитет Синглидунум,*
Булевар Михаила Пупина 12а, 11000 Београд и [5]*Хемофарм група, Вршац*

Циљ овог рада био је изолација и карактеризација антиоксидативних екстраката рузмарина (*Rosmarinus officinalis* L.) и жалфије (*Salvia officinalis* L.) са подручја јужног Балкана.

Антиоксидативна фракција изолована је из биљног материјала применом фракционе екстракције са наткритичним угљеник(IV)-оксидом на притиску од 30 MPa и на температурама од 40 и 100 °C. У овом раду су приказани резултати испитивања кинетике наткритчне екстракције антиоксидативних фракција из рузмарина и жалфије на различитим условима. Електрон спин резонантна (ESR) спектрална анализа утицаја антиоксидативних екстраката рузмарина и жалфије на трансформацију стабилних 2,2-дифенил-1-пикрилхидразил (DPPH) радикала као и на стварање и трансформацију реактивних хидроксилних радикала образованих у Фентоновој реакцији у присуству «спин-трапа» 5,5-диметил-1-пиролин-*N*-оксида (DMPO), показала је да испитивани екстракти имају антиоксидативну активност упоредиву са бутилованим хидроксианизолом (BHA) и комерцијалним рузмаринским антиоксидансом. Антиоксидативне фракције рузмарина и жалфије изоловане на вишој температури показале су већу антиоксидативну активност. За прелиминарну анализу хемијског састава антиоксидативних екстраката изолованих на вишој температури коришћена је течна хроматографија (LC) са детектором са низом диода (DAD) и течна хроматографија (LC) са масеном спектрометријом (MS). Екстракти рузмарина и жалфије садржали су абијетанске терпеноиде, флавоноиде и масне киселине.

(Примљено 20. новембра 2008, ревидирано 13. јануара 2009)

REFERENCES

1. M. Suhalj, *J. Food Comp. Anal*. **19** (2006) 531
2. J. Haworth, F. Brinkhaus, J. Graves, (Kemin Industries, Inc.), US 6,824,789 B2 (2004)
3. N. Erkan, G. Ayranci, E. Ayranci, *Food Chem*. **110** (2008) 76
4. L. Almela, B. Sánchez-Muñoz, J. A. Fernández-López, M. J. Roca, V. Rabe, *J. Chromatogr. A* **1120** (2006) 221
5. M. T. Tena, P. J. Hidalgo, J. L. Ubera, *Anal. Chem.* **69** (1997) 521
6. R. Viani (Societe d'Assistance Technique Pour Produits Nestle S.A.), US 4,012,531 (1977)
7. K. Schwarz, G. Bertelsen, L. R. Nissen, P. T. Gardner, M. I. Heinonen, A. Hopia, T. Huynh-Ba, P. Lambelet, D. McPhail, L. H. Skibsted, L. Tijburg, *Eur. Food Res. Technol.* **212** (2001) 319
8. S. S. Chang, B. Ostric-Matijasevic, C. Huang, A. Hsieh (Rutgers Research and Educational Foundation), US 3,950,266 (1976)
9. C. Bicchi, A. Binello, P. Rubiolo, *Phytochem. Anal.* **11** (2000) 236
10. U. Nguyen, G. Frankman, D. A. Evans (U. Nguyen), US 5,017,397 (1991)
11. D. L. Berner, G. A. Jacobson, C. Hill, C. D. Trombold (Cambell Soup Company), US 3,732,111 (1973)
12. S. Cavero, L. Jaime, P. J. Martin-Alvarez, F. J. Senorans, G. Reglero, *Eur. Food Res. Technol.* **221** (2005) 478
13. E. Ibanez, A. Oca, G. Murga, S. Lopez-Sebastian, J. Tabera, G. Reglero, *J. Agric. Food Chem.* **47** (1999) 1400
14. F. J. Senorans, E. Ibanez, S. Cavero, J. Tabera, G. Reglero, *J. Chromatogr. A* **870** (2000) 491
15. R. N. Carvalho, L. S. Moura, P. T. V. Rosa, A. A. J. Meireles, *J. Supercrit. Fluids* **35** (2005) 197
16. E. Dauksas, P. R. Venskutonis, V. Povilaityte, B. Sivik, *Nahrung/Food* **45** (2001) 338
17. Z. Đarmati, R. M. Jankov, E. Schwirtlich, B. Đulinac, A. Đorđević, *J. Am. Oil Chem. Soc.* **68** (1991) 731

18. A. Dapkevicius, R. Venskutonis, T. A. van Beek, J. P H. Linssen, *J. Sci. Food Agric*. **77** (1998) 140
19. I. Braida, M. Mattea, D. Cardarelli, *J. Supercrit. Fluids* **45** (2008) 195
20. O. Y. Celiktas, E. Bedir, F. V. Sukan, *Food. Chem.* **101** (2007) 1457
21. M. Hadolin, A. Rizner Hras, D. Bauman, Z. Knez, *Innov. Food Sci. Emerg. Techol.* **5** (2004) 245
22. K. Schwarz, W. Ternes, E. Schmauderer, *Z. Lebensm. Unters. Forsch.* **195** (1992) 99
23. M. E. Cuvelier, C. Berset, H. J. Richard, *J. Agric. Food Chem*. **42** (1994) 665
24. C. M. Houlihan, C. T. Ho, S. S. Chang, *J. Am. Oil Chem. Soc*. **61** (1984)1036
25. C. M. Houlihan, C. T. Ho, S. S. Chang, *J. Am. Oil Chem. Soc*. **62** (1985) 96
26. B. Zelić, M. Hadolin, D. Bauman, Đ. Vasić-Rački, *Acta Chim. Slov*. **52** (2005) 126
27. Y. Lu, L. Yeap Foo, *Food Chem.* **75** (2001) 197
28. M. E. Cuvelier, H. Richard, *J. Am. Oil Chem. Soc*. **73** (1996) 645
29. I. Zizović, M. Stamenić. J. Ivanović, A. Orlović, M. Ristić, S. Djordjević, S. Petrović, D. Skala, *J. Supercrit. Fluids* **43** (2007) 249
30. R. Kahleyss, F. Michlbauer (SKW Trostberg Aktiengesellschaft), US 5,433.949 (1995)
31. B. Lj. Milić, S. M. Djilas, J .M. Canadanović-Brunet, *Food. Chem.* **61** (1998) 443
32. C. Peng, J. Su, C. Chyau, T. Sung, S. Ho, C. Peng, R. Y. Peng, *Biosci. Biotechnol. Biochem.* **71** (2007) 2223
33. K. Stehfest, M. Boese, G. Kerns, A. Piry, C. Wilhelm, *J. Plant Physiol*. **161** (2004) 151
34. Y. Yamamoto, A. Hanano (Noevir Co. Ltd.), JP 2004059519 (2004)
35. F. A. Tomas-Barberan, E. Wollenweber, *Plant Syst. Evol.* **173** (1990), 109
36. P. Ramirez, M. R. Garcia-Risco, S. Santoyo, F. J. Javier, E. Ibanez, G. Reglero, *J. Pharm. Biomed. Anal.* **41** (2006) 1606
37. L. B. Almela, J. A. Sanchez-Munoz, M. J. R. Fernandez-Lopez, *J. Chromatogr. A* **1120** (2006) 221
38. T. Bajer, M. Adam, L. Galla, K. Ventura, *J. Sep. Sci.* **30** (2007) 122
39. G. Roy, R. Berardi, W. Chan, T. Lee (G. Roy, USA), US 2004/0091589 (2004)
40. R. Croteau, P. E. Kolattkudy, *Arch. Biochem. Biophys*. **162** (1974) 458
41. G. Cevc (Idea AG.) WO/2001/001962 (2001)
42. C. Xiao, H. Dai, H. Liu, Y. Wang, H. Tang, *J. Agric. Food Chem.* **56** (2008) 10142
43. D. Bauman, M. Hadolin, A. Rizner-Hras, Z. Knez, *Acta Aliment.* **28** (1999)15
44. M. J. Redmond, D. A. Fielder (Ceapro Inc.), WO 2004096242, 2004
45. C. L. Cantrell, S. L. Richheimer, G. M. Nicholas, B. K. Schmidt, D. T. Bailey, *J. Nat. Prod.* **68** (2005) 98
46. C. Hsieh, C. Peng, C. Chyau, Y. Lin, H. Wang, R. Y. Peng, *J. Agric. Food Chem.* **55** (2007) 2884
47. D. Kim (D. Kim), WO/2006/138399 (2006)
48. C. Funk, A. E. Koepp, R. Croteau, *Arch. Biochem. Biophys.* **294** (1992) 306
49. H. Gambliel, R. Croteau, *J. Biol. Chem*. **259** (1984) 740
50. S. Munne-Bosch, M. Mueller, K. Schwarz, L. Alegre, *J. Plant Physiol.* **158** (2001) 1431
51. K. Ninomiya, H. Matsuda, H. Shimoda, N. Nishida, N. Kasajima, T. Yoshino, T. Morikawa, M. Yoshikawa, *Bioorg. Med. Chem. Lett.* **14** (2004) 1943
52. C. H. Brieskorn, L. Buchberger, *Planta Med.* **24** (1973) 190
53. E. B. Asanov, A. V. Gayevsky, N. V. Tareyeva, V. I. Glyzin, *Khim. Farm. Zh.* **28** (1994) 32

54. T. Masuda, Y. Oyama, T. Arata, Y. Inaba, Y. Takeda, *ITE Lett. Batteries New Technol. Med.* **3** (2002) 39
55. K. Miura, H. Kikuzaki, N. Nakatani, *J. Agric. Food Chem.* **50** (2002)1845
56. M. Tada, K. Okuno, K. Chiba, E. Ohnishi, T. Yoshii, *Phytochemistry* **35** (1994) 539
57. C. H. Brieskorn, A. Fuchs, *Chem. Ber.* 95 (1962) 3034
58. N. A. Spiridonov, V. V. Arkhipov, A. G. Foigel, L. D. Shipulina, M. G. Fomkina, *Phytother. Res.* **17** (2003) 1228
59. Z. Đarmati, R. M. Jankov, Z. Vujčić, J. Csanadi, B. Djulinac, E. Švirtlih, A. Djordjević, K. Svan, *J. Serb. Chem. Soc.* **59** (1994) 291
60. D. Kim (D. Kim),WO/2006/138349 (2006)
61. P. Tomlinson (P. Tomlinson), WO/2008/101344 (2008)
62. P. Khadzhieva, K. Aleksiev, I. Topalova, in Proceedings of *F.E.C.S., Third Inernational Conference on Chemistry and Biotechnology of Biologically Active Natural Products*, Sofia, Bulgaria, (1985), p. 519
63. J. Kozlowski, I. Dedio, M. Krzyzaniak, *Herba Pol.* **44** (1998)161
64. M. Estevez, S. Ventanas, R. Ramirez, R. Cava, *J. Agric. Food Chem.* **52** (2004) 5168
65. R. M. Carlson, D. J. Gibson (Regents of the University of Minnesota), WO/2004/089357 (2004).
66. E. Ibanez, A. Kubatova, F. J. Senorans, S. Cavero, G. Reglero, S. B. Hawthorne, *J. Agric. Food Chem.* **51** (2003) 375

Journal of the Serbian Chemical Society
JSCS@tmf.bg.ac.rs • www.shd.org.rs/JSCS

J. Serb. Chem. Soc. 74 (7) 733–743 (2009)
JSCS–3871

UDC 547.82+542.44+542.913:57–188:615.281/.282
Original scientific paper

Synthesis of some biologically active 2,4'-bipyridine-5--carbonitriles carrying the 4-hydroxyphenylthio moiety

T. KARABASANAGOUDA[1], AIRODY VASUDEVA ADHIKARI[2]* and G. PARAMESHWARAPPA[3]

[1]*SeQuent Scientific Ltd., New Mangalore-575011,* [2]*Department of Chemistry, National Institute of Technology Karnataka, Surathkal, Srinivasnagar-575025 and* [3]*Department of Pharmaceutical Chemistry, Gulbarga University, Gulbarga-585106, India*

(Received 2 June 2008, revised 26 March 2009)

Abstract: A series of new 4-aryl-2'-[(4-hydroxyphenyl)thio]-6oxo-1,6-dihydro-2,4'-bipyridine-5-carbonitriles (**3a**–**k**) and 6-amino-4aryl-2'-[(4-hydroxyphenyl)thio]-2,4'-bipyridine-5-carbonitriles (**4a**–**h**) were synthesized from 4-hydroxythiophenol (**1**). The reaction of 4-hydroxythiophenol with 4-acetyl-2-chloropyridine yielded 1-{2-[(4-hydroxyphenyl)thio]pyridin-4-yl}ethanone (**2**). Further treatment of **2** with ethyl cyanoacetate in the presence of ammonium acetate with various aromatic aldehydes furnished the compounds **3a**–**k**. On the other hand, condensation of **2** with aromatic aldehydes in the presence of alcoholic malononitrile in ammonium acetate gave compounds **4a**–**h**. The structures of the newly synthesized compounds were established on the basis of their elemental analysis, as well as their IR, ^{1}H- and ^{13}C-NMR and mass spectral data. All the title compounds were subjected to *in vitro* antibacterial testing against two strains and antifungal screening against two fungi. Some of the compounds showed promising activity.

Keywords: 2,4'-bipyridine-5-carbonitriles; 3-cynopyridines; antibacterial; antifungal.

INTRODUCTION

The pyridine skeleton is of great importance to chemists as well as to biologists as it is found in a large variety of naturally occurring compounds and also in clinically useful molecules having diverse biological activities. Its derivatives are known to possess antitubercular,[1] anti-ulcer,[2] antimicrobial,[3–6] antineoplastic,[7] antitumor,[8–12] antiviral[13] and cardiotonic[14] properties. It has been well established that the presence of biologically active thiophenols is an important structural feature of a variety of synthetic drugs.[15–21] Encouraged by the above reports, it was planned to synthesize new 2,4'-bipyridine-5-carbonitriles carrying

* Corresponding author. E-mail: avchem@nitk.ac.in; avadhikari@yahoo.co.in
doi: 10.2298/JSC0907733K

the 4-hydroxyphenylthio moiety, aiming at an investigation of new heterocycles of enhanced pharmacological activities. The present study describes the synthesis of hitherto unreported 4-aryl-2'-[(4-hydroxyphenyl)thio]-6-oxo-1,6-dihydro-2,4'--bipyridine-5-carbonitriles (**3a**–**k**) and 6-amino-4-aryl-2'-[(4-hydroxyphenyl)-thio]-2,4'-bipyridine-5-carbonitriles (**4a**–**h**) and an evaluation of their *in vitro* antibacterial and antifungal activities.

RESULTS AND DISCUSSION

Chemistry

The reaction sequences employed for the synthesis of the title compounds is shown in Scheme 1. The key intermediate, 1-{2-[(4-hydroxyphenyl)thio]pyridin--4-yl}ethanone (**2**), required for the preparation of the target compounds was obtained by the condensation 4-hydroxythiophenol (**1**) with 2-chloro-4-acetylpyridine in pyridine medium. The compound **2** on treatment with aromatic aldehydes in presence of ethyl cyanoacetate and ammonium acetate in ethanolic medium yielded the compounds 4-aryl-2'-[(4-hydroxyphenyl)thio]-6oxo-1,6-dihydro-2,4'--bipyridine-5-carbonitriles (**3a**–**k**). On the other hand, condensation of **2** with aromatic aldehydes in presence of alcoholic malononitrile in ammonium acetate gave 6-amino-4-aryl-2'-[(4-hydroxyphenyl)thio]-2,4'-bipyridine-5-carbonitriles (**4a**–**h**).

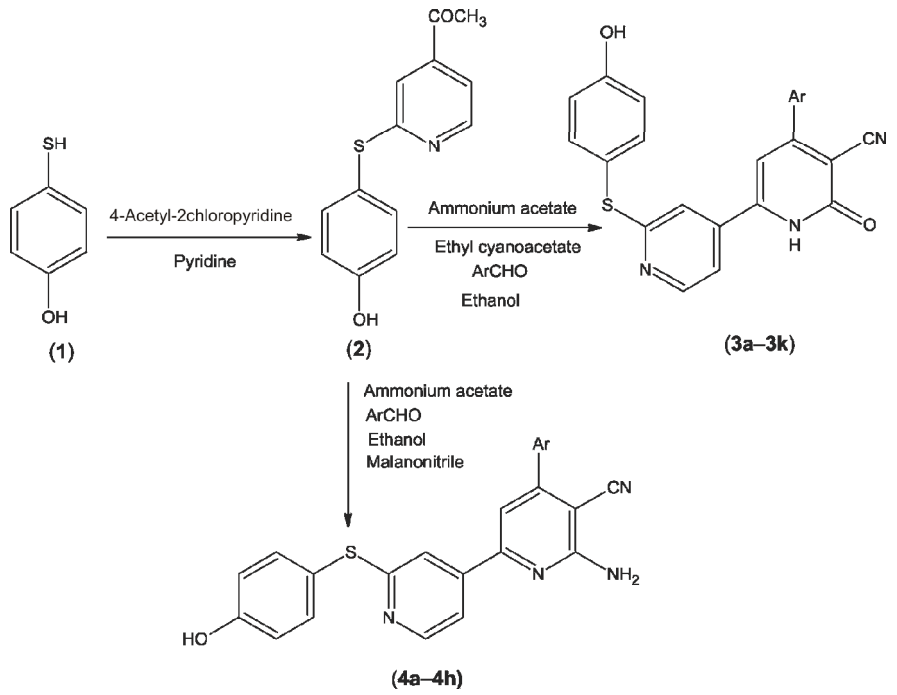

Scheme 1. The synthesis of the title compounds.

The structural elucidations of new compounds were based on their elemental analysis and spectral (IR, ^{1}H- and ^{13}C-NMR and mass) data. The characterization data of all the new compounds are summarized in Table I and their spectral data are given below.

TABLE I. Characterization data of compounds **3a**–**k** and **4a**–**h**

Compd.	Aromatic moiety	Molecular formula	Yield %	M.p. °C	Elemental analysis Found (Calcd.), %		
					C	H	N
3a	Phenyl	$C_{23}H_{15}N_3O_2S$	397.5	>260	70.00 (69.50)	3.91 (3.80)	10.80 (10.57)
3b	4-Chlorophenyl	$C_{23}H_{14}ClN_3O_2S$	432	>260	64.00 (63.96)	3.33 (3.27)	10.00 (9.73)
3c	3,4-Dimethoxyphenyl	$C_{25}H_{19}N_3O_4S$	457.5	238–240	65.70 (65.63)	4.25 (4.19)	9.20 (9.18)
3d	3-Hydroxy-4-methoxyphenyl	$C_{24}H_{17}N_3O_4S$	443.5	>260	65.50 (65.00)	3.90 (3.86)	9.52 (9.48)
3e	4-*N*,*N*-Diethylamino--2-hydroxyphenyl	$C_{27}H_{24}N_4O_3S$	484.5	>260	67.00 (66.92)	5.02 (4.99)	11.60 (11.56)
3f	4-Methylphenyl	$C_{24}H_{17}N_3O_2S$	411.5	>260	70.10 (70.05)	4.18 (4.16)	10.24 (10.21)
3g	4-Methoxyphenyl	$C_{24}H_{17}N_3O_3S$	427.5	>260	67.50 (67.43)	4.00 (4.01)	9.85 (9.83)
3h	4-Biphenylyl	$C_{29}H_{19}N_3O_2S$	473.5	>260	73.60 (73.55)	4.10 (4.04)	8.90 (8.87)
3i	2-Amino-3-pyridyl	$C_{22}H_{15}N_5O_2S$	413.5	>260	64.00 (63.91)	3.70 (3.66)	17.00 (16.94)
3j	2,3,5-Trihydroxyphenyl	$C_{23}H_{15}N_3O_5S$	445.5	>260	62.08 (62.02)	3.42 (3.39)	9.50 (9.43)
3k	6-Methoxy-2-naphthyl	$C_{28}H_{19}N_3O_3S$	477.5	250–252	70.50 (70.42)	4.00 (4.01)	8.84 (8.80)
4a	4-Chlorophenyl	$C_{23}H_{15}ClN_4OS$	431	230–232	64.14 (64.11)	3.54 (3.51)	13.10 (13.00)
4b	4-Methoxyphenyl	$C_{24}H_{17}N_4O_2S$	426.5	210–12	67.62 (67.59)	4.28 (4.25)	13.20 (13.14)
4c	3,4-Dimethoxyphenyl	$C_{25}H_{20}N_4O_3S$	456.5	205–07	65.80 (65.77)	4.46 (4.42)	12.30 (12.27)
4d	4-Methylphenyl	$C_{24}H_{18}N_4OS$	410.5	230–32	70.30 (70.22)	4.45 (4.42)	13.70 (13.65)
4e	3-Hydroxy-4-methoxyphenyl	$C_{24}H_{18}N_4O_3S$	442.5	>260	65.20 (65.14)	4.12 (4.10)	12.70 (12.66)
4f	4-Biphenylyl	$C_{29}H_{20}N_4OS$	472.5	>260	73.80 (73.71)	4.30 (4.27)	11.90 (11.86)
4g	2-Amino-3-pyridyl	$C_{22}H_{16}N_6OS$	429.5	>260	64.00 (64.06)	3.96 (3.91)	20.40 (20.38)
4h	2,3,5-Trihydroxyphenyl	$C_{23}H_{16}N_4O_4S$	444.5	>260	59.80 (59.73)	4.00 (3.92)	12.20 (12.11)

*2'-[(4-Hydroxyphenyl)thio]-6-oxo-4-phenyl-1,6-dihydro-2,4'-bipyridine-5-carbonitrile (**3a**)*. IR (KBr, cm^{-1}): 2912 (ArH), 2218 (C=N), 1640 (C=O), 1589 (C=C); ^{1}H-NMR (DMSO-d_6, δ / ppm): 6.90 (2H, *d*, C_3–, C_5–H of hydroxyphenylthio), 7.41 (2H, *d*, C_2–, C_6–H of 4-hydroxyphenylthio), 7.60 (5H, *m*, aryl moiety), 7.70 (3H, *m*, of pyridines), 8.50 (1H, *d*, C_6–H of pyridine moiety), 10.00 (1H, *s*, phenolic OH), 13.00 (1H, *s*, NH of pyridine moiety). LC–MS (*m*/*z*): 398 (M, 100 %).

*4-(4-Chlorophenyl)-2'-[(4-hydroxyphenyl)thio]-6-oxo-1,6-dihydro-2,4'-bipyridine-5-carbonitrile (**3b**)*. IR (KBr, cm^{-1}): 2903 (ArH), 2217(C=N), 1717 (C=O), 1512 (C=C); ^{1}H-NMR (DMSO-d_6, δ / ppm): 6.90 (2H, *d*, C_3–, C_5–H of hydroxyphenylthio), 7.40 (2H, *d*, C_2–, C_6–H of hydroxyphenylthio), 7.55–7.75 (7H, *m*, aromatic protons of pyridines and aryl moiety), 8.50 (1H, *d*, C_6–H of pyridine moiety), 10.00 (1H, *s*, phenolic OH), 13.00 (1H, *s*, NH of pyridine moiety); MS--FAB (*m*/*z*): 432 (M+1, 100 %), 431(M, 20 %), 415 (M–OH).

*4-(3,4-Dimethoxyphenyl)-2'-[(4-hydroxyphenyl)thio]-6oxo-1,6-dihydro-2,4'--bipyridine-5-carbonitrile (**3c**)*. IR (KBr, cm^{-1}): 2882 (ArH), 2206 (C=N), 1716 (C=O), 1498 (C=C); ^{1}H-NMR (DMSO-d_6, δ / ppm): 3.80 (3H, *s*, OCH_3), 3.90 (3H, *s*, OCH_3), 6.85 (m, 4H, C_3–, C_5–H of hydroxyphenylthio, C_2–, C_5–H of aryl), 7.18 (1H, *d*, C_6–H of aryl), 7.36 (3H, *m*, aromatic protons of pyridines), 7.42 (2H, *d*, C_2–, C_6–H of hydroxyphenylthio), 8.54 (1H, *d*, C_6–H of pyridine), 10.00 (1H, *s*, phenolic OH), 13.00 (1H, *s*, NH of pyridine); MS-FAB (*m*/*z*): 458 (M+1, 100 %), 457 (M, 20 %).

*4-(3-Hydroxy-4-methoxyphenyl)-2'-[(4-hydroxyphenyl)thio]-6-oxo-1,6-dihydro-2,4'-bipyridine-5-carbonitrile (**3d**)*. IR (KBr, cm^{-1}): 2854 (ArH), 2220 (C=N), 1743 (C=O), 1515 (C=C); ^{1}H-NMR (DMSO-d_6, δ / ppm): 4.0 (3H, s, OCH_3), 6.90 (2H, *d*, C_3–, C_5–H of hydroxyphenylthio), 7.40 (4H, *m*, C_2–, C_5–H of aryl, C_2–, C_6–H of hydroxyphenylthio), 7.42 (3H, *m*, aromatic protons of pyridine), 8.6 (1H, *d*, C_6–H of pyridine moiety), 10.00 (1H, *s*, phenolic OH), 13.00 (1H, *s*, NH of pyridine moiety); MS-FAB (*m*/*z*): 444 (M+1, 100 %).

*4-(4-*N,N*-Diethylamino-2-hydroxyphenyl)-2'-[(4-hydroxyphenyl)thio]-6oxo-1,6--dihydro-2,4'-bipyridine-5-carbonitrile (**3e**)*. IR (KBr, cm^{-1}): 2954 (ArH), 2225 (C=N), 1740 (C=O), 1510 (C=C); MS-FAB (*m*/*z*): 485 (M+1, 100 %), 484 (M, 40 %).

*2'-[(4-Hydroxyphenyl)thio]-4-(4-methylphenyl)-6-oxo-1,6-dihydro-2,4'-bipyridine-5-carbonitrile (**3f**)*. IR (KBr, cm^{-1}): 2913 (ArH), 2221 (C=N), 1638 (C=O), 1489 (C=C); ^{1}H-NMR (DMSO-d_6, δ / ppm): 2.40 (3H, *s*, CH_3), 6.90 (2H, *d*, C_3–, C_5–H of hydroxyphenylthio), 7.35 (2H, *d*, C_2–, C_6–H of hydroxyphenylthio), 7.44–7.60 (7H, *m*, aromatic protons of phenyl and pyridine), 8.5 (1H, *d*, C_6–H of pyridine moiety), 9.90 (1H, *s*, phenolic OH), 12.90 (1H, *s*, NH of pyridine moiety).

*2'-[(4-Hydroxyphenyl)thio]-4-(4-methoxyphenyl)-6-oxo-1,6-dihydro-2,4'-bipyridine-5-carbonitrile (**3g**)*. IR (KBr, cm^{-1}): 2903 (ArH), 2217 (C=N), 1717 (C=O), 1512 (C=C); ^{1}H-NMR (DMSO-d_6, δ / ppm): 3.85 (3H, *s*, OCH_3), 6.90 (2H, *d*, C_3–, C_5–H of hydroxyphenylthio), 7.10 (2H, *d*, C_2–, C_6–H of hydroxyphenylthio), 7.20 (2H, *d*, methoxyphenyl), 7.42 (2H, *d*, methoxyphenyl) 7.7 (3H, *m*, pyridine), 8.5 (1H, *d*, C_6–H of pyridine moiety), 12.90 (1H, *s*, phenolic OH), 13.00 (1H, *s*, NH of pyridine moiety).

*4-(4-Biphenylyl)-2'-[(4-hydroxyphenyl)thio]-6-oxo-1,6-dihydro-2,4'-bipyridine-5-carbonitrile (**3h**)*. IR (KBr, cm^{-1}): 2934 (CH_3), 2221 (C=N), 1644 (C=O), 1585 (C=C), 1489 (C=C); ^{1}H-NMR (DMSO-d_6, δ / ppm): 6.90 (2H, *d*, C_3–, C_5–H of hydroxyphenylthio), 7.40 (2H, *d*, C_2–, C_6–H of hydroxyphenylthio), 7.45––7.90 (12H, *m*, aromatic protons biphenyl and pyridine), 8.50 (1H, *d*, C_6–H of pyridine moiety), 10.00 (1H, *s*, phenolic OH), 13.00 (1H, *s*, NH of pyridine moiety).

*4-(2-Amino-3-pyridyl)--2'-[(4-hydroxyphenyl)thio]-6-oxo-1,6-dihydro-2,4'-bipyridine-5-carbonitrile (**3i**)*. IR (KBr, cm^{-1}): 3450 (NH_2), 2948 (ArH), 2236 (C=N), 1675 (C=O), 1611 (C=C), 1561 (C=C); ^{1}H-NMR (DMSO-d_6, δ / ppm): 6.90 (2H, *d*, C_3–, C_5–H of hydroxyphenylthio), 7.20 (2H, *m*, C_2–, C_6–H of hydroxyphenylthio), 7.42 (4H, *m*, protons of pyridines), 8.0 (1H, *d*, C_6–H of 2-amino-3-pyridyl moiety), 8.6 (1H, *d*, C_6–H of pyridine moiety), 10.00 (1H, *s*, phenolic OH), 13.00 (1H, *s*, NH of pyridine moiety).

*2'-[(4-Hydroxyphenyl)thio]-6-oxo-4-(2,3,5-trihydroxyphenyl)-1,6-dihydro--2,4'-bipyridine-5-carbonitrile (**3j**)*. IR (KBr, cm^{-1}): 2922 (ArH), 2224 (C=N), 1672 (C=O), 1589 (C=C), 1510 (C=C).

*2'-[(4-Hydroxyphenyl)thio]-4-(6-methoxy-2-naphthyl)-6-oxo-1,6-dihydro--2,4'-bipyridine-5-carbonitrile (**3k**)*. IR (KBr, cm^{-1}): 2936 (ArH), 2220 (C=N), 1658 (C=O), 1579 (C=C), 1488 (C=C); ^{1}H-NMR (DMSO-d_6, δ / ppm): 3.90 (3H, *d*, OCH_3), 6.9–8.0 (14H, *m*, aromatic protons), 8.6 (1H, *d*, C_6–H of pyridine moiety), 10.00 (1H, *s*, phenolic OH), 12.90 (1H, *s*, NH of pyridine moiety).

*6-Amino-4-(4-chlorophenyl)-2'-[(4-hydroxyphenyl)thio]-2,4'-bipyridine-5-carbonitrile (**4a**)*. IR (KBr, cm^{-1}): 3468 (NH_2), 2216 (CN), 1579 and 1494 (C=C); ^{1}H-NMR (DMSO-d_6, δ / ppm): 6.90 (2H, *d*, C_3–, C_5–H of hydroxyphenylthio), 7.40 (2H, *d*, C_2–, C_6–H of hydroxyphenylthio), 7.55–7.75 (7H, *m*, aromatic protons of pyridines and aryl moiety), 8.50 (1H, *d*, C_6–H of pyridine moiety), 10.00 (1H, *s*, phenolic OH); MS-FAB (*m*/*z*): 432 (M+1, 90 %), 431(M, 10 %).

*6-Amino-2'-[(4-hydroxyphenyl)thio]-4-(4-methoxyphenyl)-2,4'-bipyridine-5--carbonitrile (**4b**)*. IR (KBr, cm^{-1}): 3425 (NH_2), 2970 (CH_3), 2211(C=N), 1494 (C=C); ^{1}H-NMR (DMSO-d_6, δ / ppm): 3.85 (3H, *s*, OCH_3), 6.85 (2H, *d*, C_3–, C_5–H of hydroxyphenylthio), 7.18 (2H, *d*, C_3–, C_5–H of aryl), 7.36 (4H, *m*, C_2–, C_6–H of hydroxyphenylthio, C_2–, C_6–H of aryl), 7.6 (2H, *d*, aromatic protons of

pyridine), 7.90 (1H, *s*, C_3–H of pyridine), 8.52 (1H, *d*, C_6–H of pyridine moiety), 10.00 (1H, *s*, phenolic OH).

*6-Amino-4-(3,4-dimethoxyphenyl)-2'-[(4-hydroxyphenyl)thio]-2,4'-bipyridine-5-carbonitrile (**4c**)*. IR (KBr, cm^{-1}): 3630 (OH), 3337 (NH_2), 2970 (CH_3), 2207 (C=N), 1515 (C=C); ^{1}H-NMR (DMSO-d_6, δ / ppm): 3.8 (3H, *s*, OCH_3), 3.9 (3H, *s*, OCH_3), 6.90 (4H, *m*, C_3–, C_5–H of hydroxyphenylthio, C_2–, C_5–H of 4-aryl), 7.22 (1H, *d*, C_6–H of 4-aryl), 7.36 (3H, *m*, aromatic protons of pyridine), 7.42 (2H, *d*, C_2, C_6–H of hydroxyphenylthio), 8.54 (1H, *d*, C_6–H of pyridine), 10.00 (1H, *s*, phenolic OH); MS-FAB (*m*/*z*): 457(M, 10 %).

*6-Amino-2'-[(4-hydroxyphenyl)thio]-4-(4-methylphenyl)-2,4'-bipyridine-5-carbonitrile (**4d**)*. IR (KBr, cm^{-1}): 3416 (NH_2), 2919 (CH_3), 2206 (C=N), 1547 (C=C); ^{1}H-NMR (DMSO-d_6, δ / ppm): 2.40 (3H, *s*, CH_3), 6.90 (2H, *d*, C_3–, C_5–H of hydroxyphenylthio), 7.30 (2H, *d*, C_2–, C_6–H of hydroxyphenylthio), 7.42––7.70 (7H, *m*, aromatic protons phenyl and pyridine), 8.60 (1H, *d*, C_6–H of pyridine moiety), 10.00 (1H, *s*, phenolic OH).

*6-Amino-4-(3-hydroxy-4-methoxyphenyl)-2'-[(4-hydroxyphenyl)thio]-2,4'-bipyridine-5-carbonitrile (**4e**)*. IR (KBr, cm^{-1}): 3349 (NH_2), 2935 (CH_3), 2199 (C=N), 1555 (C=C); ^{1}H-NMR (DMSO-d_6, δ / ppm): 4.0 (3H, *s*, OCH_3), 6.90 (2H, *d*, C_3–, C_5–H of hydroxyphenylthio), 7.30 (2H, *d*, C_2–, C_6–H of hydroxyphenylthio), 7.42 (6H, *m*, aromatic protons of aryl and pyridine), 8.65 (1H, *d*, C_6–H of pyridine moiety), 10.00 (1H, *s*, phenolic OH); MS-FAB (*m*/*z*): 444 (M+1, 100 %).

*6-Amino-4-(4-biphenylyl)-2'-[(4-hydroxyphenyl)thio]-2,4'-bipyridine-5-carbonitrile (**4f**)*. IR (KBr, cm^{-1}): 3416 (NH_2), 2954 (ArH), 2214 (C=N), 1575 (C=C), 1490 (C=C); ^{1}H-NMR (DMSO-d_6, δ / ppm): 6.90 (2H, *d*, C_3–, C_5–H of hydroxyphenylthio), 7.30 (2H, *d*, C_2–, C_6–H of hydroxyphenylthio), 7.42–7.90 (12H, *m*, aromatic protons biphenyl and pyridine), 8.60 (1H, *d*, C_6–H of pyridine moiety), 10.00 (1H, *s*, phenolic OH).

*6-Amino-4-(2-amino-3-pyridyl)-2'-[(4-hydroxyphenyl)thio]-2,4'-bipyridine--5-carbonitrile (**4g**)*. IR (KBr, cm^{-1}): 3449 (NH_2), 2934 (ArH), 2197 (C=N), 1497 (C=C); ^{1}H-NMR (DMSO-d_6, δ / ppm): 6.90 (2H, *d*, C_3–, C_5–H of hydroxyphenylthio), 7.20 (2H, *m*, C_2–, C_6–H of hydroxyphenylthio), 7.42 (4H, *m*, protons of pyridines), 8.0 (1H, *d*, C_6–H of 2-amino-3-pyridyl moiety), 8.50 (1H, *d*, C_6–H of pyridine moiety), 10.00 (1H, *s*, phenolic OH).

*6-Amino-2'-[(4-hydroxyphenyl)thio]-4-(2,3,5-trihydroxyphenyl)-2,4'-bipyridine-5-carbonitrile (**4h**)*. IR (KBr, cm^{-1}): 3410 (NH_2), 2926 (ArH), 2210 (C=N), 1487 (C=C); ^{1}H-NMR (DMSO-d_6, δ / ppm): 5.90 (1H, *s*, C_4–H of 2,3,5-trihydroxyphenyl), 6.16 (1H, *s*, C_4–H of 2,3,5-trihydroxyphenyl), 6.90 (2H, *d*, C_3–, C_5–H of hydroxyphenylthio), 7.20 (2H, *d*, C_2–, C_6–H of hydroxyphenylthio), 7.42 (3H, *m*, protons of pyridine), 8.50 (1H, *d*, C_6–H of pyridine moiety), 10.00 (1H, *s*, phenolic OH).

The formation 1-{2-[(4-hydroxyphenyl)thio]pyridin-4-yl}ethanone (**2**) was confirmed by FTIR, ^{1}H-NMR, ^{13}C-NMR and elemental analyses. The IR spectrum of **2** exhibited absorption bands at 3066, 1700 and 1587 cm^{-1} due to CH_3, C=O and aromatic C=C stretching frequencies, respectively. Its ^{1}H-NMR spectrum showed singlets at δ 2.45, 7.17 and 9.48 ppm, which are due to CH_3, pyridine proton and hydroxyl proton, respectively. Further, doublets at 6.93 and 7.48 ppm are due to the aromatic protons of the 4-hydroxyphenylthio group, while the doublets at 7.35 and 8.55 ppm are due to protons of the pyridine nucleus. Its ^{13}C--NMR spectrum showed peaks at 26.07, 116.28, 116.73, 117.04, 117.40, 136.73, 142.88, 149.72, 158.67, 164.48 and 196.54 ppm, which are due to CH_3, C_1 of 4-hydroxyphenylthio, C_3 and C_5 of 4-hydroxyphenylthio, C_3 of pyridine, C_5 of pyridine, C_2 and C_6 of 4-hydroxyphenylthio, C_4 of pyridine, C_6 of pyridine, C_4 of 4-hydroxyphenylthio, C_2 of pyridine and C=O, respectively. It was observed that the peaks due to quaternary carbons disappeared on DEPT experimentation.

The build up of 2'-[(4-hydroxyphenyl)thio]-6-oxo-4-phenyl-2,4'-bipyridine--5-carbonitrile (**3a**) was established on the basis of FTIR, ^{1}H-NMR, ^{13}C-NMR, mass spectral and elemental analyses. Its IR spectrum exhibited peaks at 2920, 2218, 1640 and 1590 cm^{-1} due to stretching frequencies of CH_3, C≡N, C=O and C=C groups, respectively. Its ^{1}H-NMR spectrum exhibited two doublets at δ 6.90 and 7.41 ppm, due to the presence of the 4-hydroxyphenylthio moiety, and one multiplet for five protons at 7.60 ppm due to phenyl group at the position 4. Also, it appeared as a multiplet at 7.70 ppm, integrating for three protons, due to the pyridine rings and a doublet at 8.5 ppm due to the C_6–H of pyridine. The OH and pyridine –NH protons appeared at δ 10.00 and 13.00 ppm, respectively. The LC––mass spectrum displayed the molecular ion peak at *m*/*z* 398.1 (M+1, 100 %), which is in agreement with the molecular formula $C_{23}H_{15}N_3O_2S$.

The structure of 6-amino-4-chlorophenyl-2'-[(4-hydroxyphenyl)thio]-2,4'-bipyridine-5-carbonitrile (**4a**) was established on the basis of FTIR, ^{1}H-NMR, mass spectral and elemental analyses. The IR spectrum exhibited peaks at 3468, 2216 and 1579 cm^{-1}, which are due to the presence of NH_2, CN and C=C groups, respectively. The ^{1}H-NMR spectrum exhibited doublets at δ 6.90 and 7.40 ppm, which are due to the four protons of the 4-hydroxyphenylthio moiety. The appearance of a multiplet at 7.55–7.75 ppm is due to seven aromatic protons of the pyridines and aryl moiety. Furthermore, the appearance of a doublet at δ 8.50 ppm is due to C_6–H of the pyridine moiety. In addition, the proton of the hydroxyl group resonates at δ 10 ppm as a broad singlet. The FAB mass spectrum showed the molecular ion peak at *m*/*z* 431(M+1, 100 %), which is in accordance with the molecular formula $C_{23}H_{15}ClN_4OS$.

Biological screening

Antibacterial activity. All the title compounds, **3a**–**k** and **4a**–**h**, were evaluated for their *in vitro* antibacterial activity against two bacteria, *viz*., *Staphylococcus aureus* and *Escherichia coli*, using the cup plate method.[22,23] The solvent, *N*,*N*-dimethylformamide, showed no zone of inhibition. The activities were compared with the known standard drug gentamycin, used at a concentration of 1000 ppm. The results are summarized in Table II.

TABLE II. Antimicrobial activity of the title compounds

Compound	Zone of inhibition, mm			
	Antibacterial activity		Antifungal activity	
	Staphylococcus aureus	*Escherichia coli*	*Aspergillus niger*	*Candida albicans*
3a	16	17	20	22
3b	18	15	18	14
3c	12	14	20	16
3d	16	14	18	19
3e	10	12	21	20
3f	20	21	16	19
3g	17	22	22	23
3h	14	16	20	22
3i	17	15	20	18
3j	13	12	15	14
3k	14	15	17	16
4a	14	16	19	20
4b	16	12	17	16
4c	17	15	16	18
4d	16	16	15	12
4e	18	14	19	18
4f	14	16	20	22
4g	15	17	21	18
4h	17	13	14	16
Standard (flucanazole)	–	–	25	24
Standard (gentamycin)	21	23	–	–

Results of antibacterial studies revealed that compounds **3f** and **3g** showed fairly good activity against both the strains, while compounds **4b**, **4e** and **4g** showed good activity against *S. aureus*, and the remaining compounds exhibited moderate activity, compared to the standard gentamycin. The enhanced antibacterial activity in the compounds is attributed to the presence of 4-methylphenyl and 4-methoxyphenyl groups at the position 4 of the pyridine ring.

Antifungal activity. All the title compounds, **3a**–**k** and **4a**–**h**, were screened for their *in vitro* antifungal activity against *Aspergillus niger* and *Candida albicans* using the cup plate method.[22,23] The solvent, *N*,*N*-dimethylformamide

showed no zone of inhibition. The activities were compared with the known standard drug flucanazole, used at a concentration of 1000 ppm. The results are tabulated in Table II.

The results of the antifungal screening showed that compounds **3a**, **3e**, **3g**, **3h**, **4a**, **4f** and **4h** displayed good activity against both fungal strains, which were comparable with the standard flucanazole. Compounds **3b**, **3c**, **3d**, **3k** and **4e** showed good activity against *A. niger*, while the remaining compounds exhibited moderate activity when compared to flucanazole. It was noticed that the presence of the phenyl, *N*,*N*-diethylamino-2-hydroxyphenyl, 4-methoxyphenyl, 4-chlorophenyl, 4,4'-biphenyl-1-yl and 2-amino-3-pyridyl group at position 4 of the pyridine moiety led to increased antifungal activity.

EXPERIMENTAL

The melting points were determined in open capillaries and are uncorrected (melting point apparatus: Serwell Instruments Inc., India). The purity of the compounds was checked by thin layer chromatography (TLC) on a silica-coated aluminum sheet (silica gel $60F_{254}$) using chloroform and methanol (9:1, v/v). The IR spectra were recorded on a Nicolet Avatar 330-FTIR spectrometer. The ^{1}H- and ^{13}C-NMR spectra were recorded on a Varian 300 MHz NMR spectrometer using TMS as the internal standard. The chemical shifts (δ) are reported in ppm and the signals are described as singlet (*s*), doublet (*d*), triplet (*t*), quartet (*q*), broad (*br*) and multiplet (*m*). The FAB mass spectra were recorded on a Jeol SX 102/DA-6000 spectrophotometer/data system using argon/xenon (6 KV, 10 mA) FAB gas, at 70 eV. Elemental analysis was carried out using a Flash EA 1112 Series, CHNSO analyzer (Thermo). The solvents and reagents were purchased from commercial venders in the appropriate grade and were used without purification.

*Procedure for the preparation of 1-{2-[(4-hydroxyphenyl)thio]pyridin-4-yl}ethanone (**2**)*

A mixture of 12.6 g (0.10 mol) of 4-hydroxythiophenol (**1**) and 18.7 g (0.12 mol) of 2-chloro-4-acetylpyridine in 10 mL pyridine was heated under reflux for 8 h. After the reaction, the pyridine was evaporated under reduced pressure and the reaction mixture was diluted with water. The product was extracted with ethyl acetate and the extract was concentrated to 1/4th of the volume. The resulting solution was left overnight at room temperature. Solid product was collected by filtration, and finally recrystallized from ethyl acetate.

IR (KBr, cm^{-1}): 3066 (CH_3), 1700 (C=O), 1587 (Ar); ^{1}H-NMR ($CDCl_3$+DMSO-d_6, δ / ppm): 2.45 (3H, *s*, CH_3), 6.93 (2H, *d*, C_3–, C_5–H of hydroxyphenylthio, J = 8.72 Hz), 7.17 (1H, *s*, C_3–H of pyridine), 7.35 (2H, *d*, C_5–H of pyridine), 7.48 (2H, *d*, C_2–, C_6–H of hydroxylphenylthio), 8.55 (1H, *d*, C_6–H of pyridine), 9.48 (1H, *s*, OH of phenyl); ^{13}C-NMR ($CDCl_3$+ + DMSO-d_6, δ / ppm): 26.07 (CH_3), 116.28 (C_1 of 4-hydroxyphenylthio), 116.73 (C_3 and C_5 of 4-hydroxyphenylthio), 117.04 (C_3 of pyridine), 117.4 (C_5 of pyridine), 136.73 (C_2 and C_6 of 4-hydroxyphenylthio), 142.88 (C_4 of pyridine), 149.72 (C_6 of pyridine), 158.67 (C_4 of 4-hydroxyphenylthio), 164.48 (C_2 of pyridine), 196.54 (carbonyl).

*General procedure for the preparation of 4-aryl- -2'-[(4-hydroxyphenyl)thio]-6-oxo-1,6- -dihydro-2,4'-bipyridine-5-carbonitriles (**3a–k**)*

A mixture of 1-{2-[(4-hydroxyphenyl)thio]pyridin-4-yl}ethanone (**2**) (1.0 mmol), an aromatic aldehyde (1.0 mmol), ethyl cyanoacetate (1.0 mmol), ammonium acetate (4.0 mmol) and 5.0 mL ethanol was heated at reflux for 10 h. The reaction mixture was left overnight and the separated solids were filtered and recrystallized from ethanol.

*General procedure for the preparation of 6-amino-4-aryl-2'-[(4-hydroxyphenyl)thio]-2,4'--bipyridine-5-carbonitriles (**4a**–**h**)*

A mixture of 1-{2-[(4-hydroxyphenyl)thio]pyridin-4-yl}ethanone (**2**) (1.0 mmol), an aromatic aldehyde (1.0 mmol), malononitrile (1.0 mmol), ammonium acetate (4.0 mmol) and 10 mL of ethanol was heated at reflux for 6 h. The reaction mixture was left overnight and the separated solids were filtered and recrystallized from ethanol.

CONCLUSIONS

The successful syntheses of two series of heterocyclic title compounds and an evaluation of the antimicrobial activity of the new pyridines containing the 4-hydroxyphenylthio group were reported. From the results of the antimicrobial screening, it can be concluded that compound **3g** was found to be active against both bacteria and fungi. The activity is due to the presence of 4-methoxyphenyl group in the structure.

Acknowledgements. The authors are grateful to the Head, SAIF, CDRI Lucknow and the Director, NMR Research Centre II Sc., Bangalore for providing the NMR and mass spectral data.

ИЗВОД

СИНТЕЗА НЕКИХ БИОЛОШКИ АКТИВНИХ 2,4'-БИПИРИДИН-5-КАРБОНИТРИЛА КОЈИ САДРЖЕ 4-ХИДРОКСИФЕНИЛТИО ГРУПУ

T. KARABASANAGOUDA[1], AIRODY VASUDEVA ADHIKARI[2] и G. PARAMESHWARAPPA[3]

[1]*SeQuent Scientific Ltd., New Mangalore-575011,* [2]*Department of Chemistry, National Institute of Technology Karnataka, Surathkal, Srinivasnagar-575025 и* [3]*Department of Pharmaceutical Chemistry, Gulbarga University, Gulbarga-585106, India*

Серија нових 4-арил-2'-[(4-хидроксифенил)тио]-6-оксо-1,6-дихидро-2,4'-бипиридин-5--карбонитрила (**3a**–**k**) и 6-амино-4-арил-2'-[(4-хидроксифенил)тио]-2,4'-бипиридин-5-карбонитрила (**4a**–**h**) синтетизована је из 4-хидрокситиофенола (**1**). У реакцији 4-хидрокситиофенола са 4-ацетил-2-хлоропиридином добијен је 1-{2-[(4-хидроксифенил)тио]пиридин-4-ил}-етанон (**2**). Третирањем једињења **2** са етил-цијаноацетатом у присуству амонијум-ацетата са различитим ароматичним алдехидима добијена су једињења **3a**–**k**. С друге стране, једињење **2** кондензацијом са ароматичним алдехидима у присуству алкохолног раствора малононитрила у амонијум-ацетату наградило је једињења **4a**–**h**. Структуре нових једињења утврђене се на основу елементалне анализе, IR, ^{1}H и ^{13}C-NMR и MS спектралних података. Антибактеријска активност насловљених једињења, као и антифунгална активност тестирана је *in vitro* на два соја, односно два типа гљивица. Нека једињења показују охрабрујућу активност.

(Примљено 2. јуна 2008, ревидирано 26. марта 2009)

REFERENCES

1. G. H. Mikail, M. R. Arnold, G. F. Scott, *J. Med. Chem.* **44** (2001) 1560
2. S. Y. Cho, S. K. Kang, S. S. Kim, H. G. Cheon, J. K. Choi, E. K. Yum, *Bull. Korean Chem. Soc.* **22** (2001) 1217

3. W. J. Yeong, B. I. Weon, K. R. Jae, M. J. Shim, B. K. Won, C. C. Eung, *Bioorg. Med. Chem.* **12** (2004) 5909
4. F. E. Goda, A. A.-M. Abdel-Aziz, O. A. Attef, *Bioorg. Med. Chem*. **12** (2004) 1845
5. M. Satoshi, H. Takayuki, K. Mitsuo, *J. Agric. Food Chem.* **45** (1997) 2345
6. J. I. Sebat, A. J. Paszczynski, M. S. Cortese, R. I. Crawford, *Appl. Environ. Microbiol.* **67** (2001) 3924
7. L. Mao-Chin, L. Tai-Shun, C. G. Joseph, C. H. Ann, S. C. Alan, *J. Med. Chem.* **39** (1996) 2586
8. A. Tiwari, W. R. Waud, R. F. Struck, *Bioorg. Med. Chem.* **10** (2002) 3593
9. K. C. Nicolaou, R. Scarpelli, B. Bollbuck, B. Werschkun, M. Pereira, M. Wartmann, K. Altmann, D. Zaharevitz, R. Gussio, P. Giannakakou, *Chem. Biol.* **7** (2000) 593
10. D. Kovala-Demertzi, A. Boccarelli, M. A. Demertzis, M. Coluccia, *Chemotherapy* **53** (2007) 148
11. L. Mao-Chin, L. Tai-Shun, S. C. Alan, *J. Med. Chem.* **35** (1992) 3667
12. W. Yuqiang, L. Mao-Chin, L. Tai-Shun, S. C. Alan, *J. Med. Chem.* **35** (1992) 3672
13. M. Sylvie, R. Jean-Louis, G. Christophe, A. Hassan, S. Robert, A. Graciella, D. C. Erik, B. Jan, G. Alain, *Bioorg. Med. Chem*. **10** (2002) 941
14. C. Altomare, S. Cellamare, L. Summo, P. Fossa, L. Mosti, A. Carotti, *Bioorg. Med. Chem.* **8** (2000) 909
15. M. Ashok, B. S. Holla, B. Poojary, *Eur. J. Med. Chem.* **42** (2007) 1095
16. K. S. Kenneth, V. K. Joseph, US 4,028,394 (1977)
17. M. E. Deason, K. R. Whitten, US 5,962,725 (1999)
18. A. S. Bell, D. Brown, N. K. Terret, US 5,250,534 (1994)
19. I. W. Gunawardana, US 6,867,203 (2005)
20. M. Ashok, B. S. Holla, *J. Pharmacol. Toxicol.* **2** (2007) 256
21. O. Sangtae, J. H. In, A. M. Chan, S. Woon-Seob, L. Seokjoon, *Bioorg. Med. Chem*. **12** (2004) 3783
22. *Practical medical microbiology*, 14th ed.,. G. Collee, J. P. Duguid, A. G. Froser, B. P. Marmion, Eds., Churchill Livingstone, Edinburgh, 1996
23. The Pharmacopoeia of India, Controller of publication, New Delhi, 1985, A-9.

Journal of the Serbian Chemical Society
JSCS@tmf.bg.ac.rs • www.shd.org.rs/JSCS

J. Serb. Chem. Soc. 74 (7) 745–754 (2009) UDC 541.18:546.732'742'562'472+547.461.4
JSCS–3872 *Original scientific paper*

Effect of micelles on the chemical speciation of binary complexes of Co(II), Ni(II), Cu(II) and Zn(II) with succinic acid

BATHULA SRIKANTH, PEDADA SRINIVASA RAO, VASA SAMBA SIVA RAO, CHARLA KAMALA SASTRY and GOLLAPALLI NAGESWARA RAO*

School of Chemistry, Andhra University, Visakhapatnam-530 003, India

(Received 13 December 2008, revised 13 February 2009)

Abstract: Speciation of Co(II), Ni(II), Cu(II) and Zn(II) complexes with succinic acid in the presence of anionic, cationic and non-ionic surfactants at an ionic strength of 0.16 mol dm^{-3} and temperature 303 K were investigated pH metrically. The existence of different binary complex species was established from modelling studies using the computer program MINIQUAD75. The decreased stability of the complexes with increasing micellar content was explained by electrostatic forces. The influence of the micelles on the chemical speciation is discussed based on the mole fraction of the medium. Distribution diagrams of various species of the complexes in relation to pH are presented.

Keywords: succinic acid; speciation; essential metals; binary complexes; micelles.

INTRODUCTION

Succinic acid (suc) has great potential as a building block chemical,[1] being the precursor for many other chemicals made from renewable resources. It can be produced by fermentation and processed into a variety of products.[2] Succinate is a component of the citric acid cycle. Dialkyl succinates are essential chemicals for industries producing food and pharmaceutical products, surfactants and detergents, green solvents, biodegradable plastics and ingredients to stimulate animal and plant growth. Succinate is also involved in the metabolic pathway that forms part of the breakdown of carbohydrates, fats and proteins into carbon dioxide and water in order to generate energy in all living cells that utilize oxygen as part of cellular respiration.

Speciation studies of essential metal ion complexes of suc are useful[3–6] for the understanding of the role played by active site cavities in biological molecules and the binding behaviour of protein residues with metal ions. Cobalt in the form of vitamin B_{12} is essential for animals. Vitamin B_{12} is synthesized only by micro-organisms, in particular anaerobic bacteria. Nickel is associated with seve-

* Corresponding author. E-mail: gollapallinr@ yahoo.com
doi: 10.2298/JSC0907745S

ral enzymes[7–9] and any variation in its concentration leads to metabolic disorders.[10] Copper is largely rejected from cells but outside the cell, it is essential for the metabolism of many hormones and connective tissue. The biological functions include electron transfer, dioxygen transport, oxygenation, oxidation, reduction and disproportionation.[11,12] Zinc is the second most abundant essential trace metal after iron and it plays vital roles in biological systems.[13–16] Surfactants are used as detergents, cleaning agents, emulsifiers, in food, pharmaceuticals and cosmetics. Hence, speciation studies of suc with some essential metal ions, such as Co, Ni, Cu and Zn, in surfactant–water mixtures are reported in this paper.

EXPERIMENTAL

A solution 0.050 mol dm^{-3} of succinic acid (R.G., E-Merck, Germany) was prepared in triple distilled water. Aqueous solutions of Co(II), Ni(II), Cu(II) and Zn(II) chlorides (0.050 mol dm^{-3}) were prepared in 0.050 mol dm^{-3} HNO_3, to suppress the hydrolysis of the metal salts. A.R. or G.R. samples of sodium lauryl sulphate, SDS, (Qualigens, India), cetyltrimethylammonium bromide, CTAB (Qualigens, India) and Triton X-100, TX100, (E-Merck, Germany) were used as commercial products and their purity was checked by determining the critical micellar concentration (*CMC*) conductometrically. The *CMC* values of SDS, CTAB and TX-100 were 8.1×10^{-3}, 9.2×10^{-4} mol dm^{-3} and 0.54 vol. %, respectively, at 303 K. Sodium nitrate was used to maintain the ionic strength in the titrand. The strengths of alkali and mineral acid were determined using the Gran plot method.[17] To assess the errors that might have crept into the determination of the concentrations, the data were subjected to analysis of variance of one-way classification (ANOVA).

Apparatus

The titrimetric data were obtained using a calibrated ELICO (Model LI-120) pH-meter (readability 0.01), which can monitor changes in the H_3O^+ concentration. The glass electrode was equilibrated in a well-stirred micellar solution containing an inert electrolyte. All the titrations were performed at 303.0±0.1 K in a medium containing varying concentrations of the surfactants (0.5–2.5 % w/w) maintaining an ionic strength of 0.16 mol dm^{-3} with sodium nitrate. The effect of variations in asymmetry, liquid junction potential, activity coefficient, sodium ion error and dissolved CO_2 on the response of glass electrode were taken into account in the form of a correction factor, which was discussed in an earlier communication.[18]

Procedure and modelling strategy

For the determination of the stability constants of the binary metal–ligand species, initially titrations of a strong acid with alkali were performed at regular intervals to check whether complete equilibration had been achieved. Then the calomel electrode was refilled with micellar solution (only TX100 and CTAB but not SDS, since it forms a precipitate with KCl) of equivalent composition to that of the titrand. In each of the titrations, the titrand consisted of approximately 1 mmol mineral acid in a total volume of 50 cm^3. Titrations with different ratios (1:2.5, 1:3.5, 1:5) of metal to ligand were performed with 0.40 mol dm^{-3} sodium hydroxide. Other experimental details are given elsewhere.[19]

The computer program SCPHD[20] was used to calculate the correction factor. The binary stability constants were calculated from with the pH-metric titration data using the computer program MINIQUAD75,[21] which exploits the advantage of a constrained least-squares me-

thod in the initial refinement and reliable convergence of the Marquardt algorithm. During the refinement of the binary systems, the correction factor and the protonation constants of suc were fixed. The variation of stability constants with the mole fraction of the medium was analysed on electrostatic grounds based on solute–solute and solute–solvent interactions.

RESULTS AND DISCUSSION

The results of the best-fit models that contain the stoichiometry of the complex species and their overall formation constants along with some of the important statistical parameters are given in Tables I–III. The very low standard deviation in the log β values indicates the precision of these parameters. The small values of U_{corr} (sum of the squares of the deviations in the concentrations of the constituents at all experimental points) corrected for degrees of freedom, indicate that the experimental data can be represented by the model. The small values of the mean, standard deviation and mean deviation for the systems corroborate that the residuals are around a zero mean with little dispersion. For an ideal normal distribution, the values of the kurtosis and skewness should be three and zero, respectively. The kurtosis values in the present study indicate that the residuals form leptokurtic as well as platykurtic patterns[18] and very few form mesokurtic patterns. The values of skewness recorded in the Tables I–III are between –2.88 and –0.01. These data evince that the residuals form part of a normal distribution. Hence, least squares method can be applied to the present data. The sufficiency of the model is further evident from the low crystallographic *R*-values. These statistical parameters thus show that the best-fit models portray the metal–ligand species in micellar media.

Effect of systematic errors on best-fit model

In order to rely upon the best chemical model for critical evaluation and application under varied experimental conditions with different accuracies of data acquisition, an investigation was made by introducing pessimistic errors into influential parameters, such as the concentrations of alkali, mineral acid, ligand and metal (Table IV). The order of the components that influence the magnitudes of the stability constants due to incorporation of errors is alkali > acid > ligand > > metal. Some species were even rejected when errors were introduced in the concentrations. The rejection of some species and increased standard deviations in the stability constants on introduction of errors confirm the appropriateness of the experimental conditions (concentrations of the constituents) and the choice of the best-fit models.

Effect of the surfactant

Variation of the stability constants (log β) with mole fraction of surfactants in various micellar media exhibits a non-linear decreasing trend. The stability of the complex depends on the polarity of the medium, charge on the Stern layer[22]

TABLE I. Parameters of the best-fit chemical models of Co(II), Ni(II), Cu(II) and Zn(II)–succinic acid complexes in CTAB–water mixtures

CTAB % w/v	log $\beta(SD)$ ML	MLH	ML_2	ML_2H	ML_2H_2	*NP*	U_{corr}[a] $\times10^{-8}$	Skewness	χ^2	*R*-Factor $\times10^3$	Kurtosis	pH Range
						Co(II)						
0.0	–	9.99(4)	6.43(3)	12.52(8)	–	115	2.56	–1.93	31.09	73	4.07	1.60–8.50
0.5	–	8.87(5)	5.34(4)	11.34(7)	–	93	3.10	0.44	35.02	49	5.04	2.50–7.50
1.0	–	8.71(2)	5.30(3)	11.26(12)	–	98	8.15	0.71	22.04	5.2	9.21	2.00–7.90
1.5	–	8.69(2)	5.27(8)	11.20(10)	–	95	6.53	1.21	39.31	1.4	3.23	2.50–7.50
2.0	–	8.51(4)	5.16(7)	11.15(11)	–	89	4.72	1.04	47.71	65	5.45	2.50–5.50
2.5	–	8.29(2)	5.04(5)	11.06(12)	–	96	3.25	1.74	49.05	1.3	6.05	2.50–6.00
						Ni(II)						
0.0	4.47(2)	–	9.58(4)	12.68(7)	–	59	7.32	–0.18	21.92	83	2.93	2.00–7.00
0.5	3.36(1)	–	8.95(7)	11.64(8)	–	95	3.10	–2.42	29.01	9.5	3.42	2.50–6.00
1.0	3.29(2)	–	8.74(5)	11.72(8)	–	105	8.15	–2.54	32.13	72	4.44	1.85–6.50
1.5	3.20(2)	–	8.45(6)	11.51(9)	–	102	6.53	–1.09	13.59	46	8.02	1.85–6.00
2.0	3.11(3)	–	8.32(5)	11.39(10)	–	108	4.72	–1.74	18.92	8.5	7.31	1.85–7.00
2.5	3.03(3)	–	7.58(5)	11.16(11)	–	92	3.25	–1.80	17.41	9.6	4.92	2.50–6.00
						Cu(II)						
0.0	–	–	8.95(3)	11.86(5)	16.08(12)	71	0.65	–2.24	22.32	5.2	8.62	2.00–7.50
0.5	–	–	7.95(4)	10.95(6)	15.59(18)	100	6.40	–0.38	24.32	3.2	3.62	2.75–8.50
1.0	–	–	7.63(2)	10.68(4)	15.35(14)	101	8.29	–0.44	38.34	6.3	4.82	1.75–8.00
1.5	–	–	7.34(5)	10.48(6)	15.21(20)	94	8.74	–0.52	48.48	8.7	5.62	2.50–8.00
2.0	–	–	6.98(3)	10.35(5)	14.95(11)	89	8.02	–0.32	34.32	8.3	4.48	2.50–7.50
2.5	–	–	6.81(4)	10.02(6)	14.82(16)	85	4.09	–0.12	4.69	18	3.67	2.50–5.50
						Zn(II)						
0.0	–	10.75(3)	6.75(5)	14.87(6)	–	85	2.55	–1.34	19.32	3.9	4.32	2.00–7.50
0.5	–	9.94(2)	5.94(4)	13.91(6)	–	100	5.04	0.03	40.74	40	2.70	1.90–8.50
1.0	–	9.83(2)	5.83(4)	13.82(7)	–	97	2.64	1.35	64.25	2.2	8.32	1.70–7.50
1.5	–	9.52(4)	5.25(5)	13.50(8)	–	98	1.55	2.24	32.32	8.1	7.42	1.80–8.50
2.0	–	8.98(3)	4.93(5)	13.42(7)	–	85	4.24	1.00	44.81	39	6.93	1.75–7.00
2.5	–	8.62(6)	4.57(4)	13.15(7)	–	97	2.10	1.32	53.85	4.3	5.42	2.50–8.50

[a] $U_{corr} = U/(NP - m)\times10^8$, where, m = number of species; NP = number of experimental points

TABLE II. Parameters of the best-fit chemical models of Co(II), Ni(II), Cu(II) and Zn(II)–succinic acid complexes in TX100–water mixtures

TX100 % v/v	log $\beta(SD)$ ML	MLH	ML_2	ML_2H	ML_2H_2	NP	U_{corr}[a] $\times10^{-8}$	Skewness	χ^2	R–Factor $\times10^3$	Kurtosis	pH Range
						Co(II)						
0.0	–	9.99(4)	6.43(3)	12.52(8)	–	115	2.56	–1.93	31.09	73.2	4.07	1.60–8.50
0.5	–	8.64(2)	5.92(4)	11.98(7)	–	110	8.66	–1.84	35.42	93.2	5.94	1.64–8.50
1.0	–	8.39(1)	5.87(4)	11.78(4)	–	125	3.62	–2.85	98.32	14.2	9.34	1.65–8.00
1.5	–	8.27(4)	5.49(2)	11.52(5)	–	52	8.97	–1.24	25.32	83.2	4.85	2.00–5.50
2.0	–	7.97(2)	4.97(3)	10.89(8)	–	50	7.33	–1.84	29.64	85.4	3.32	2.00–5.60
2.5	–	7.64(1)	4.81(3)	10.56(8)	–	65	5.83	–1.01	34.29	45.9	2.83	2.00–6.00
						Ni(II)						
0.0	4.47(2)	–	9.58(4)	12.98(7)	–	59	7.32	–0.18	21.92	83.2	2.93	2.00–7.00
0.5	3.36(2)	–	8.75(4)	11.89(7)	–	55	8.09	–4.32	42.32	84.1	4.32	2.50–6.00
1.0	3.29(3)	–	8.65(5)	11.92(7)	–	51	6.66	–2.42	38.68	49.2	6.84	2.50–7.00
1.5	3.20(3)	–	8.53(4)	11.48(4)	–	57	1.89	–1.38	54.32	49.2	5.94	2.00–7.50
2.0	3.11(2)	–	7.97(5)	10.97(4)	–	78	5.74	–2.32	38.68	18.1	4.48	2.50–7.00
2.5	3.02(2)	–	7.62(5)	10.58(5)	–	80	9.22	–1.94	54.32	317	3.42	2.00–6.00
						Cu(II)						
0.0	–	–	6.94(3)	11.97(5)	16.08(12)	71	0.65	–2.24	22.32	5.23	8.62	2.00–7.50
0.5	–	–	5.90(7)	10.89(8)	15.76(10)	162	6.37	–1.49	45.20	3.43	3.14	1.50–8.50
1.0	–	–	5.76(5)	10.85(7)	15.89(21)	160	6.44	–2.42	22.15	8.41	2.15	1.50–8.20
1.5	–	–	5.62(6)	10.45(8)	15.35(14)	62	4.09	–4.42	42.52	9.31	4.82	2.50–7.50
2.0	–	–	4.98(6)	9.86(8)	14.98(15)	65	3.60	–1.82	52.11	8.31	3.42	2.50–8.00
2.5	–	–	4.78(7)	9.25(9)	14.53(10)	62	3.87	1.39	72.35	1.24	8.14	2.50–7.50
						Zn(II)						
0.0	–	10.75(3)	6.75(5)	14.87(6)	–	85	2.55	–1.34	19.32	3.94	4.32	2.00–7.50
0.5	–	9.87(1)	5.87(7)	13.89(11)	–	148	1.07	–1.88	38.25	17.3	8.32	1.62–8.50
1.0	–	9.82(3)	5.76(8)	13.56(12)	–	132	1.17	–2.49	57.52	18.3	7.92	1.60–8.00
1.5	–	9.51(3)	5.32(7)	13.25(12)	–	84	1.18	0.87	45.39	13.4	4.62	2.00–8.00
2.0	–	8.94(2)	4.95(8)	12.89(11)	–	82	8.46	–1.34	52.31	13.5	5.62	2.00–8.00
2.5	–	8.24(4)	4.78(7)	12.56(10)	–	77	2.27	0.47	39.21	42.9	3.90	2.00–7.80

[a] $U_{corr} = U/(NP - m)\times10^8$, where, m = number of species; NP = number of experimental points

TABLE III. Parameters of the best-fit chemical models of Co(II), Ni(II), Cu(II) and Zn(II)–succinic acid complexes in SDS–water mixtures

SDS % w/v	log $\beta(SD)$ ML	MLH	ML_2	ML_2H	ML_2H_2	*NP*	U_{corr}[a] $\times10^{-8}$	Skewness	χ^2	*R*–Factor $\times10^3$	Kurtosis	pH Range
						Co(II)						
0.0	–	9.99(4)	6.43(3)	12.52(8)	–	115	2.56	–1.93	31.09	73.2	4.07	1.60–8.50
0.5	–	9.25(3)	6.25(7)	12.01(11)	–	57	1.41	–1.18	22.87	35.6	6.29	2.00–7.00
1.0	–	8.79(2)	5.87(6)	11.75(12)	–	53	6.40	–1.24	31.32	46.0	5.52	2.50–6.70
1.5	–	8.53(2)	5.48(8)	11.54(10)	–	56	8.49	–1.33	27.31	3.20	3.39	2.00–6.90
2.0	–	8.23(4)	5.24(8)	11.35(10)	–	55	7.32	–2.30	18.10	5.60	2.36	2.00–7.00
2.5	–	7.56(2)	4.82(7)	10.58()12)	–	54	2.56	–2.25	16.21	81.4	4.42	2.00–6.50
						Ni(II)						
0.0	4.47(2)	–	9.58(4)	12.68(7)	–	59	7.32	–0.18	21.92	83.2	2.93	2.00–7.00
0.5	3.98(2)	–	9.01(15)	12.02(14)	–	51	4.02	–0.01	19.47	52.0	4.31	2.00–6.50
1.0	3.59(3)	–	8.56(14)	11.58(18)	–	54	5.88	–0.29	20.25	2.70	3.35	2.00–6.80
1.5	3.52(2)	–	8.31(15)	11.23(15)	–	56	9.24	–0.11	35.90	2.90	8.62	2.00–7.00
2.0	3.21(2)	–	7.86(15)	11.05(20)	–	53	6.40	–0.42	28.98	29.8	5.52	2.50–6.50
2.5	3.01(3)	–	7.25(12)	10.89(22)	–	52	8.97	–0.57	42.45	34.3	4.67	2.00–6.20
						Cu(II)						
0.0	–	–	6.94(3)	11.97(5)	16.08(12)	71	0.65	–2.24	22.32	5.20	8.62	2.00–7.50
0.5	–	–	7.15(2)	10.58(8)	15.47(17)	69	9.01	–1.51	19.49	3.90	5.52	2.00–6.80
1.0	–	–	7.32(4)	10.45(7)	15.84(20)	78	2.68	–1.45	27.07	51.2	4.67	1.70–7.40
1.5	–	–	7.54(4)	10.27(7)	15.77(22)	67	8.49	–1.59	32.38	49.7	7.72	2.00–6.50
2.0	–	–	7.18(3)	10.15(8)	15.35(19)	68	3.84	–1.28	17.49	83.2	4.67	2.50–7.00
2.5	–	–	7.21(3)	10.74(8)	15.08(20)	77	1.32	–1.49	27.48	73.5	5.49	1.70–7.50
						Zn(II)						
0.0	–	10.75(3)	6.75(5)	14.87(6)	–	85	2.55	–1.34	19.32	3.90	4.32	2.00–7.50
0.5	–	9.66(2)	5.58(8)	13.91(18)	–	92	3.30	–1.59	21.42	4.70	9.82	1.75–7.50
1.0	–	10.71(2)	6.66(5)	14.52(14)	–	87	3.43	–2.88	39.82	93.7	8.84	2.00–7.42
1.5	–	10.05(3)	6.17(7)	14.20(20)	–	79	7.33	–2.21	45.49	52.1	6.95	1.90–7.50
2.0	–	9.89(3)	5.92(7)	13.77(18)	–	84	8.06	–4.45	52.32	45.1	4.59	2.00–7.50
2.5	–	9.74(2)	5.74(8)	13.53(17)	–	81	4.58	–2.45	25.94	83.1	3.23	2.20–7.40

[a] $U_{corr} = U/(NP - m)\times10^8$, where, m = number of species; NP = number of experimental points

and the electrostatic attraction or repulsive forces operating between the complex species and the micellar surface. The dielectric constant of the medium decreases with increasing concentration of surfactant.[23,24] The charged species will be destabilized due to the decreased dielectric constant of the medium with increasing surfactant concentration. The linear decrease indicates the dominant action of electrostatic forces over non-electrostatic forces on the complex equilibria.

TABLE IV. Effect of errors in influential parameters on the stability constants of Ni(II) in Ni(II)-Suc in 1.0 %v/v TX100–water mixture

Component	Error, %	log $\beta(SD)$		
		MLH	ML_2	ML_2H
Alkali	0	3.29(3)	8.65(5)	11.92(7)
	–5	4.05(32)	Rejected	Rejected
	–2	3.55(11)	8.97(43)	12.07(32)
	+2	Rejected	8.84(10)	12.23(23)
	+5	3.92(12)	Rejected	Rejected
Acid	–5	Rejected	8.37(22)	Rejected
	–2	3.11(22)	8.05(43)	11.39(41)
	+2	Rejected	Rejected	12.30(35)
	+5	Rejected	9.67(44)	Rejected
Ligand	–5	3.82(24)	8.75(10)	12.09(70)
	–2	3.79(29)	8.71(10)	12.05(66)
	+2	3.85(49)	8.67(62)	12.03(84)
	+5	3.65(97)	8.78(14)	11.12(25)
Metal	–5	3.82(38)	8.82(41)	11.03(70)
	–2	3.79(37)	9.07(41)	12.01(70)
	+2	3.82(36)	8.77(42)	12.00(69)
	+5	3.88(35)	8.84(55)	12.08(69)

Distribution diagrams

Suc has two dissociable carboxyl protons, its various forms are LH_2, LH^- and L^{2-} in the pH ranges 3.0–6.5, 3.0–7.0 and 4.5–7.0, respectively. The protonation equilibria of L-aspartic acid, citric acid and succinic acid in anionic and cationic micellar media were earlier reported.[25,26] The plausible refined species are MLH, ML_2 and ML_2H for the Co(II) and Zn(II) systems; ML, ML_2 and ML_2H for Ni(II); ML_2, ML_2H and ML_2H_2 for Cu(II) in anionic, cationic and non-ionic micellar media.

Typical distribution diagrams of suc in CTAB–water mixtures are shown in Fig. 1, which indicates that ML_2 had formed to an extent of 60 % at pH values above 5.0. The formation of the various binary complex species is shown in the following equilibria:

$$M(II) + LH_2 \rightleftharpoons MLH^+ + H^+ \quad (1)$$

$$MLH^+ \rightleftharpoons ML + H^+ \quad (2)$$

$$M(II) + 2LH_2 \rightleftharpoons ML_2H_2 + 2H^+ \quad (3)$$
$$ML_2H_2 \rightleftharpoons ML_2H^- + H^+ \quad (4)$$
$$ML_2H^- \rightleftharpoons ML_2^{2-} + H^+ \quad (5)$$
$$M(II) + 2LH^- \rightleftharpoons ML_2H^- + H^+ \quad (6)$$
$$ML + LH^- \rightleftharpoons ML_2^{2-} + H^+ \quad (7)$$
$$M(II) + LH^- \rightleftharpoons ML + H^+ \quad (8)$$
$$MLH^+ + LH_2 \rightleftharpoons ML_2H_2 + H^+ \quad (9)$$
$$MLH^+ + LH^- \rightleftharpoons ML_2H^- + H^+ \quad (10)$$

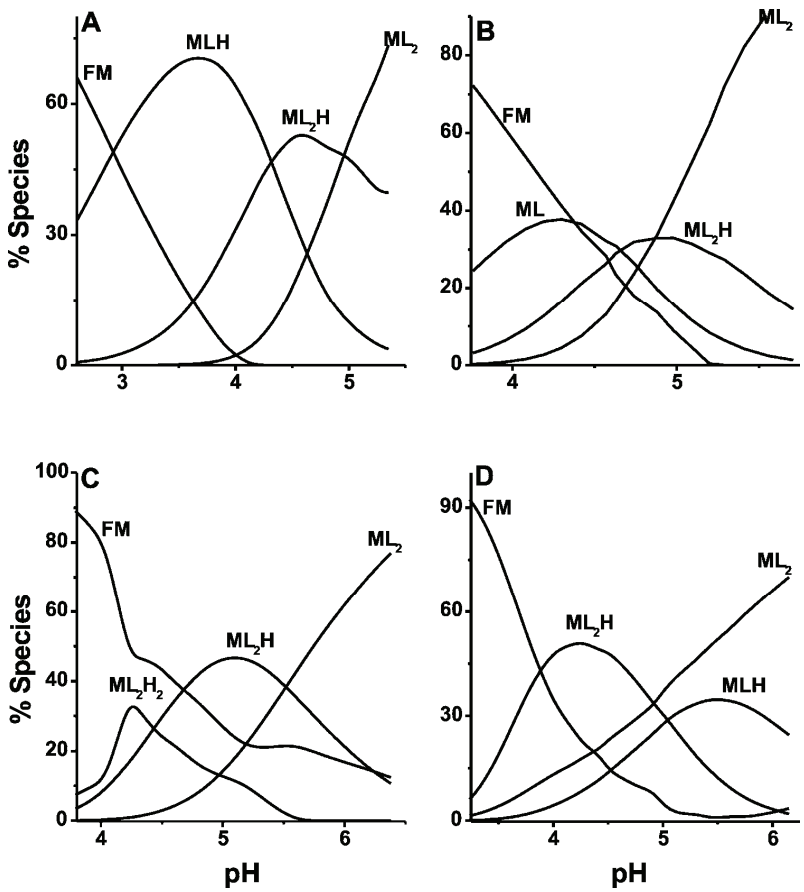

Fig. 1. Distribution diagrams of succinic acid complexes in 1.5 % w/v CTAB mixture. A) Co(II), B) Ni(II), C) Cu(II) and D) Zn(II).

For Co(II) and Zn(II), Eq. (5) is relevant because decreases in the percentage of ML_2H^- and increases in ML_2 were observed at the same pH (Figs. 1A and 1D). For Ni(II), Eqs. (5) and (8) are applicable (Fig. 1B). In the case of Cu(II),

Eqs. (3)–(5) are more appropriate because decreases in the percentage of ML_2H_2 and increases in the percentage of ML_2H^- were observed at the same pH (Fig. 1C).

CONCLUSIONS

The common species formed due to interaction of succinic acid with the studied metals are ML, MLH^+, ML_2^{2-}, ML_2H^- and ML_2H_2. The non-linear decrease of stability constants with mole fraction of the surfactant indicates the dominance of electrostatic forces over the non-electrostatic forces and a decreased dielectric constant with increasing surfactant concentration. The order of the components in influencing the magnitudes of the stability constants due to incorporation of errors is alkali > acid > ligand > metal.

ИЗВОД

УТИЦАЈ МИЦЕЛА НА ХЕМИЈСКУ СПЕЦИЈАЦИЈУ БИНАРНИХ КОМПЛЕКСА Co(II), Ni(II), Cu(II) И Zn(II) СА ЋИЛИБАРНОМ КИСЕЛИНОМ

B. SRIKANTH, P. SRINIVASA RAO, V. SAMBA SIVA RAO, C. KAMALA SASTRY и G. NAGESWARA RAO

School of Chemistry, Andhra University, Visakhapatnam-530 003, India

Изучавана је специјација Co(II), Ni(II), Cu(II) и Zn(II) комплекса са ћилибарном киселином у присуству анјонских, катјонских и нејонских површински активних супстанци при јонској јачини од 0,16 mol dm^{-3} и температури 303 K, пехаметријски. Моделовањем помоћу компјутерског програма MINIQUAD75 утврђено је постојање разних бинарних комплексних врста. Смањење стабилности комплекса са повећањем мицеларног садржаја приписано је електростатичким силама. Утицај мицела на хемијску специјацију дискутован је на основу молских удела. Приказани су дијаграми расподеле разних врста комплекса у зависности од pH вредности.

(Примљено 13. децембра 2008, ревидирано 13. фебруара 2009)

REFERENCES

1. T. Werpy, G. Petersen, *Top value added chemicals from biomass, Vol. 1, Results of screening for potential candidates from sugars and synthesis gas*, available at: http:////www.osti.gov/bridge (February 2008)
2. J. G. Zeikus, M. K. Jain, P. Elankovan, *Appl. Microbiol. Biotechnol.* **51** (1999) 545
3. K. V. Lavanya, V. M. Rao, G. N. Rao, *Oxid. Commun.* **31** (2008) 398
4. B. B. V. Sailaja, T. Kebede, G. N. Rao, M. S. Rao, *Proc. Natl. Acad. Sci. India* **74** (2004) 399
5. V. U. S. Sagar, G. Himabindu, K. G. Sudarsan, G. N. Rao, *J. Indian Chem. Soc.* **82** (2005) 598
6. G. N. Rao, A. Ramakrishna, *Proc. Natl. Acad. Sci. India* **75** (2005) 245
7. R. A. Poellot, T. R. Shuler, E. O. Uthes, F. H. Nielson, *Proc. Natl. Acad. Sci. USA* **44** (1990) 80
8. M. W. W. Adams, *Biochim. Biophys. Acta* **1020** (1990) 115
9. R. Cammack, *Nature* **373** (1995) 556
10. A. K. Kolodziej, *Prog. Inorg. Chem.* **41** (1994) 493
11. R. H. Holm, P. Kennepohl, E. I. Solomon, *Chem. Rev.* (1996) 2239

12. R. Mukherjee, *Comprehensive Coordination Chemistry – II: From Biology to Nanotechnology*, Elsevier, 2003, p. 747
13. Y. L. Lin, C. J. J. Lim, *J. Am. Chem. Soc.* **126** (2004) 2602
14. E. H. Cox, G. L. McLendon, *Curr. Opin. Chem. Biol.* **4** (2000) 162
15. J. H. Laity, B. M. J. Lee, P. E. Wright, *Curr. Opin. Struct. Biol.* **11** (2001) 39
16. T. Dudev, C. J. Lim, *J. Chin. Chem. Soc.* **50** (2003) 1093
17. G. Gran, *Anal. Chim. Acta* **206** (1988) 111
18. M. P. Latha, V. M. Rao, T. S. Rao, G. N. Rao, *Bull. Chem. Soc. Ethiop*. **21** (2007) 363
19. N. Padmaja, M. S. Babu, G. N. Rao, R. S. Rao, K. V. Ramana, *Polyhedron* **9** (1990) 2497
20. G. N. Rao, *Ph.D. Thesis*, Andhra University, Visakhapatnam, India, 1989
21. P. Gans, A. Sabatini, A. Vacca, *Inorg. Chim. Acta* **18** (1976) 237
22. C. A. Bunton, G. Cerichelli, Y. Ihara, L. Supulveda, *J. Am. Chem. Soc*. **101** (1979) 2429
23. A. K. Singh, D. Manjula, *J. Indian Chem. Soc.* **71** (2001) 635
24. E. H. Cordes, *Pure Appl. Chem.* **50** (1978) 617
25. P. S. Rao, B. Srikanth, V. S. S. Rao, C. K. Sastry, G. N. Rao, *Eur. J. Chem*. **6** (2009) 561
26. B. Srikanth, P. S. Rao, V. S. S. Rao, C. K. Sastry, G. N. Rao, *Proc. Natl. Acad. Sci. India* **79** (2009) 335.

Journal of the Serbian Chemical Society
JSCS@tmf.bg.ac.rs • www.shd.org.rs/JSCS

J. Serb. Chem. Soc. 74 (7) 755–764 (2009)
JSCS–3873

UDC 546.661+546.650:548.7:544.553.537:621.315.59
Original scientific paper

Synthesis, structure, semiconductive and photoluminescent properties of $[\{Eu(NC_5H_4COOH)_3(H_2O)_2\}(1.5ZnCl_4)\cdot(2H_2O)]_n$

WEN-TONG CHEN*, XIAO-NIU FANG, QIU-YAN LUO and YA-PING XU

School of Chemistry and Chemical Engineering, Jinggangshan University, 343009, Ji'an, Jiangxi, P.R. China

(Received 18 November 2008, revised 20 February 2009)

Abstract: A novel bimetallic 4f–3d metal-isonicotinic acid inorganic–organic hybrid complex $[\{Eu(NC_5H_4COOH)_3(H_2O)_2\}(1.5ZnCl_4)\cdot(2H_2O)]_n$ (**1**) was synthesized *via* a hydrothermal reaction and structurally characterized by single-crystal X-ray diffraction. Complex **1** crystallizes in the space group *C*2/*c* of the monoclinic system with eight formula units in a cell: a = 23.878(8) Å, b = 20.573(6) Å, c = 15.358(5) Å, β = 127.276(5)°, V = 6003(3) Å^3, $C_{18}H_{23}Cl_6EuN_3O_{10}Zn_{1.5}$, M_r = 904.11 g/mol, ρ = 2.001 g/cm^3, S = 1.077, μ(Mo$K\alpha$) = 3.846 mm^{-1}, F(000) = 3536, R = 0.0270 and wR = 0.0672. Complex **1** has a characteristic, one-dimensional polycationic chain-like structure. A photoluminescent investigation revealed that the title complex displays intense emissions in the orange and red regions. The luminescence spectra show that the red emission is stronger than the orange emission. Optical absorption spectra of **1** revealed the presence of an optical gap of 3.56 eV.

Keywords: crystal structure; europium; lanthanide; photoluminescence; semiconductor.

INTRODUCTION

In recent years, inorganic–organic hybrid complexes containing trivalent lanthanides have attracted increasing attention for use as the active species in luminescent materials, magnetic functional materials, catalysts, electroluminescent devices, zeolite-like materials, and so forth.[1–5] Moreover, for a vast number of inorganic–organic hybrid materials, the intriguing variety of the architectures and topologies that can be obtained by the self-assembly of the metal ions and multifunctional ligands has attracted the attention of chemists. Hitherto, although the synthesis of inorganic–organic hybrid materials based on transition metals has become widespread,[6–12] there are relatively few reports on lanthanide-based inorganic–organic hybrid materials, despite their potential applications in lumines-

* Corresponding author. E-mail: cwtqq@yahoo.com.cn
doi: 10.2298/JSC0907755C

cence and other fields.[13] To the best of our knowledge, lanthanide-based inorganic–organic hybrid materials with aromatic carboxylic acids exhibit good thermal and luminescent stability for practical application. In addition, transition metal complexes containing group 12 (IIB) elements are particularly attractive for many reasons, such as, the variety of coordination numbers and geometries provided by the d^{10} configuration of the IIB metal ions, the well-known toxicity of cadmium and mercury, their semiconductor properties and the essential role in biological systems of zinc, *etc*. Taking the above into account, it was deemed that LN-IIB-based (LN = lanthanide) inorganic–organic hybrid materials with aromatic carboxylic acids as ligands may have novel structural topologies and properties, such as photoluminescence, semiconductivity, magnetism, electro- and photochemistry, catalysis, thermochromism and so forth. Therefore, our group recently became interested in the crystal engineering of LN-IIB-based inorganic––organic hybrid materials with isonicotinic acid as the ligand (Scheme 1). In this paper, the synthesis, crystal structure, and semiconductive and photoluminescent properties of $[\{Eu(NC_5H_4COOH)_3(H_2O)_2\}(1.5ZnCl_4)\cdot(2H_2O)]_n$ (**1**) are reported.

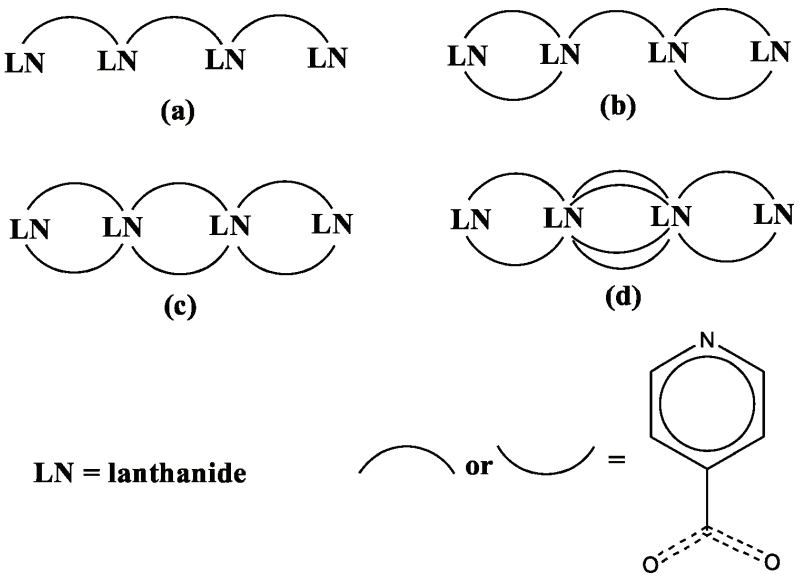

Scheme 1. Important chain-like structural types of isonicotinic acid bridging LN centres: a) 1-1-1; b) 2-1-2; c) 2-2-2; d) 2-4-2 types, in which the number indicates the number of the bridges.

EXPERIMENTAL

Chemicals and instruments

All reactants of A.R. grade were obtained commercially and used without further purification. The fluorescent data were collected at room temperature on a computer-controlled JY FluoroMax-3 spectrometer. The UV–Vis spectra were recorded at room temperature in the

wavelength range 190–1100 nm using a computer-controlled PE Lambda 900 UV–Vis spectrometer equipped with an integrating sphere. A $BaSO_4$ plate was used as the reference (100 % reflectance), on which the finely ground powder of the samples were coated. The absorption spectra were calculated from the reflection spectra by the Kubelka-Munk function:[14,15] $\alpha/S = (1 - R)^2/2R$, where α is the absorption coefficient, S is the scattering coefficient, which is practically wavelength independent when the particle size is larger than 5 μm, and R is the reflectance.

Preparation of $[\{Eu(NC_5H_4COOH)_3(H_2O)_2\}(1.5ZnCl_4)\cdot(2H_2O)]_n$

The title complex was prepared by mixing $EuCl_3\cdot 6H_2O$ (1.0 mmol, 0.37 g), $ZnCl_2$ (1.0 mmol, 0.14 g), isonicotinic acid (1.00 mmol, 0.123 g) and 10 mL distilled water in a 25 mL Teflon-lined stainless steel autoclave and heated at 200 °C for 3 days. After slow cooling to room temperature at 6 °C/h, colourless crystals suitable for X-ray analysis were obtained. The yield was 88 % (based on europium).

Crystallography

The intensity data set was collected on a Rigaku Mercury CCD X-ray diffractometer with graphite monochromated Mo-$K\alpha$ radiation (λ = 0.71073 Å) using the ω scan technique. CrystalClear software was used for data reduction and empirical corrections for absorption.[16] The structure was solved by the direct method using the Siemens SHELXTL™ , version 5, package of crystallographic software.[17] The difference Fourier maps based on these atomic positions yielded the other non-hydrogen atoms. The hydrogen atom positions were generated theoretically, except for those of the lattice water molecules, which were obtained by difference Fourier maps allowed to ride on their respective parent atoms and included in the structure factor calculations with assigned isotropic thermal parameters but they were not refined. The structures were refined using a full-matrix least-squares refinement on F^2. All atoms were refined anisotropically. The crystallographic data are given in Table I and selected bond distances and bond angles are given in Table II (CCDC 666795).

TABLE I. Crystal data[a] and structure refinement details for **1**

Property	Value
Formula	$C_{18}H_{23}Cl_6EuN_3O_{10}Zn_{1.5}$
Formula weight, g mol^{-1}	904.11
Colour	Colourless
Crystal size, mm^3	0.40; 0.30; 0.20
Crystal system	Monoclinic
Space group	*C*2/*c*
a / Å	23.878(8)
b / Å	20.573(6)
c / Å	15.358(5)
β / °	127.276(5)
V / Å^3	6003(3)
Z	8
$2\theta_{max}$ / °	50.12
Index ranges	$-22\leq h\leq 28$, $-24\leq k\leq 24$, $-18\leq l\leq 17$
Reflections collected	18023
Independent, observed reflections (R_{int})	5236, 4947 (0.0232)
$d_{calcd.}$ / gcm^{-3}	2.001
μ / mm^{-1}	3.846

TABLE I. Continued

Property	Value
T / K	293(2)
F(000)	3536
$R1$, $wR2$	0.0270, 0.0672
S	1.077
Largest and mean Δ/σ	0.002, 0
$\Delta\rho$(max, min) /eÅ^{-3}	1.906, –1.494

TABLE II. Selected interatomic distances and bond angles Åt^0 for **1**

Eu1–O1	2.376(2)	O5–C13	1.246(2)
Eu1–O2#1	2.357(2)	O6–C13	1.251(2)
Eu1–O3	2.363(2)	Cl1–Zn1–Cl2	107.75(3)
Eu1–O4#2	2.389(2)	Cl3–Zn1–Cl1	109.04(3)
Eu1–O5	2.412(2)	Cl3–Zn1–Cl2	109.62(2)
Eu1–O6#1	2.395(2)	Cl4–Zn1–Cl1	113.25(3)
Eu1–O1W	2.453(2)	Cl4–Zn1–Cl2	106.81(3)
Eu1–O2W	2.513(2)	Cl4–Zn1–Cl3	110.28(3)
Zn1–Cl1	2.2696(9)	Cl5–Zn2–Cl6	89.77(6)
Zn1–Cl2	2.3139(9)	Cl5–Zn2–Cl7	105.22(6)
Zn1–Cl3	2.2663(9)	Cl6–Zn2–Cl7	107.96(5)
Zn1–Cl4	2.266(1)	Cl7#3–Zn2–Cl5	135.10(5)
Zn2–Cl5	2.205(2)	Cl7#3–Zn2–Cl6	107.12(6)
Zn2–Cl6	2.261(2)	Cl7#3–Zn2–Cl7	108.22(6)
Zn2–Cl7	2.396(1)	C1–O1–Eu1	132.9(1)
Zn2–Cl7#3	2.396(1)	C1–O2–Eu1#1	157.0(1)
O1–C1	1.246(2)	C7–O3–Eu1	171.4(1)
O2–C1	1.239(2)	C7–O4–Eu1#2	126.2(2)
O3–C7	1.258(3)	C13–O5–Eu1	144.9(2)
O4–C7	1.246(2)	C13–O6–Eu1#1	137.3(1)

RESULTS AND DISCUSSION

Crystal structure

X-ray diffraction analysis revealed that the structure of the title complex consisted of $\{Eu(NC_5H_4COOH)_3(H_2O)_2\}^{3+}$ chains, $[ZnCl_4]^{2-}$and lattice water molecules, as shown in Fig. 1. The Zn1 atom is tetrahedrally bonded to four chlorine atoms to form the $[ZnCl_4]^{2-}$. The Zn2 atom is positionally disordered and the occupancy of Zn2 had to be set to 0.5 in order to obtain a rational structure model and thermal displacement parameters. The bond lengths of Zn–Cl range from 2.205(2) to 2.396(1) Å with an average value of 2.297(2) Å, which are normal and similar to the counterparts found in the literature.[18–21] The europium atom is coordinated to eight oxygen atoms, of which two are from the two water molecules and six are from the six isonicotinic acid ligands, yielding a distorted square anti-prism with the top and bottom planes defined by O(2)(1–x, y, 1/2–z), O(1), O(5), O(6)(1–x, y, 1/2–z), and O(2W), O(3), O(1W) and O(4)(1/2–x, –1/2–y,

–*z*) atoms, respectively. The bond lengths of Eu–$O_{isonicotinic\ acid}$ range from 2.357(2) to 2.412(2) Å, with an average value of 2.382(2) Å, which is obviously shorter than that of Eu–O_{water}, being of 2.453(2) and 2.513(2) Å, indicating that the isonicotinic acid ligand has a stronger affinity to the Eu(III) ion than water. For the requirement of charge balance, all isonicotinic fragments are protonated at the nitrogen atom. The europium atoms are alternately bridged by two or four μ_2-isonicotinic acid ligands in a 2-4-2 (the number indicates the number of the bridges) mode to construct a 1D polycationic chain with Eu···Eu distances of 4.986(2) and 4.568(1) Å, respectively (Fig. 2 and Scheme 1d). It is noteworthy that, to date, the documented types of chains formed by LN and isonicotinic acid are mainly 1-1-1, 2-1-2 and 2-2-2 types (Schemes 1a, 1b and 1c, respectively). There are five kinds of hydrogen bonds in **1**, *i.e.*, O···Cl, O···O, O···N, N···Cl and Cl···Cl hydrogen bonds, including O1W···Cl1 (1/2–*x*, –1/2+*y*, 1/2–*z*), O2W···Cl2 (*x*, –*y*, –1/2+*z*), O2W···O4W, O3W···Cl4 (1/2–*x*, –1/2–*y*, 1–*z*), O3W···O3W (1–*x*, *y*, 3/2–*z*), O3W···N3, O4W···Cl3 (*x*, *y*, –1+*z*), O4W···Cl4 (*x*, –*y*, –1/2+*z*), N1···Cl2, N1···Cl5, N2···Cl3 and HC15···Cl6, with the hydrogen bond distances being of 3.205(2), 3.235(2), 2.727(3), 3.245(2), 2.983(3), 2.858(3), 3.234(3), 3.236(3), 3.191(3), 3.286(3), 3.318(3) and 3.027(3) Å, respectively. The 1D polycationic chains, $[ZnCl_4]^{2-}$ moieties and the water molecules are linked *via* hydrogen bonds to yield a 3D network (Fig. 3).

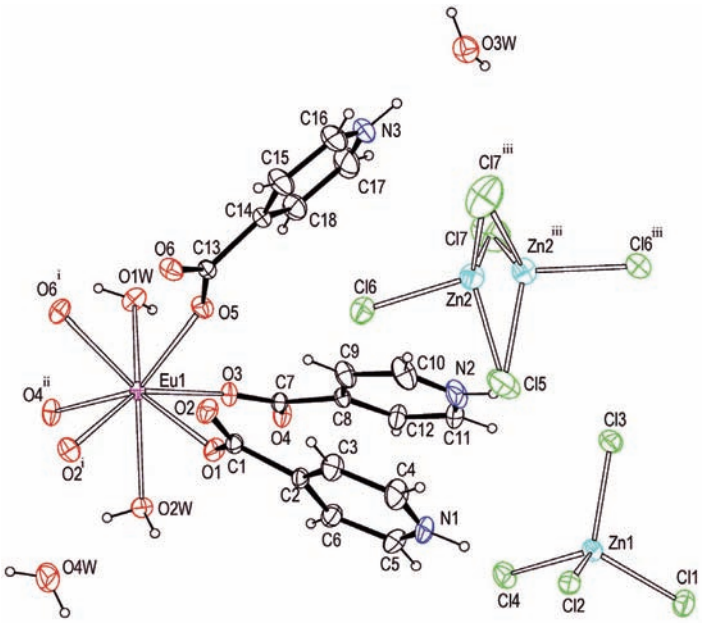

Fig. 1. ORTEP-plot of **1** with 30 % thermal ellipsoids. The small spheres represent hydrogen atoms. Disordered $Cl5^{iii}$ are omitted for clarity. The occupancies of Zn2, Cl5 and Cl6 are set to 0.5. Symmetry codes: i) 1–*x*, *y*, 1/2–*z*; ii) 1/2–*x*, –1/2–*y*, –*z*; iii) 1–*x*, *y*, 3/2–*z*.

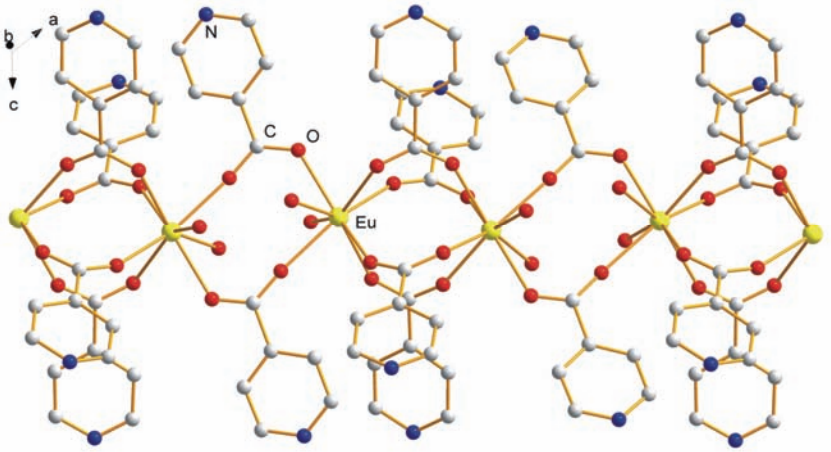

Fig. 2. The 1D cationic chain-like structure of **1**.

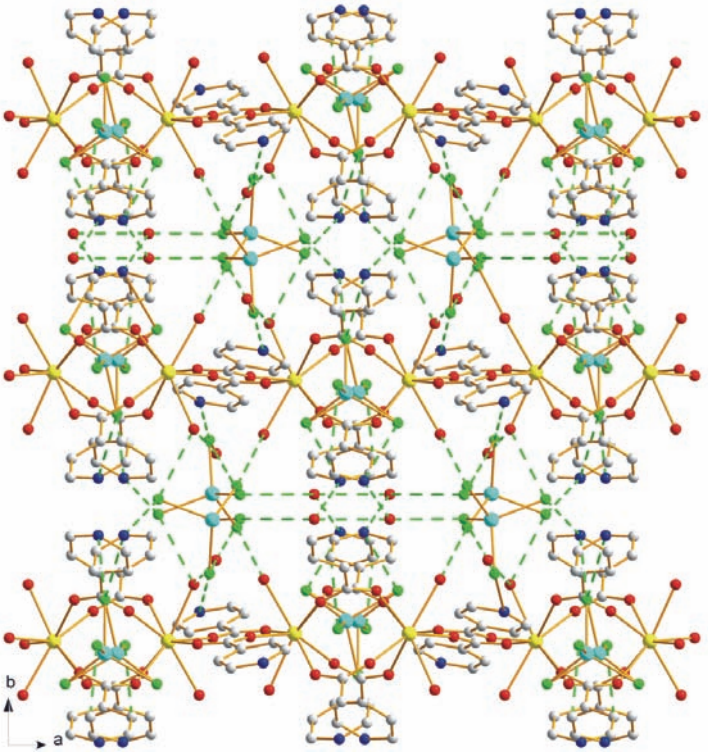

Fig. 3. Packing diagram of **1** with the dashed lines representing hydrogen bonds (Å): O1W···Cl1 (1/2–*x*, –1/2+*y*, 1/2–*z*), 3.205(2); O2W···Cl2 (*x*, –*y*, –1/2+*z*), 3.235(2); O2W···O4W, 2.727(3); O3W···Cl4 (1/2–*x*, –1/2–*y*, 1–*z*), 3.245(2); O3W···O3W (1–*x*, *y*, 3/2–*z*), 2.983(3), O3W···N3 2.858(3), O4W···Cl3 (*x*, *y*, –1+*z*) 3.234(3); O4W···Cl4 (*x*, –*y*, –1/2+*z*), 3.236(3); N1···Cl2, 3.191(3); N1···Cl5, 3.286(3); N2···Cl3, 3.318(3) and C15···Cl6, 3.027(3).

To our knowledge, isonicotinic acid is a quite interesting tecton in constructing extended structures because it is an unsymmetrical, divergent ligand with a nitrogen atom at one end and two oxygen atoms from the carboxylato group at the other. Isonicotinic acid can link two metal centres by coordinating to a metal centre with the nitrogen atom and to the other one with one or two carboxylato oxygen atoms.[22,23] Therefore, an attempt was made to employ isonicotinic acid as a ligand to bridge LN and IIB metal centres. Unfortunately, the isonicotinic acid only coordinated to LN centres, while the IIB atoms did not link to the isonicotinic acid ligand. The reason for this can probably be ascribed to the experimental conditions. It is believed that the isonicotinic acid ligand would bridge LN and IIB atoms together if the changing experimental conditions, such as temperature and solvent, were changed. Further systematic experimental and theoretical investigations on this system are currently in progress.

Photoluminescent properties

Taking into account the excellent luminescent property of the Eu^{3+}, the luminescence of **1** was investigated at room temperature (Fig. 4). The solid-state excitation spectra of the title complex show that the effective energy absorption mainly occurs in the long wavelength ultraviolet region in the range 280–360 nm (inner plot of Fig. 4). The excitation bands of complex **1** under the red emission of 613 nm possess two main bands, at 288 and 346 nm. The corresponding emission spectra were further measured by selective excitation with the different excitation wavelengths of the title complex and they showed a similar emission position with only small differences in the luminescent intensities, which indicates that the excitation bands are all effective energy sensitizer for the luminescence of the Eu^{3+}. The emission spectrum is shown in the outer plot of Fig. 4. For complex **1**, the emission spectra show two main and intense emission bands under excitation by 346 nm: 592 and 613 nm light, corresponding to the characteristic emission of $^5D_0$–^7F_J transitions (J = 1,2) of the Eu^{3+}. This indicates that effective energy transfer occurred and that conjugated systems formed between the ligands and the chelated lanthanide ions in **1**. Moreover, the absence of a ligand-based emission in the fluorescence spectra of **1** also suggests that energy transfer from the ligand to the lanthanide centre is effective. Among the red luminescent intensity of $^5D_0$–$^7F_2$, the electric dipole transition is the strongest and the orange emission intensity of the $^5D_0$–$^7F_1$ magnetic dipole transition becomes stronger by the overlap of the $^5D_0$–$^7F_0$ transition. For the title complex, the spectra were not ideal enough because the two bands of the emission spectra corresponding to the emissions originating from the $^5D_0$–^7F_J transitions (J = 1,2) of the Eu^{3+} were not completely separated; they meet at 602 nm. The overlap of the two transitions and the small shoulder band of the $^5D_0$–$^7F_2$ transition suggest that the isonicotinic acid ligand is not perfect for the sensitization of Eu^{3+}.

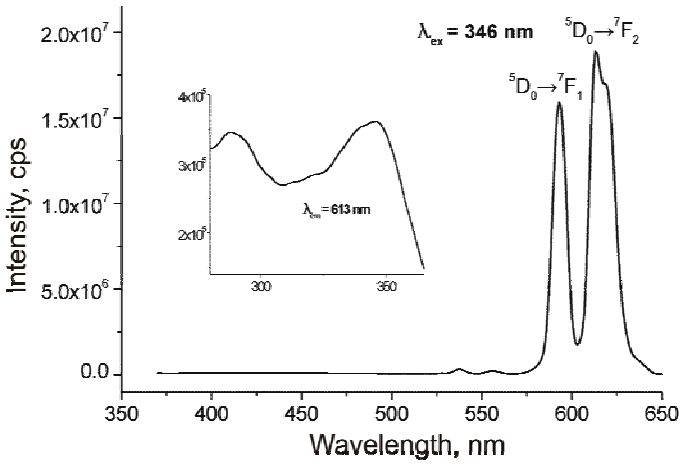

Fig. 4. Luminescent spectra of the title complex: outer plot, emission spectrum and inner plot, excitation spectrum.

Solid-state diffuse reflectance spectrum

The optical absorption spectrum of **1** revealed the presence of an obvious optical gap of 3.56 eV (Fig. 5), which suggests that complex **1** may be a potential wide-gap semiconductor, which is consistent with the colour of the crystal, as for cases found in the literature.[24] The steep slope of the optical absorption edge for **1** is indicative of the existence of direct transitions.[25] The optical absorption of **1** most likely originates from charge-transfer excitations, mainly from the p-like valence band of the chloride ligands to the 4s-like conduction band of the zinc centre, similar to those reported in the literature.[26–28]

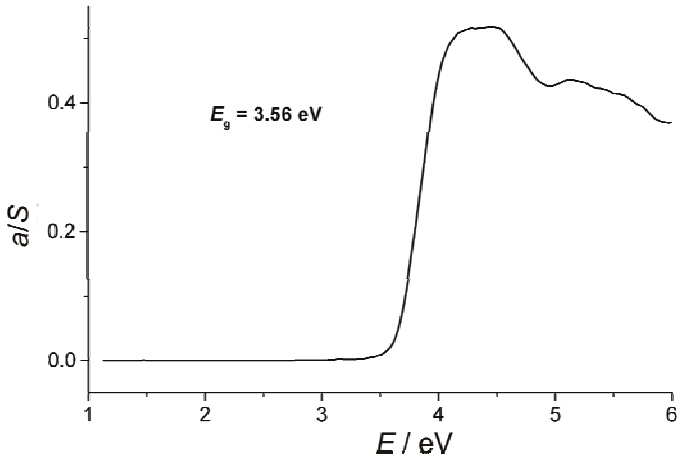

Fig. 5. Solid-state diffuse reflectance spectrum of **1**.

CONCLUSIONS

In brief, a metal–isonicotinic acid inorganic–organic hybrid complex was prepared *via* a hydrothermal reaction. The crystal structure of the title complex is characteristic for a novel one-dimensional polycationic chain-like structure. The title complex shows intense red luminescence at around 613 nm, corresponding to the $^5D_0$–$^7F_2$ transition under UV excitation. Therefore, it may be expected that the title lanthanide functional complex could lead to the fabrication of high-quality colour displays and be rather useful as a source of monochromatic emission in photonic crystals. The optical absorption spectra show that the title complex may be a candidate for potential photoelectric materials.

Acknowledgements. We gratefully acknowledge the financial support of the NSF of Jiangxi Province (200007GQH1685) and the science and technology project of Jiangxi Provincial Department of Education (GJJ08412).

ИЗВОД

СИНТЕЗА, СТРУКТУРА, ПОЛУПРОВОДНИЧКА И ФОТОЛУМИНИСЦЕНТНА СВОЈСТВА $[\{Eu(NC_5H_4COOH)_3(H_2O)_2\}(1,5ZnCl_4)\cdot(2H_2O)]_n$

WEN-TONG CHEN, XIAO-NIU FANG, QIU-YAN LUO и YA-PING XU

School of Chemistry and Chemical Engineering, Jinggangshan University, 343009, Ji'an, Jiangxi, P.R. China

Хидротермалном реакцијом добијен је нови диметални 4f–3d метал–изоникотинска киселина органско–неорганski хибридни комплекс $[\{Eu(NC_5H_4COOH)_3(H_2O)_2\}(1.5ZnCl_4)\cdot(2H_2O)]_n$ (**1**) и структурно окарактерисан X-рендгенском дифракционом анализом на моно-кристалу. Комплекс кристалише у просторној групи *C*2/*c* моноклиничког система са 8 формулских јединица у ћелији: a = 23,878(8) Å, b = 20,573(6) Å, c = 15,358(5) Å, β = 127,276(5)°, V = 6003(3) Å^3, $C_{18}H_{23}Cl_6EuN_3O_{10}Zn_{1.5}$, M_r = 904,11 g/mol, ρ = 2,001 g/cm^3, S = 1,077, μ(Mo$K\alpha$) = 3,846 mm^{-1}, F(000) = 3536, R = 0,0270 и wR = 0,0672. Комплекс је карактеристичан по једно-димензионалној поликатјонској ланчастој структури. Фотолуминисцентна испитивања потврдила су да наведени комплекс показује интензивну емисију у наранџастој и црвеној области. Луминисцентни спектри показују јачу црвену него наранџасту емисију. Оптички апсорпциони спектар комплекса **1** има оптички пад од 3,56 eV.

(Примљено 18. новембра 2008, ревидирано 20. фебруара 2009)

REFERENCES

1. M. Fujita, Y. J. Kwon, S. Washizu, K. Ogura, *J. Am Chem. Soc.* **116** (1994) 1151
2. K. M. Dunbar, R. A. Heintz, *Prog. Inorg. Chem.* **45** (1997) 283
3. M. Eddaoudi, D. B. Moler, H. Li, B. Chen, T. M. Reinecke, M. O'Keeffe, O. M. Yaghi, *Acc. Chem. Res.* **34** (2001) 319
4. J. Kido, Y. Okamoto, *Chem. Rev*. **102** (2002) 2357
5. R. Reyes, E. N. Hering, M. Cremona, C. F. B. Silva, H. F. Brito, C. A. Achete, *Thin Solid Films* **23** (2002) 420
6. M. J. Zaworotko, *Chem. Soc. Rev.* (1994) 283
7. G. B. Gardner, D. Venkataraman, J. S. Moore, S. Lee, *Nature* **374** (1995) 792
8. C. Janiak, *Angew. Chem. Int. Ed. Engl.* **36** (1997) 1431
9. O. M. Yaghi, H. Li, C. Davis, D. Richardson, T. L. Groy, *Acc. Chem. Res.* **31** (1998) 474

10. S. R. Batten, R. Robson, *Angew. Chem., Int. Ed. Engl.* **37** (1998) 1460
11. W. Lin, O. R. Evans, R. G. Xiong, Z. Wang, *J. Am. Chem. Soc.* **120** (1998) 13272
12. O. R. Evans, R. G. Xiong, Z. Wang, G. K. Wong, W. Lin, *Angew. Chem. Int. Ed. Engl.* **38** (1999) 536
13. T. M. Reineke, M. Eddaoudi, M. Fehr, D. Kelley, O. M. Yaghi, *J. Am. Chem. Soc.* **121** (1999) 1651
14. W. W. Wendlandt, H. G. Hecht, *Reflectance Spectroscopy*, Interscience Publishers, New York, 1966
15. G. Kortüm, *Reflectance Spectroscopy*, Springer Verlag, New York, 1969
16. Rigaku, CrystalClear, version 1.35, Rigaku Corporation, 2002
17. Siemens, SHELXTL^{TM}, version 5, Reference Manual, Siemens Energy & Automation Inc., Madison, WI, 1994
18. A. Bino, F. A. Cotton, Z. Dori, M. Shaia-Gottlieb, M. Kapon, *Inorg. Chem.* **27** (1988) 3592
19. A. J. Dickie, D. C. R. Hockless, A. C. Willis, J. A. McKeon, W. G. Jackson, *Inorg. Chem.* **42** (2003) 3822
20. Z. Tao, Q.-J. Zhu, S.-F. Xie, W. G. Jackson, Z.-Y. Zhou, X.-G. Zhou, *Polyhedron* **22** (2003) 1603
21. A. Dogan, B. Sarkar, A. Klein, F. Lissner, T. Schleid, J. Fiedler, S. Zalis, V. K. Jain, W. Kaim, *Inorg. Chem.* **43** (2004) 5973
22. J. Y. Lu, A. M. Babb, *Chem. Commun.* (2001) 821
23. M. E. Chapman, P. Ayyappan, B. M. Foxman, G. T. Yee, W. Lin, *Cryst. Growth Des.* **1** (2001) 159
24. E. A. Axtell, Y. Park, K. Chondroudis, M. G. Kanatzidis, *J. Am. Chem. Soc.* **120** (1998) 124
25. F. Q. Huang, K. Mitchell, J. A. Ibers, *Inorg. Chem.* **40** (2001) 5123
26. J.-H. Liao, M. G. Kanatzidis, *Chem. Mater.* **5** (1993) 1561
27. T. J. McCarthy, X. Zhang, M. G. Kanatzidis, *Inorg. Chem.* **32** (1993) 2944
28. E. A. Axtell, Y. Park, K. Chondroudis, M. G. Kanatzidis, *J. Am. Chem. Soc.* **120** (1998) 124.

Journal of the Serbian Chemical Society
JSCS@tmf.bg.ac.rs • www.shd.org.rs/JSCS

J. Serb. Chem. Soc. 74 (7) 765–771 (2009) UDC 547.534+547.686+547.315.2+539.124:530.18
JSCS–3874 *Original scientific paper*

On π-electron conjugation in the five-membered ring of fluoranthene-type benzenoid hydrocarbons

IVAN GUTMAN*# and JELENA ĐURĐEVIĆ

Faculty of Science, University of Kragujevac, P.O. Box 60, 34000 Kragujevac, Serbia

(Received 17 February 2009)

Abstract: A fluoranthene-type benzenoid hydrocarbon (FTBH) is a polycyclic conjugated system obtained by joining two ordinary benzenoid hydrocarbons so as to form a five-membered ring. The main differences between the π-electron properties of FTBHs and those of ordinary benzenoid hydrocarbons are caused by this five-membered ring. The most important structural factors influencing the π-electron conjugation in the five-membered ring of FTBHs were analyzed and established.

Keywords: fluoranthene-type hydrocarbons; benzenoid hydrocarbons; PCP-effect; linear effect.

INTRODUCTION

Our recent theoretical studies[1–6] of fluoranthene-type benzenoid hydrocarbons (FTBHs) were motivated by the fact that whereas the π-electron properties of ordinary benzenoid hydrocarbons have been investigated for almost an entire century (see the books,[7–9] the reviews,[10–13] the recent papers,[14–18] and the references cited therein), the paper[1] seems to be the very first systematic research of FTBHs.

Fluoranthene-type benzenoid hydrocarbons (FTBHs) and ordinary benzenoid hydrocarbons are structurally closely related. The former can be viewed as being obtained by connecting two ordinary benzenoid fragments so as to form a new five-membered ring. The general structure of an FTBH is depicted in Fig. 1, in which the notation and terminology used throughout this work are also explained.

ON KEKULÉ STRUCTURES OF FLUORANTHENE-TYPE BENZENOIDS

If the two benzenoid fragments (denoted by **X** and **Y**, *cf.* Fig. 1) in an FTBH (denoted by **F**, *cf.* Fig. 1) both have Kekulé structures, then the Kekulé structure

* Corresponding author. E-mail: gutman@kg.ac.rs
# Serbian Chemical Society member.
doi: 10.2298/JSC0907765G

count of **F** is simply the product of the Kekulé structure counts of **X** and **Y**, $K(\mathbf{F}) = K(\mathbf{X})\cdot K(\mathbf{Y})$. In addition, the two carbon–carbon bonds by which **X** and **Y** are joined are single in all Kekulé structures. This gives the impression that the π-electron systems of the fragments **X** and **Y** are mutually independent and that the interaction between them (*via* the five-membered ring) is negligible. An illustrative example is provided in Fig. 2.

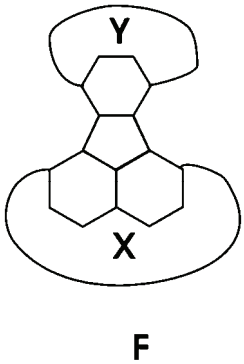

Fig. 1. The general form of a fluoranthene-type benzenoid hydrocarbon, **F**. It is obtained by joining two benzenoid systems (**X** and **Y**), so as to form a new five-membered ring. The fragments **X** and **Y** in **F** are referred to as "female" and "male", respectively.

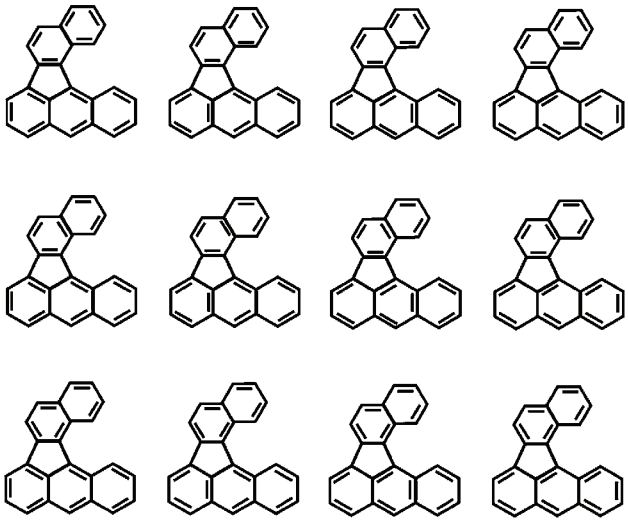

Fig. 2. The twelve (= 4×3) Kekulé structures of dibenzo[*a*,*l*]fluoranthene, composed of an anthracene (**X**) and a naphthalene (**Y**) fragment. The two carbon–carbon bonds connecting the anthracene and naphthalene fragments (thus belonging to the five-membered ring) are single in all Kekulé structures.

The fact that the two bonds connecting the benzenoid fragments **X** and **Y** are single in all Kekulé structures might be the main reason why theoreticians have for so long neglected FTBHs. Namely, according to the currently most often em-

ployed approaches in the theory of benzenoid hydrocarbons (based on Kekulé structure counts, conjugated circuits, and Clar aromatic sextet formulas, for details see[7,12]), the π-electron conjugation in the five-membered ring of an FTBH would be zero or, saying this in a more cautious manner, very weak. In reality, the extent of π-electron conjugation in the five-membered ring of FTBHs is small, but far from negligible. The magnitude of this conjugation in a peculiar manner depends on the structure of **X** and **Y**, and on the manner in which these fragments are connected (see below).

At this point it should be mentioned that if the fragments **X** and **Y** are not Kekuléan, but **F** is, then either one or both the carbon–carbon bonds connecting **X** and **Y** must be double in all Kekulé structures of **F**. Examples illustrating this case are to be found in Fig. 3. An example of an FTBH in which all five carbon––carbon bonds of the five-membered ring are single in all Kekulé structures is also shown in Fig. 3.

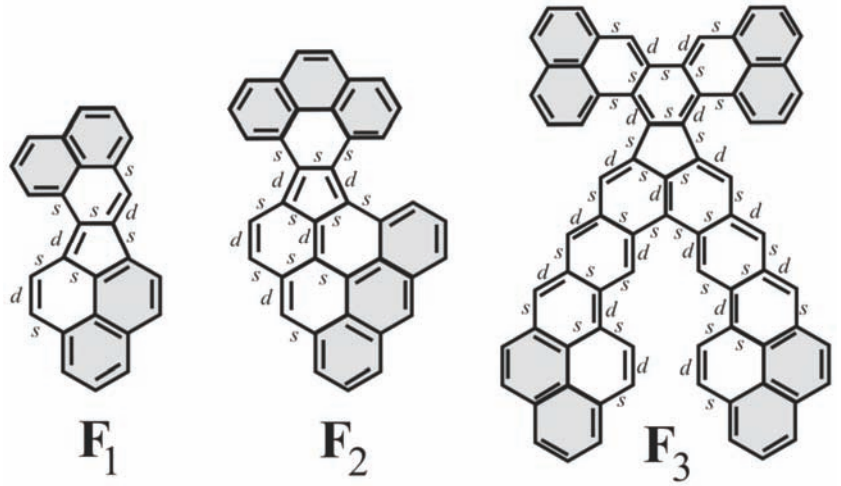

Fig. 3. Diagram $\mathbf{F}_1$ is a Kekulé structure (of the 9 possible) of an FTBH in which both benzenoid fragments **X** and **Y** are non-Kekuléan, $K(\mathbf{X}) = K(\mathbf{Y}) = 0$. Diagram $\mathbf{F}_2$ is a Kekulé structure (of the 20 possible) of an FTBH in which the benzenoid fragment **X** is non-Kekuléan, $K(\mathbf{X}) = 0$, whereas the fragment **Y** is Kekulèan, $K(\mathbf{Y}) > 0$. Diagram $\mathbf{F}_3$ is a Kekulé structure (of the 27 possible) of an FTBH in which both benzenoid fragments **X** and **Y** are Kekuléan, $K(\mathbf{X}) > 0$, $K(\mathbf{Y}) > 0$. In this FTBH, all the five carbon–carbon bonds of the five-membered ring are single in all Kekulé structures. The carbon–carbon bonds which are single and double in all Kekulé structures are marked by *s* and *d*, respectively. The domains without fixed single and double bonds are indicated by shading.

ON CYCLIC CONJUGATION IN THE FIVE-MEMBERED RING

The extent of cyclic conjugation in a ring of a polycyclic conjugated molecule can be assessed by means of its energy effect (*ef*). Details of the calculation

of this energy effect can be found in the review,[19] recent papers,[3,5,20] and the references cited therein. For what follows, it is important that the *ef*-values are computed using a Coulson-integral based molecular orbital method, which is free of any *a priori* assumptions concerning Kekulé structures. Positive *ef*-values indicate stabilization, and the greater is the *ef*, the greater is the magnitude of the cyclic conjugation in the underlying ring.

Cyclic conjugation in the five-membered ring of FTBHs was studied in detail in previous papers.[3,5,6] Therefore, only the two main findings on its structure dependency are briefly repeated here.

PCP effect.[3] The five-membered ring and a six-membered ring in an FTBH are said to be in a phenyl-cyclopentadienyl (PCP) constellation if the two rings are connected by exactly one carbon–carbon bond. Six-membered rings in a PCP constellation increase the magnitude of cyclic conjugation in the five-membered ring. The greater is the number of such six-membered rings, the greater is the *ef*-value of the five-membered ring.

Linear effect.[6] The five-membered ring and a six-membered ring in an FTBH are said to be in a linear constellation if they are separated by a six-membered ring but are not in a PCP constellation. Six-membered rings in a linear constellation decrease the magnitude of the cyclic conjugation in the five-membered ring. The greater is the number of such six-membered rings, the smaller is the *ef*-value of the five-membered ring.

Simple examples illustrating the above two effects are given in Fig. 4. Some more complex situations are shown in Figs. 5 and 6.

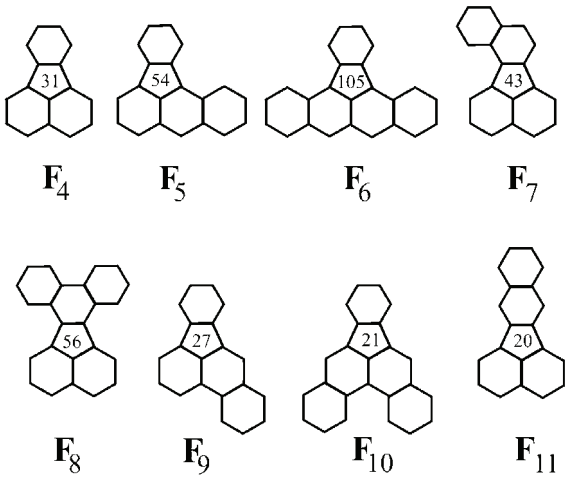

Fig. 4. Examples illustrating the PCP and linear effects in FTBHs: fluoranthene ($\mathbf{F}_4$) and its congeners with one hexagon in the PCP constellation ($\mathbf{F}_5$ and $\mathbf{F}_7$), with two hexagons in the PCP constellation ($\mathbf{F}_6$ and $\mathbf{F}_8$), with one hexagon in the linear constellation ($\mathbf{F}_9$ and $\mathbf{F}_{11}$) and two hexagons in the linear constellation ($\mathbf{F}_{10}$); in $\mathbf{F}_4$–$\mathbf{F}_8$, there are no linear constellations, in $\mathbf{F}_4$ and $\mathbf{F}_9$–$\mathbf{F}_{11}$, there are no PCP constellations. The *ef*-value of the five-membered ring (multiplied by 10000 and expressed in the units of the HMO carbon–carbon resonance integral β) is inscribed into this ring; for details see text.

From the data shown in Figs. 4–6, especially in Fig. 4, it can be seen that the linear effect is much weaker than the PCP effect. Furthermore, the PCP effect caused by hexagons in the female benzenoid fragment (*e.g.*, in $\mathbf{F}_6$ and $\mathbf{F}_7$) is much

stronger than the analogous effect caused by hexagons in the male benzenoid fragment (*e.g.*, in $\mathbf{F}_8$ and $\mathbf{F}_9$). This observation may be summarized as follows:

Male–female difference in the PCP effect.[6] A six-membered ring belonging to the female benzenoid fragment of an FTBH has a stronger PCP effect than a six-membered ring belonging to the male benzenoid fragment of the same FTBH.

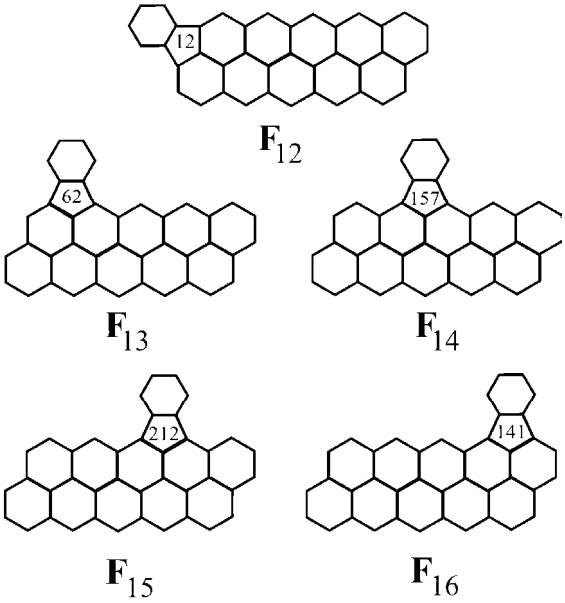

Fig. 5. The same data as in Fig. 4 for FTBHs the female and male benzenoid fragments of which are pentacenopentacene and benzene, respecttively. $\mathbf{F}_{12}$–$\mathbf{F}_{16}$ have 1, 2, 3, 3, 2 PCP constellations, and 0, 2, 2, 2, 1 linear constellations, respectively. The *ef*-values of the five-membered ring follow the increase of the number of PCP constellations. Note, however, that the *ef*-value in $\mathbf{F}_{16}$ is signifycantly greater than in the case of $\mathbf{F}_{13}$, although both $\mathbf{F}_{13}$ and $\mathbf{F}_{16}$ have an equal number of PCP constellations.

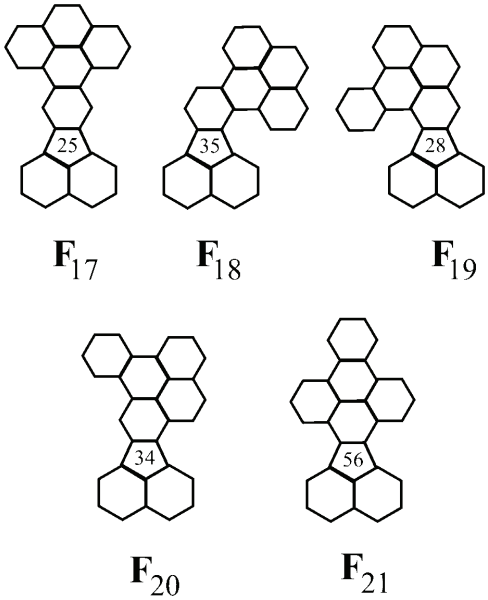

Fig. 6. The same data as in Fig. 4 for FTBHs the female and male benzenoid fragments of which are naphthalene and benzo[*b*]pyrene, respecttively. $\mathbf{F}_{17}$–$\mathbf{F}_{21}$ have 0, 1, 1, 1, 2 PCP constellations, and 1, 0, 1, 1, 1 linear constellations, respectively. The *ef*-values of the five-membered ring follow the increase of the number of PCP constellations. In agreement with the linear effect, the *ef*-value in $\mathbf{F}_{18}$ is greater than that in $\mathbf{F}_{19}$ and $\mathbf{F}_{20}$.

In order to convincingly demonstrate the validity of the above regularity, we examined pairs of FTBHs with an equal number of PCP and linear constellations, such that the female benzenoid fragment of one species and the male benzenoid fragment of the other species are identical, were examined. Two examples of this kind are depicted in Fig. 7.

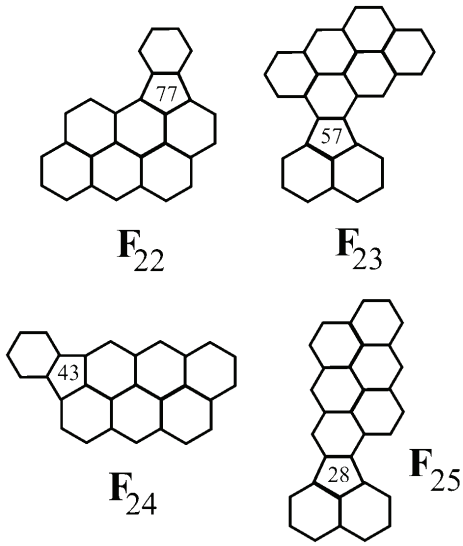

Fig. 7. The same data as in Fig. 4 for the pairs $\mathbf{F}_{22}$–$\mathbf{F}_{25}$. Both $\mathbf{F}_{22}$ and $\mathbf{F}_{23}$ possess two hexagons in the PCP constellation and one in the linear constellation. The female fragment of $\mathbf{F}_{22}$ and the male fragment of $\mathbf{F}_{23}$ are identical (= anthracenoanthracene), but the *ef*-value in $\mathbf{F}_{22}$ is much greater than in $\mathbf{F}_{23}$. Both $\mathbf{F}_{24}$ and $\mathbf{F}_{25}$ possess one hexagon in the PCP constellation and one in the linear constellation. The female fragment of $\mathbf{F}_{24}$ and the male fragment of $\mathbf{F}_{25}$ are identical (= anthracenoanthracene), but the *ef*-value in $\mathbf{F}_{24}$ is much greater than in $\mathbf{F}_{25}$. These examples confirm the existence of a male-female difference in the PCP effect.

CONCLUSIONS

The main conclusion of the present work is that, contrary to the inferences of the traditional, Kekulé-structure based, theoretical approaches,[7,12] the five-membered ring in fluoranthene-type benzenoid hydrocarbons is far from being "empty", and does possess a certain degree of π-electron conjugation. The magnitude of this conjugation, measured by its energy effect, depends in a perplexed manner on the structure and mode of condensation of the two benzenoid fragments which form the fluoranthene derivative. The most significant of these structural factors seems to have been identified.

Acknowledgement. The authors thank the Serbian Ministry of Science and Technological Development for partial support of this work, through Grant No. 144015G.

ИЗВОД

О π-ЕЛЕКТРОНСКОЈ КОНЈУГАЦИЈИ У ПЕТОЧЛАНОМ ПРСТЕНУ БЕНЗЕНОИДНИХ УГЉОВОДОНИКА ФЛУОРАНТЕНСКОГ ТИПА

ИВАН ГУТМАН и ЈЕЛЕНА ЂУРЂЕВИЋ

Природно–математички факултет Универзитета у Крагујевцу

Бензеноидни угљоводоници флуорантенског типа (FTBH) су полициклични конјуговани системи добијени спајањем два бензеноидна угљоводоника тако да се образује нови петочлани прстен. Главне разлике између π-електронских особина FTBH и бензеноидних угљоводоника узроковане су овим петочланим прстеном. У раду су анализирани и одређени најважнији структурни фактори који утичу на π-електронску конјугацију у петочланом прстену FTBH.

(Примљено 17. фебруара 2009)

REFERENCES

1. I. Gutman, J. Đurđević, *MATCH Commun. Math. Comput. Chem.* **60** (2008) 659
2. J. Đurđević, S. Radenković, I. Gutman, *J. Serb. Chem. Soc.* **73** (2008) 898
3. I. Gutman, J. Đurđević, A. T. Balaban, *Polyc. Arom. Comp.* **29** (2009) 3
4. I. Gutman, J. Đurđević, S. Radenković, A. Burmudžija, *Indian J. Chem.* **37A** (2009) 194
5. J. Đurđević, I. Gutman, R. Ponec, *J. Serb. Chem. Soc.* **74** (2009) 549
6. J. Đurđević, I. Gutman, J. Terzić, A. T. Balaban, *Polyc. Arom. Comp.* **29** (2009) 90
7. I. Gutman, S. J. Cyvin, *Introduction to the Theory of Benzenoid Hydrocarbons*, Springer--Verlag, Berlin, 1989
8. *Advances in the Theory of Benzenoid Hydrocarbons*, I. Gutman, S. J. Cyvin, Eds., Springer-Verlag, Berlin, 1990
9. *Advances in the Theory of Benzenoid Hydrocarbons II*, I. Gutman, Ed., Springer-Verlag, Berlin, 1992
10. T. Balaban, *Pure Appl. Chem.* **54** (1982) 1075
11. J. A. N. F. Gomes, R. B. Mallion, *Chem. Rev.* **101** (2001) 1349
12. M. Randić, *Chem. Rev.* **103** (2003) 3449
13. T. Balaban, P. V. R. Schleyer, H. S. Rzepa, *Chem. Rev.* **105** (2005) 3436
14. I. Gutman, B. Furtula, R. Kovačević, *J. Serb. Chem. Soc.* **72** (2007) 663
15. S. Gojak, I. Gutman, S. Radenković, A. Vodopivec, *J. Serb. Chem. Soc.* **72** (2007) 673
16. S. Stanković, J. Đurđević, I. Gutman, R. Milentijević, *J. Serb. Chem. Soc.* **73** (2008) 547
17. I. Gutman, S. Stanković, *Monatsh. Chem.* **139** (2008) 1179
18. S. Radenković, I. Gutman, *J. Serb. Chem. Soc.* **74** (2009) 155
19. I. Gutman, *Monatsh. Chem.* **136** (2005) 1055
20. I. Gutman, S. Stanković, J. Đurđević, B. Furtula, *J. Chem. Inf. Model.* **47** (2007) 776.

Journal of the Serbian Chemical Society
JSCS@tmf.bg.ac.rs • www.shd.org.rs/JSCS

J. Serb. Chem. Soc. 74 (7) 773–779 (2009)
JSCS–3875

UDC 66.088:546.26–162:531.728:53.086
Original scientific paper

Laser reflection spot as a pattern in a diamond coating – a microscopic study

GORDANA S. RISTIĆ[1*#], MILAN S. TRTICA[1#], ŽARKO D. BOGDANOV[1], ZLATKO LJ. RAKOČEVIĆ[1] and ŠĆEPAN S. MILJANIĆ[1,2]

[1]*VINČA Institute of Nuclear Sciences, P.O. Box 522, 11001 Belgrade, and* [2]*Faculty of Physical Chemistry, University of Belgrade, P.O. Box 137, 11001 Belgrade, Serbia*

(Received 3 July 2008, revised 13 March 2009)

Abstract: Diamond coatings were deposited by the synchronous and coupled action of a hot filament CVD method and a pulsed CO_2 laser in spectro-absorbing and spectro-non-absorbing diamond precursor atmospheres. The obtained coatings were structured/patterned, *i.e.*, they were comprised of uncovered, bare locations. An extra effect observed only in the spectro-active diamond precursor atmosphere was the creation of another laser spot in the coating – a reflection spot. In order to establish the practical usability of the latter one, extensive microscopic investigations were performed with consideration of the morphology changes in the spot of the direct laser beam. Normal incidence SEM images of this spot showed a smooth surface, without any pulse radiation damage. AFM imaging revealed the actual surface condition and gave precise data on the surface characteristics.

Keywords: diamond coating; hot filament CVD; CO_2 laser; radiation reflection; SEM; AFM.

INTRODUCTION

A wealth of high-valuable technological properties of diamond has become fully available in thin film form by chemical vapour deposition (CVD). The hot filament chemical vapour deposition method (hfCVD) is a simple and inexpensive approach for obtaining good quality diamond films. The joint, synchronous action of a laser – the synergy – in the course of diamond coating deposition, enables a patterned coating to be obtained in a single-step procedure without any previous or subsequent processing. The main purpose of achieving the hot filament CVD-pulse CO_2 laser synergy in the synthesis of a diamond coating is to use the hot filament for the production of atomic hydrogen in sufficient quantities and the pulse CO_2 laser as a pattern-writing agent.

* Corresponding author. E-mail: eristic@vinca.rs
# Serbian Chemical Society member.
doi: 10.2298/JSC0907773R

The synergy of the hot filament CVD method with a number of lasers operating in a broad spectral region was realised in order to obtain diamond coatings. Different lasers were used: excimer lasers ArF (193 nm)[1,2] and XeCl (308 nm);[1,3] an Ar-ion laser (514.5 nm);[4] a pulsed, frequency-doubled Nd:YAG laser (532 nm);[5,6] a continuous wave (cw) Nd:YAG laser (1064 nm);[7] a cw/pulsed CO_2 laser (10.6 μm)[8] and a pulsed CO_2 laser.[9] In all these cited works, except for two, the spectro-non-absorbing diamond precursor, CH_4 (1–3 %) in H_2 was used.

A spectro-absorbing diamond precursor atmosphere in the synergy laser–conventional CVD method takes advantage of another specific, important characteristic of laser radiation – monochromacity (in addition to high-directionality and high-intensity), which justifies the use of rather expensive/sophisticated instrument. In a spectro-absorbing diamond precursor atmosphere, the synergy of the hot filament CVD method with either an ultraviolet excimer laser[1] or an infrared-pulsed CO_2 laser[9] enables specific coating patterning – by deposition suppression, *i.e.*, impoverishment in irradiated locations. The obtaining of another laser spot in the coating, the reflection spot, indicated a possibility of exploiting the beneficial and avoiding the detrimental effects of pulse laser radiation. An SEM comparison of the spots created by the direct laser beam and by the reflected laser beam showed the absence of any substrate surface damage in the latter case. Microscopic investigations of the reflection spot down to the nano-scale were additionally undertaken in order to ascertain the substrate surface quality required for applications in diamond coating technologies.

EXPERIMENTAL

A reaction cell with a hot filament and a TEA pulsed CO_2 laser were set opposite to each other on the same optical axis, in order to accomplish their synergy. The reaction cell with the hot filament was coupled to a vacuum apparatus equipped with a pump, a pressure gauge and a gas flowmeter. The Ta filament (0.5 mm diameter) was supplied with electrical current from the a.c. mains through variable transformers. Molybdenum was chosen as the target/substrate in all synergy experiments, based on a study of different substrate materials for diamond CVD.[10] The Mo substrate (20 mm×10 mm×0.5 mm), mirror-polished by a standard metallographic procedure, unseeded, was mounted at a distance about 5 mm from the filament. The working parameters were as follows: substrate temperature ≈ 900 °C, filament temperature 2100–2200 °C, total working pressure 30 mbar, gas flow rate 50 cm^3 min^{-1}, experiment duration $t_{dep} = t_{irr} = 2.5$ h. Gaseous mixtures, C_2H_4 (0.5 %) in H_2, C_2H_4 (7.5 %) in H_2 and CH_4 (1 %) in H_2, were prepared before the experiments.

Radiation of the pulsed TEA CO_2 laser[11] was focused by a ZnSe lens (f = 25 cm) onto the Mo target/substrate mounted in the reaction cell at a distance from the filament of ≈ 1–2 mm. The laser working characteristics were as follows: pulse power (at a spike) 0.5 MW; pulse duration 120 ns (initial spike), ≈ 2 μs (pulse "tail"); repetition rate ≈ 3 Hz; output wavelength 10.6 μm; multimode working regime; spot size at the focus ≈ 1 mm^2; beam incidence angle to the surface 90°.

Characterisation of the resulting diamond coatings was performed by scanning electron microscopy (Jeol JSM 35, accelerating voltage 25 kV). The topography of the uncovered

substrate surface in the reflection spot was imaged by a powerful, high-resolution AFM instrument, Digital Nanoscope (Nanotec Electronica, Spain), working with WSxM software.[12]

RESULTS AND DISCUSSION

The diamond coating was deposited by the simultaneous action of the hot filament and the pulsed CO_2 laser from the spectro-absorbing diamond precursor atmosphere, C_2H_4 (0.5 %) in H_2. The obtained coating contained two laser spots situated in regions of reduced thickness. The first spot was created at the focus of the direct laser beam. Deposition impoverishment in the spot surrounding and moderation of the photothermal effect in the spot centre were explained by absorption of the laser beam in ethene.[9]

The second spot, made synchronously with the first one, is presented in the SEM micrographs shown in Figs. 1a–1d. The whole spot can be seen in Fig. 1a. A "patch deposit" gathered in the middle point of the spot is shown in Fig. 1b. The diffuse spot border and the gradual crystallites rarefaction indicate the influence of the spectro-active agent during the deposition, Fig. 1c. A detail from

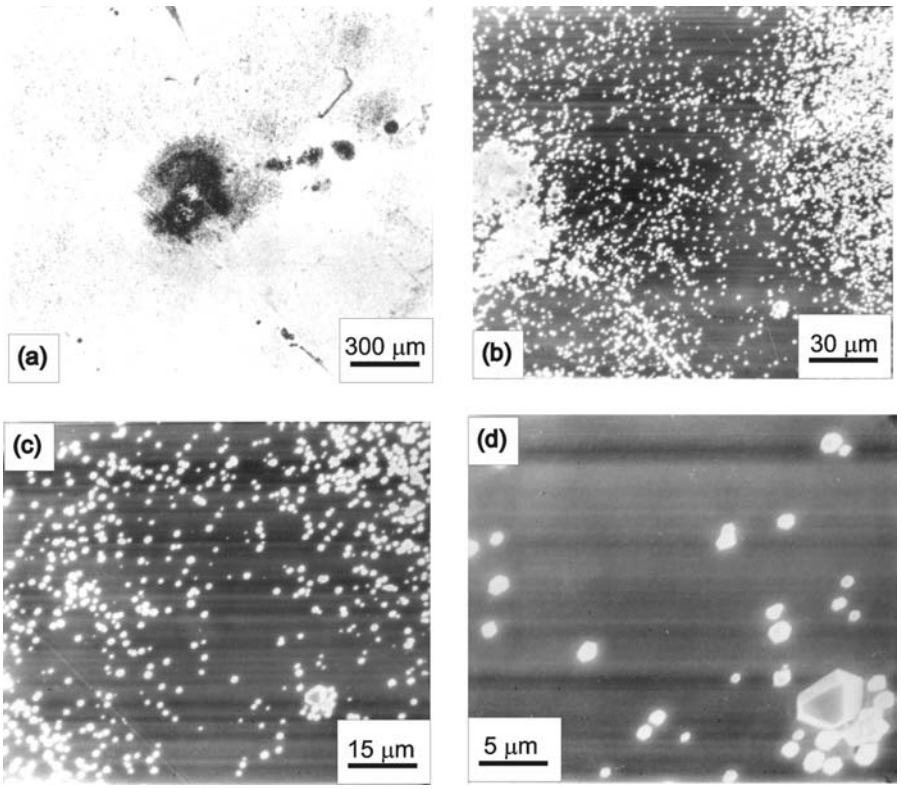

Fig. 1. Diamond coating of synergy obtained from C_2H_4 (0.5 %) in H_2: a) whole reflection spot; b) patch deposit in the central point of the spot; c) diffuse spot boundary; d) details from this spot.

the spot is shown in Fig. 1d. This spot resulted from specular reflection at the mirror-finished Mo substrate and backward reflection at the laser output coupler. It is well known that the reflectivity of metals increases with increasing incident radiation wavelength, and that for a CO_2 laser, the radiation reflectivity approaches unity (for molybdenum R = 0.985[13]). After specular reflection at the Mo substrate, the radiation reverted through the lens, become defocused after the focal point, *i.e.*, diverged, and reached the Ge output coupler* placed at an over-focus. At the coupler, the radiation is partly cast back, the straying rays travelled the same optical way, and then converged to create the reflection spot, and a cycle recurred until being extinguished by the absorbing medium. The speckle deposit in the spot centre, Figs. 1a and 1b, means that the laser radiation did not act at this point, which might indicate a possibility of a self-absorption effect of the laser radiation. On the other hand, deposition impoverishment in the spot stands just for action of the laser.[1,9] At the same time, the uncovered substrate surface in the spot without cracks produced by the pulse laser radiation, Figs. 1c and 1d, seemed as an acceptable/promising outcome of the laser action – a diamond coating pattern.

In order to compare laser modifications of the substrate surface effected in different working atmospheres, SEM micrographs (of the same/higher magnification) of the examined spot centres are given in Figs. 2a–2d. The modified substrate surface from the synergy experiment in the spectro-inactive diamond precursor atmosphere, CH_4 (1 %) in H_2 is presented in Fig. 2a. Figure 2b originnates from the spot made at the direct laser beam focus, and Fig. 2c stems from the reflection spot; both spots were created in the spectro-absorbing diamond precursor atmosphere, C_2H_4 (0.5 %) in H_2. The spot made at the laser beam focus in the highly concentrated diamond precursor atmosphere, C_2H_4 (7.5 %) in H_2 is shown in Fig. 2d. The effects of the laser radiation in the resulting coatings differ considerably: in the methane atmosphere, a laser radiation fluence of 15 J cm^{-2} produced the shown morphology pattern on the surface after removal of the diamond coating, Fig. 2a. In C_2H_4 (0.5 %) in H_2, the "palliated" surface morphology in the spot centre created at the direct laser beam focus, Fig. 2b, reveals damping of the laser radiation in the optically dense medium (simultaneously, the coating impoverishment in the spot surroundings confirms draining of the diamond precursor into a photolytic reaction channel), as has already been explained.[9] In the reflection spot, Fig. 2c, no cracks in the uncovered surface are visible; they might have vanished by radiation moving to and fro in the spectro-absorbing diamond precursor/medium. Only faint marks/traces of surface cracking seen in the spot centre created at the direct laser beam focus in C_2H_4 (7.5 %) in H_2, Fig. 2d, confirm the already noticed damping effect of the laser radiation in the

* Ge output coupler, transmission (declared): 20 %.

spectro-absorbing atmosphere.* These micrographs indicated the convenience of using the radiation reflection effect in the spectro-active diamond precursor in the studied synergy: diamond coating deposition with simultaneous patterning, without underlying surface damage to the substrate.

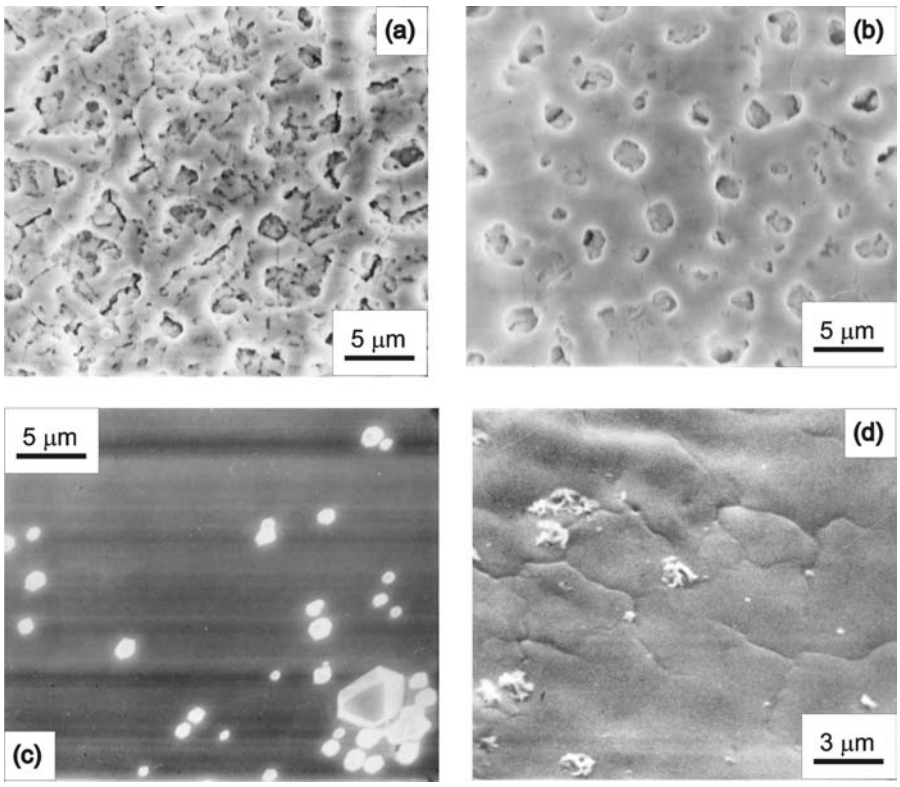

Fig. 2. Laser surface modifications/spots effected in different atmospheres during hfCVD-pulsed CO_2 laser synergy: a) spot created by the direct laser beam in CH_4 (1 %) in H_2; b) spot created by the direct laser beam in C_2H_4 (0.5 %) in H_2; c) spot created by the reflected laser beam in C_2H_4 (0.5 %) in H_2; d) spot created by the direct laser beam in C_2H_4 (7.5 %) in H_2.

Microscopic examination reaching even higher magnifications was undertaken in order to corroborate these findings. The morphology of the uncovered surface in the reflection spot is given by the AFM 3D-image (1.5 μm×1.5 μm) in Fig. 3a. Profile analysis of the examined surface segment, performed along the white, dashed line, is presented in Fig. 3b. The depth of the observed cracks (vertical distance between cursors) was ascertained in Fig. 3b, Graph (1), and equals

*Effect of the radiation reflection in the course of the hfCVD-pulsed CO_2 laser synergy was not observed in the spectro-unabsorbing precursor, CH_4 (1 %) in H_2, due to the formation of a thick diamond deposit; in the very high concentration of the spectro-absorbing diamond precursor atmosphere, C_2H_4 (7.5 %) in H_2, a reflection spot was not unambiguously discerned.

18 and 24 nm. The width of the observed cracks (horizontal distance between cursors), seen in Fig. 3b, Graph (2), amounts to 120 and 160 nm. The roughness of the examined surface segment is 7.5 nm (all numerical values are rounded). The presented evidence indicates that the pulsed laser radiation produced nanoscale surface damage in the reflection spot created in the micrometer-thick diamond coating. Consequently, applications which are unaffected by nanometric defects of the substrate surface are suitable for this method of coating patterning.

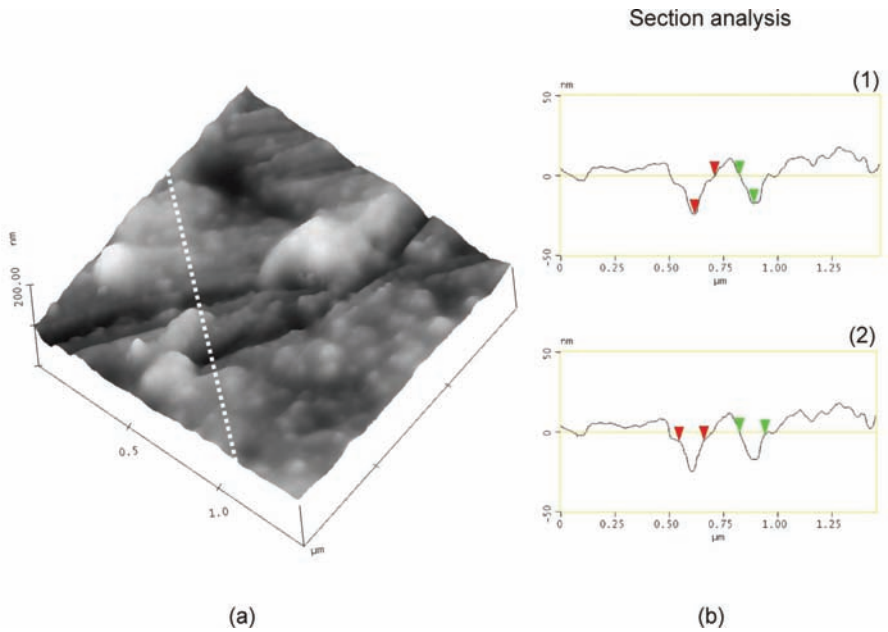

Fig. 3. Uncovered substrate surface in the reflection spot taken by AFM: a) 3D-surface view of the morphology (the white, dashed line indicates the location of the section analysis); b) profile of the section analysed, giving the depth (1) and width (2) of the registered flaws.

Hence, the main idea which induced these investigations, the prospective employment of reflected laser radiation for diamond coating patterning, gave several results: a proper evaluation of effects and concluding with possible applications.

CONCLUSIONS

– Irradiation of a mirror-polished substrate surface in a spectro-absorbing diamond precursor atmosphere during hot filament-pulsed CO_2 laser synergy enables obtaining a reflection spot, *i.e.*, a specific coating pattern, to be obtained.

– Laser radiation multiple pass/reflection through a spectro-absorbing precursor atmosphere moderates/eliminates the effects of thermal shock produced by the beam stroke on the surface.

– This procedure of coating patterning is recommended for applications insensitive to nanoscale surface flaws.

Acknowledgements. This work was financially supported by the Ministry of Science and Technological Development of the Republic of Serbia, under projects 142065 and 142067.

ИЗВОД

ЛАСЕРСКИ СПОТ РЕФЛЕКСИЈЕ КАО ШАРА У ДИЈАМАНТСКОЈ ПРЕВЛАЦИ – МИКРОСКОПСКО ПРОУЧАВАЊЕ

ГОРДАНА С. РИСТИЋ[1], МИЛАН С. ТРТИЦА[1], ЖАРКО Д. БОГДАНОВ[1], ЗЛАТКО Љ. РАКОЧЕВИЋ[1] и ШЋЕПАН С. МИЉАНИЋ[1,2]

[1]*Институт за нуклеарне науке ВИНЧА, п.пр. 522, 11001 Београд и* [2]*Факултет за физичку хемију, Универзитет у Београду, п.пр. 137, 11001 Београд*

Дијамантске превлаке депоноване су спрегнутим и синхроним деловањем методе усијаног влакна ХДП и импулсног CO_2 ласера у спектроапсорбујућој и спектронеапсорбујућој атмосфери дијамантског прекурсора. Добијене превлаке су структуриране/ишаране, тј. садрже непрекривене, огољене области. Додатни ефекат, запажен само у спектроактивној атмосфери дијамантског прекурсора, јесте формирање још једног ласерског спота у превлаци – рефлексионог спота. Опсежна микроскопска истраживања урађена су имајући у виду морфолошке промене у споту директног ласерског зрака, са циљем да се утврди практична употребљивост рефлексионог спота. СЕМ микрографије нормалне инциденције овог спота показују глатку површину без оштећења импулсним зрачењем. АФМ техника визуализације открила је право стање површине и дала је прецизне податке о њеним карактеристикама.

(Примљено 3. јула 2008, ревидирано 13. марта 2009)

REFERENCES

1. F. G. Celii, H. H. Nelson, P. E. Pehrsonn, *J. Mater. Res.* **5** (1990) 2337
2. Y. Goto, T. Yagi, H. Nagai, *Mat. Res. Soc. Proc.* **129** (1989) 213
3. H. Chen, N. Mafei, R. H. Prince, *J. Appl. Phys.* **76** (1994) 8113
4. M. Lindstam, M. Boman, J. O. Carlsson, *Appl. Surf. Sci.* **109**/**110** (1997) 462
5. Q. Wang, R. Schliesing, H. Zacharias, V. Buck, *Appl. Surf. Sci.* **138**/**139** (1999) 429
6. G. F. Zhang, V. Buck, *Appl. Surf. Sci.* **180** (2001) 255
7. Z. Toth, A. Mechler, P. Heszler, *Appl. Surf. Sci.* **168** (2000) 5
8. J. Gaze, T. Obata, N. Oyanagi, H. Izawa, W. L. Zhou, M. Kusunoki, Y. Ikuhara, *Nucl. Instr. Meth. Phys. Res. B* **121** (1997) 427
9. G. S. Ristić, M. S. Trtica, Ž. D. Bogdanov, N. Ž. Romčević, Š. S. Miljanić, *Appl. Surf. Sci.* **253** (2007) 5233
10. G. S. Ristić, Ž. D. Bogdanov, S. Zec, N. Romčević, Z. Dohčević-Mitrović, Š. S. Miljanić, *Mater. Chem. Phys.* **80** (2003) 529
11. M. S. Trtica, B. M. Gaković, B. B. Radak, Š. S. Miljanić, in *Proceedings of SPIE, Vol.* 4747: *International Conference on Atomic and Molecular Pulsed Lasers IV*, (2002), Tomsk, Russia, (2001), p. 44
12. I. Horcas, R. Fernandez, J. M. Gomez-Rodrigez, J. Colchero, J. Gomez-Herrero, A. M. Baro, *Rev. Sci. Instruments* **78** (2007) 013705
13. J. H. Weaver, in *CRC Handbook of Chemistry and Physics*, D. R. Lide, Ed., CRC Press, Boca Raton, 1991, p.p. 12–87.

Journal of the Serbian Chemical Society
JSCS@tmf.bg.ac.rs • www.shd.org.rs/JSCS

J. Serb. Chem. Soc. 74 (7) 781–787 (2009)
JSCS–3876

UDC 546.661:66.061+546.11'535+546.212+547.546
Short communication

SHORT COMMUNICATION

Distribution of micro-amounts of europium in the two-phase water–HCl–nitrobenzene–*N*,*N*'-dimethyl-*N*,*N*'-diphenyl-2,6-dipicolinamide–hydrogen dicarbollylcobaltate extraction system

EMANUEL MAKRLÍK[1]*, PETR VAŇURA[2], PAVEL SELUCKÝ[3], VASILY A. BABAIN[4] and IVAN V. SMIRNOV[4]

[1]*Faculty of Applied Sciences, University of West Bohemia, Husova 11, 306 14 Pilsen,* [2]*Institute of Chemical Technology, Technická 5, 166 28 Prague,* [3]*Nuclear Research Institute, 250 68 Řež, Czech Republic and* [4]*Khlopin Radium Institute, Research and Production Association, St. Petersburg, Russia*

(Received 31 July 2008, revised 4 February 2009)

Abstract: Extraction of micro-amounts of europium by a nitrobenzene solution of hydrogen dicarbollylcobaltate (H^+B^-) in the presence of *N*,*N*'-dimethyl-*N*,*N*'-diphenyl-2,6-dipicolinamide (MePhDPA, L) was investigated. The equilibrium data were explained assuming that the species HL^+, HL_2^+, EuL_2^{3+} and EuL_3^{3+} are extracted into the organic phase. The values of the extraction and stability constants of the species in nitrobenzene saturated with water were determined.

Keywords: europium; hydrogen dicarbollylcobaltate; *N*,*N*'-dimethyl-*N*,*N*'-diphenyl-2,6-dipicolinamide; water–nitrobenzene system; extraction and stability constants.

INTRODUCTION

The dicarbollylcobaltate anion and some of its halogen derivatives are very useful reagents for the extraction of alkali metal cations (especially Cs^+), and also, in the presence of polyoxyethylene compounds, for the extraction of Sr^{2+} and Ba^{2+} from aqueous solution into an organic polar phase, both under laboratory conditions for purely theoretical or analytical purposes,[1] and on the technological scale for the separation of some high-activity isotopes in the reprocessing of spent nuclear fuel and acidic radioactive waste.[2–4]

Dicarboxylic acid diamides are the subject of active research as potential extractants of actinides (in particular of minor actinides) from radioactive wastes. Important information concerning substituted malonic diamides was reported.[5,6]

* Corresponding author. E-mail: makrlik@centrum.cz
doi: 10.2298/JSC0907781M

Lately, interest has shifted to the properties of tetra-alkyl-diglycolamides,[7–10] with emphasis on tetra-octyl-diglycolamide (TODGA) as an extractant of Pu(IV), Np(IV), Am(III) and Cm(III) in solutions with hydrocarbon diluents.[7–9] The ability of TODGA to extract many other metals was discussed[10,11] and the very high extractive capacity of this agent was shown to allow its application as a solid extractant.[12]

Recently, the extraction properties of some 2,6-dipicolinamides were investtigated.[13–16] In the present work, the solvent extraction of micro-amounts of europium by a nitrobenzene solution of hydrogen dicarbollylcobaltate (H^+B^-)[1] in the presence of *N*,*N*'-dimethyl-*N*,*N*'-diphenyl-2,6-dipicolinamide (MePhDPA, L) (see Scheme 1) was studied. The intention was to find the composition of the species in the nitrobenzene phase and to determine the corresponding equilibrium constants.

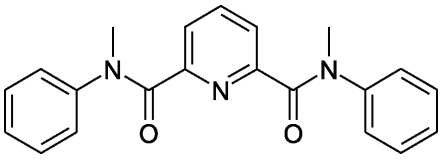

Scheme 1. Structural formula of *N*,*N*'-dimethyl--*N*,*N*'-diphenyl -2,6-dipicolinamide (MePhDPA).

EXPERIMENTAL

N,*N*'-dimethyl-*N*,*N*'-diphenyl-2,6-dipicolinamide (MePhDPA) was prepared as described in the literature.[17,18] Cesium dicarbollylcobaltate (Cs^+B^-) was synthesized by the method published by Hawthorne *et al.*[19] A nitrobenzene solution of hydrogen dicarbollylcobaltate (H^+B^-)[1] was prepared from Cs^+B^- by the procedure described elsewhere.[20] The other chemicals used (Lachema, Czech Republic) were of reagent grade purity. The radionuclide $^{152,154}Eu^{3+}$ (Polatom, Poland) was of standard radiochemical purity.

The extraction experiments in the two-phase water–HCl–Eu^{3+} (micro-amounts)–nitrobenzene–MePhDPA–H^+B^- systems were performed in 10 ml glass test-tubes closed with polyethylene stoppers, using 2 ml of each phase. The test-tubes filled with the solutions were shaken for 2 h at 25±1 °C using a laboratory shaker. Under these conditions, the equilibria in the system under study were established after approximately 20 min of shaking. Then the phases were separated by centrifugation. Afterwards, 1 ml samples were taken from each phase and their γ-activities were measured using a well-type NaI(Tl) scintillation detector connected to a γ-analyzer, NK/350 (Gamma, Hungary).

The equilibrium distribution ratios, *D*, of europium were determined as the ratios of the corresponding radioactivities of $^{152,154}Eu^{3+}$ measured in the nitrobenzene and aqueous samples.

RESULTS AND DISCUSSION

The dependence of the logarithm of the europium distribution ratios (log *D*) on the logarithm of the numerical value of the total (analytical) concentration of the MePhDPA ligand in the initial nitrobenzene phase, log *c*(L), is shown in Fig. 1. The initial concentration of hydrogen dicarbollylcobaltate in the nitrobenzene phase, *c*(B) = 0.010 mol/l, as well as the initial concentration of HCl in the aqueous phase, *c*(HCl) = 0.20 mol/l, are always related to the volume of one phase.

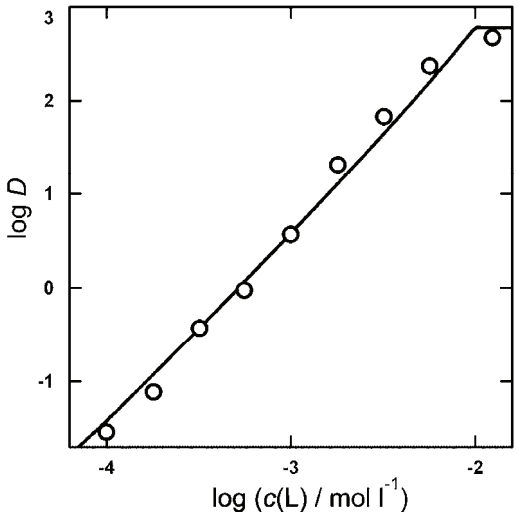

Fig. 1. Log D as a function of log c(L), where L = MePhDPA, for the system water–HCl–Eu^{3+} (micro-amounts)–nitrobenzene–MePhDPA–H^+B^-. c(HCl) = 0.20 mol/l, c(B) = 0.010 mol/l. The curve was calculated using the constants given in Table I.

Regarding previous results,[21–26] the considered water–HCl–Eu^{3+} (micro-amounts)–nitrobenzene–MePhDPA(L)–H^+B^- system can be described by the set of reactions:

$$L(aq) \rightleftharpoons L(org);\ K_D \quad (1)$$

$$H^+(org) + L(org) \rightleftharpoons HL^+(org);\ \beta(HL^+(org)) \quad (2)$$

$$H^+(org) + 2L(org) \rightleftharpoons HL_2^+(org);\ \beta(HL_2^+(org)) \quad (3)$$

$$Eu^{3+}(aq) + 3H^+(org) \rightleftharpoons Eu^{3+}(org) + 3H^+(aq);\ K_{ex}(Eu^{3+}(aq)) \quad (4)$$

$$Eu^{3+}(aq) + nL(org) + 3H^+(org) \rightleftharpoons EuL_n^{3+}(org) + 3H^+(aq);\ K_{ex}(EuL_n^{3+}(org)) \quad (5)$$

to which the equilibrium constants: K_D, $\beta(HL^+(org))$, $\beta(HL_2^+(org))$, $K_{ex}(Eu^{3+}(aq))$ and $K_{ex}(EuL_n^+(org))$ correspond.

TABLE I. Equilibrium constants in the water–HCl–Eu^{3+} (micro-amounts)–nitrobenzene–MePhDPA–H^+B^- system

Equilibrium	log K
(1)	1.29[a]
(2)	9.30[b]
(3)	10.7[b]
(4)	1.30[c]
(5), n = 2	25.0
(5), n = 3	34.6
$Eu^{3+}(org) + 2L(org) \rightleftharpoons EuL_2^{3+}(org)$	23.8
$Eu^{3+}(org) + 3L(org) \rightleftharpoons EuL_3^{3+}(org)$	33.3

[a]Determined by the concentration dependent distribution method described in ref. 21; [b]determined by the method described in details in ref. 22; [c]ref. 23

A subroutine UBBE, based on the relations given above, the mass balance of the MePhDPA ligand and the electroneutrality conditions in both phases of the system under consideration, was formulated[27,28] and introduced into a more general least-squares minimizing program LETAGROP[29] used for the determination of the "best" values of the extraction constants $K_{ex}(EuL_n^{3+}(org))$. The minimum of the sum of the errors in log *D*, *i.e.*, the minimum of the expression:

$$U = \Sigma(\log D_{calc} - \log D_{exp})^2 \quad (6)$$

was sought.

The values log K_D = 1.29 (see Table I, footnote a), log ($\beta(HL^+(org))$) = 9.3 (see Table I, footnote b), log ($\beta(HL_2^+(org))$) = 10.7 (see Table I, footnote b) and log ($K_{ex}(Eu^{3+}(aq))$) = 1.3[23] were used for the respective calculations. The results are listed in Table II, from which it is evident that the extraction data can be best explained assuming the complexes EuL_2^{3+} and EuL_3^{3+} are extracted into the nitrobenzene phase.

TABLE II. Comparison of three different models of europium extraction from an aqueous HCl solution by a nitrobenzene solution of H^+B^- in the presence of MePhDPA

Europium complexes in the organic phase	log K_{ex}[a]	U[b]
EuL_2^{3+}	25.60 (26.16)	10.40
EuL_3^{3+}	35.35 (35.73)	2.41
EuL_2^{3+} , EuL_3^{3+}	25.05 (25.32), 34.58 (34.99)	0.05

[a]The values of the extraction constants are given for each complex. The reliability interval of the constants is given as $3\sigma(K)$, where $\sigma(K)$ is the standard deviation of the constant *K*.[29] These values are given in the logarithmic scale using the approximate expression $\log K \pm \{\log(K + 1.5\sigma(K)) - \log(K1.5\sigma(K))\}$. For $\sigma(K) > 0.2\ K$, the previous expression is not valid and then only the upper limit is given in the parentheses in the form of $\log K(\log[K + 3\sigma(K)])$;[29] [b]the error-square sum $U = \Sigma(\log D_{calc} - \log D_{exp})^2$

Knowing the value $\log K_{ex}(Eu^{3+}(org)) = 1.30$,[23] as well as the extraction constants $\log K_{ex}(EuL_2^{3+}(org)) = 25.0$ and $\log K_{ex}(EuL_3^{3+}(org)) = 34.6$ determined here (Table II), the stability constants of the complexes EuL_2^{3+} and EuL_3^{3+} in the nitrobenzene phase defined as:

$$\beta(EuL_2^{3+}(org)) = \frac{[EuL_2^{3+}(org)]}{[Eu^{3+}(org)][L(org)]^2} \quad (7)$$

$$\beta(EuL_3^{3+}(org)) = \frac{[EuL_3^{3+}(org)]}{[Eu^{3+}(org)][L(org)]^3} \quad (8)$$

can be evaluated applying the simple relations:

$$\log \beta(EuL_2^{3+}(org)) = \log K_{ex}(EuL_2^{3+}(org)) - \log K_{ex}(Eu^{3+}(org)) \quad (9)$$

$$\log \beta(EuL_3^{3+}(org)) = \log K_{ex}(EuL_3^{3+}(org)) - \log K_{ex}(Eu^{3+}(org)) \quad (10)$$

The respective equilibrium constants are summarized in Table I.

Furthermore, Fig. 2 depicts the contributions of the species Eu^{3+}(org), EuL_2^{3+}(org) and EuL_3^{3+}(org) to the total europium concentration in the equilibrium organic phase. It follows from Fig. 2 that the complex EuL_3^{3+}(org) is present in significant concentrations in the equilibrium nitrobenzene phase only at relatively high amounts of the MePhDPA ligand in the system under consideration.

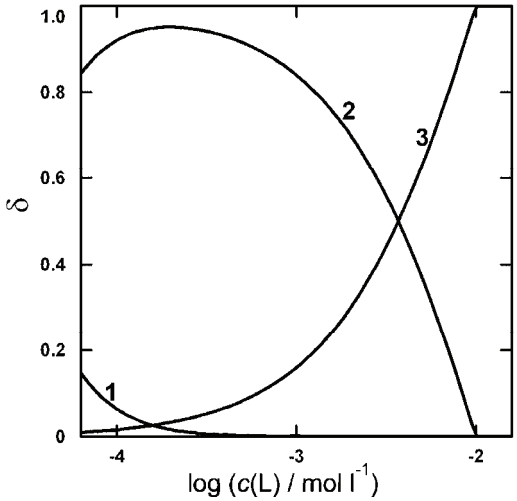

Fig. 2. Distribution diagram of europium in the equilibrium nitrobenzene phase of the water–HCl–Eu^{3+} (micro-amounts)–nitrobenzene–MePhDPA–H^+B^- extraction system in the forms of Eu^{3+}, EuL_2^{3+} and EuL_3^{3+}. c(HCl) = 0.20 mol/l; c(B) = 0.010 mol/l. 1: $\delta(Eu^{3+}) = [Eu^{3+}(org)]/c(Eu^{3+}(org))$; 2: $\delta(EuL_2^{3+}) = [EuL_2^{3+}(org)]/c(Eu^{3+}(org))$; 3: $\delta(EuL_3^{3+}) = [EuL_3^{3+}(org)]/c(Eu^{3+}(org))$, where: $c(Eu^{3+}(org)) = [Eu^{3+}(org)] + [EuL_2^{3+}(org)] + [EuL_3^{3+}(org)]$. The distribution curves were calculated using the constants given in Table I.

Finally, the stability constants of the EuL_2^{3+} and EuL_3^{3+} complexes in water saturated nitrobenzene at 25 °C for L = *N*,*N*'-dimethyl-*N*,*N*'-diphenyl-2,6-dipicolinamide, (MePhDPA), *N*,*N*'-dimethyl-*N*,*N*'-diphenyl-2,6-dipicolinamide (EtPhDPA) are given in Table III. It is interesting that the stability constants of the EuL_2^{3+} complexes in the mentioned medium are comparable for both these ligands, whereas the stability of the species EuL_3^{3+} is somewhat higher for L = = MePhDPA than when L = EtPhDPA, as follows from Table III.

TABLE III. Stability constants of the complexes EuL_2^{3+} and EuL_3^{3+} for L = *N*,*N*'-dimethyl-*N*,*N*'-diphenyl-2,6-dipicolinamide (MePhDPA), *N*,*N*'-diethyl-*N*,*N*'-diphenyl-2,6-dipicolinamide (EtPhDPA) in water saturated nitrobenzene at 25 °C

L	$\log \beta(EuL_2^{3+}(org))$	$\log \beta(EuL_3^{3+}(org))$
MePhDPA	23.75	33.28
EtPhDPA[a]	23.54	32.36

[a]Ref. 30

In conclusion, it is necessary to emphasize that the stability constants of the complexes EuL_2^{3+} and EuL_3^{3+}, where L is *N*,*N*'-dibutyl-*N*,*N*'-dimethyl-2-(2-dodecyloxyethyl)malonamide (DBDMDDOEMA) in nitrobenzene saturated with water are $\log \beta(EuL_2^{3+}(org)) = 7.17$ and $\log \beta(EuL_3^{3+}(org)) = 9.18$.[31] From this

fact, it follows that the DBDMDDOEMA ligand is a less effective extraction agent for Eu^{3+} than the ligand MePhDPA in the two-phase water–nitrobenzene system.

Acknowledgements. The presented work was supported by the Czech Ministry of Education, Youth and Sports, Projects MSM 4977751303 and MSM 6076137307.

ИЗВОД

РАСПОДЕЛА МИКРОКОЛИЧИНА ЕУРОПИЈУМА У ДВОФАЗНОМ ЕКСТРАКЦИОНОМ СИСТЕМУ ВОДА–HCl–НИТРОБЕНЗЕН–*N,N'*-ДИМЕТИЛ-*N,N'*-ДИФЕНИЛ-2,6--ДИПИКОЛИНАМИД-ВОДОНИК-ДИКАРБОЛИЛКОБАЛТАТ

E. MAKRLÍK[1], P. VAŇURA[2], P. SELUCKÝ[3], V. A. BABAIN[4] и I. V. SMIRNOV[4]

[1]*Faculty of Applied Sciences, University of West Bohemia, Husova 11, 306 14 Pilsen,* [2]*Institute of Chemical Technology, Technická 5, 166 28 Prague,* [3]*Nuclear Research Institute, 250 68 Řež, Czech Republic and* [4]*Khlopin Radium Institute, Research and Production Association, St. Petersburg, Russia*

Испитивана је екстракција микроколичина еуропијума водоник-карболилкобалтатом (H^+B^-) растворeним у нитробензену, у присуству *N,N'*-диметил-*N,N'*-дифенил-2,6-дипиколинамида (MePhDPA, L). Подаци за стање равнотеже објашњени су уз претпоставку да су јони HL^+, HL_2^+, EuL_2^{3+} и EuL_3^{3+} екстраховани органском фазом. Одређене су вредности константи екстракције и стабилности јона у водом засићеном нитробензену.

(Примљено 31. јула 2008, ревидирано 4. фебруара 2009)

REFERENCES

1. E. Makrlík, P. Vaňura, *Talanta* **32** (1985) 423
2. J. D. Law, K. N. Brewer, R. S. Herbst, T. A. Todd, D. J. Wood, *Waste Management* **19** (1999) 27
3. V. N. Romanovskiy, I. V. Smirnov, V. A. Babain, T. A. Todd, R. S. Herbst, J. D. Law, K. N. Brewer, *Solvent Extr. Ion Exch.* **19** (2001) 1
4. J. D. Law, R. S. Herbst, T. A. Todd, V. N. Romanovskiy, V. A. Babain, V. M. Esimantovskiy, I. V. Smirnov, B. N. Zaitsev, *Solvent Extr. Ion Exch.* **19** (2001) 23
5. C. Cuillerdier, C. Musikas, P. Hoel, L. Nigond, X. Vitart, *Sep. Sci. Technol.* **26** (1991) 1229
6. V. K. Manchanda, P. N. Pathak, *Sep. Purif. Technol.* **35** (2004) 85
7. Y. Sasaki, G. R. Choppin, *Anal. Sci*. **12** (1996) 225
8. Y. Sasaki, Y. Sugo, S. Suzuki, S. Tachimori, *Solvent Extr. Ion Exch*. **19** (2001) 91
9. Y. Sasaki, S. Tachimori, *Solvent Extr. Ion Exch*. **20** (2002) 21
10. Y. Sasaki, Y. Sugo, S. Suzuki, T. Kimura, *Anal. Chim. Acta* **543** (2005) 31
11. S. A. Ansari, P. N. Pathak, V. K. Manchanda, M. Husain, A. K. Prasad, V. S. Parmar, *Solvent Extr. Ion Exch.* **23** (2005) 463
12. E. P. Horwitz, D. R. McAlister, A. H. Bond, R. E. Barrans, Jr., *Solvent Extr. Ion Exch.* **23** (2005) 319
13. M. Yu. Alyapyshev, V. A. Babain, I. V. Smirnov, *Radiochemistry (Radiokhimiya), Eng. Ed.* **46** (2004) 270
14. M. Yu. Alyapyshev, V. A. Babain, I. V. Smirnov, A. Yu. Shadrin, *Radiochemistry (Radiokhimiya), Eng. Ed.* **48** (2006) 369

15. V. N. Romanovskiy, V. A. Babain, M. Yu. Alyapyshev, I. V. Smirnov, R. S. Herbst, J. D. Law, T. A. Tood, *Sep. Sci. Technol.* **41** (2006) 2111
16. V. A. Babain, M. Yu. Alyapyshev, R. N. Kiseleva, *Radiochim. Acta* **95** (2007) 217
17. A. Shimada, T. Yaita, H. Narita, S. Tachimori, K. Okuno, *Solvent Extr. Ion Exch.* **22** (2004) 147
18. E. S. Nikitskaya, V. S. Usovskaya, M. V. Rubtstov, *Zh. Obsch. Khimii* **28** (1958) 161
19. M. F. Hawthorne, D. C. Young, T. D. Andrews, D. V. Howe, R. L. Pilling, A. D. Pitts, M. Reintjes, L. F. Warren, P. A. Wegner, *J. Am. Chem. Soc.* **90** (1968) 879
20. E. Makrlík, *Collect. Czech. Chem. Commun*. **57** (1992) 289
21. P. Vaňura, E. Makrlík, *J. Radioanal. Nucl. Chem.* **267** (2006) 251
22. P. Vaňura, E. Makrlík, *J. Radioanal. Nucl. Chem.* **267** (2006) 465
23. E. Makrlík, P. Vaňura, *Collect. Czech. Chem. Commun*. **51** (1986) 498
24. J. Rais, E. Šebestová, P. Selucký, M. Kyrš, *J. Inorg. Nucl. Chem.* **38** (1976) 1742
25. P. Vaňura, *Solvent Extr. Ion Exch.* **10** (1994) 145
26. J. Rais, S. Tachimori, *Sep. Sci. Technol.* **29** (1994) 1347
27. P. Vaňura, E. Makrlík, J. Rais, M. Kyrš, *Collect. Czech. Chem. Commun*. **47** (1982) 1444
28. P. Vaňura, E. Makrlík, *Collect. Czech. Chem. Commun.* **58** (1993) 1324
29. L. G. Sillén, B. Warnqvist, *Arkiv Kemi*. **31** (1969) 315
30. E. Makrlík, P. Vaňura, P. Selucký, V. A. Babain, I. V. Smirnov, *Radiochemistry*, in press
31. 31. E. Makrlík, P. Vaňura, P. Selucký, *J. Radioanal. Nucl. Chem.* **279** (2009) 287.

Journal of the Serbian Chemical Society
JSCS@tmf.bg.ac.rs • www.shd.org.rs/JSCS

J. Serb. Chem. Soc. 74 (7) 789–799 (2009)
JSCS–3877

UDC 543.552:546.48:546.74
Original scientific paper

Net analyte signal standard addition method for the simultaneous determination of cadmium and nickel

KARIM ASADPOUR-ZEYNALI*, MIR REZA MAJIDI and MASOUD TAHMASEBPOUR

Department of Analytical Chemistry, Faculty of Chemistry, University of Tabriz, Tabriz 51666 16471, Iran

(Received 18 December 2008, revised 10 April 2009)

Abstract: A novel net analyte signal standard addition method (NASSAM) is presented for the simultaneous determination of Cd^{2+} and Ni^{2+} in their mixture by differential pulse polarography. The method combines the advantages of the standard addition method with the net analyte signal concept, which enables the extraction of information concerning a certain analyte from voltammograms of multi-component mixtures. This method has some advantages, such as: the use of a full voltammogram, realization in a single step, therefore it does not require calibration and prediction steps and only a few measurements are required for the determination. The simultaneous determination of Cd^{2+} and Ni^{2+} was performed in Britton–Robinson buffer (pH 2.87) and 0.40 M potassium thiocyanate solution.

Keywords: differential pulse polarography; simultaneous determination; net analyte signal; standard addition method.

INTRODUCTION

Electrochemical techniques such as differential pulse polarography (DPP) and stripping voltammetry are highly sensitive techniques and are widely used in many area of analytical chemistry. However, their applicability to the determination of mixtures of several components is rather limited when they display strongly or partially overlapping polarograms. In this case, one may try to optimize the conditions for maximum separation in order to find a single variable. This, however, is time and cost consuming, and may be the source of errors. Chemometric techniques allow these problems to be overcome and the probability of finding a global optimum is increased.

The use of chemometrics in electrochemistry and the analysis of voltammetric data was reviewed recently.[1–3] Chemometrics can be applied to different steps of an electro-analytical process or with different objectives. Among the dif-

* Corresponding author. E-mail: asadpour@tabrizu.ac.ir
doi: 10.2298/JSC0907789A

ferent steps, the following can be mentioned: *i*) experimental design and optimization of relevant experimental and instrumental parameters, *ii*) preparation and transformation of data for further data treatment, *iii*) data exploration and sample classification and *iv*) concentration determination, calibration, and model identification.[2]

Several linear and non-linear multivariate calibration methods have been reported for simultaneous determination by electro-analytical techniques.[4–8] Also, the H-point standard addition method (HPSAM) was established for resolving strongly overlapping spectra of two analytes.[9,10] This method is based on dual wavelength spectrophotometry and the standard addition method. Shams *et al*.[11] used this method for the simultaneous determination of lead and tin by the striping voltammetry method. The HPSAM uses only two data points when the portion of the analytical signal due to the interferent is constant and that due to the analyte is as different as possible.

In this work, a novel standard addition method based on the net analyte signal concept, which does not have the constraints of the HPSAM, is introduced. The net analyte signal was defined by Lorber, based on spectroscopic methods, as the part of the spectrum of a mixture that is unique for the analyte of interest (Fig. 1), *i.e.*, it is orthogonal to the spectra of the interferences.[12] There are some net analyte signal based methods reported for calculation of the NAS.[13–16] In this work, an attempt was made to calculate NAS vectors and attribute them to the analyte concentration using the polarographic technique.

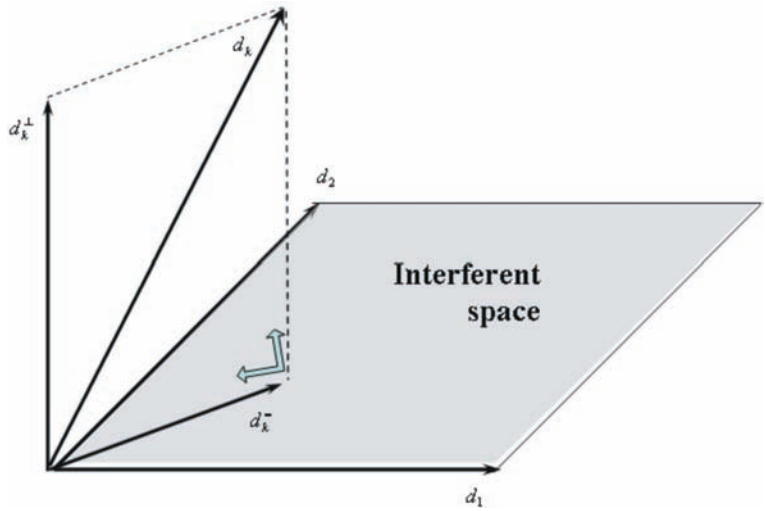

Fig. 1. Representation in J^{th} dimensional vector space analyte ($\mathbf{d}_k$) and vector of interfering agents ($\mathbf{d}_1$ and $\mathbf{d}_2$) and the NAS vector $\mathbf{d}_k^{\perp}$ will be different from $\mathbf{d}_k$ in direction and length. The vector $\mathbf{d}_k^{=}$ is the part of $\mathbf{d}_k$ that is in the interference space.

Theory

The conventional notation has been used throughout the following discussion. Thus, a boldface capital letter is used for a matrix, a boldface lower case for a column vector and a lightface lower case italic for a scalar. The superscript T designates the operation of the vector or matrix transposition and the superscript $^+$ denotes the pseudo-inverse of a non-square matrix. The digitized polarogram is referred to as a polarogram vector or simply as a vector, while a voltammogram vector of a pure component is called a component vector.

In principal component regression, the concentration prediction of the kth component in an unknown sample can be performed by the following equation:

$$c_{\text{un}} = d_{\text{un}}^{\text{T}}\mathbf{D}^{+}c \tag{1}$$

where d_{un} is the vector of the responses of the unknown sample, the matrix $\mathbf{D}^+$ is the pseudo inverse of the calibration matrix $\mathbf{D}$ ($J\times I$), and is the vector of concentrations of the kth component in the calibration set.

In voltammetric techniques, the currents measured at J potentials are collected in a ($J\times 1$) column vector (d). The matrix $\mathbf{D}$ ($J\times I$) contains the voltammogram of I samples in its columns. Suppose that the analyte of interest (k) is a compound in a mixture of other electro-active compounds that are called interfering agents. By definition, it is always possible to split up the voltammogram (d_k) of the analyte of interest into two distinct parts:

$$d_k = d_{\bar{\bar{k}}} + d_k^{\perp} \tag{2}$$

where $d_{\bar{\bar{k}}}$ is the part of the voltammogram that could have been generated by a linear combination of the voltammograms of the interfering agents. The superscript "=" indicates that $d_{\bar{\bar{k}}}$ is in the space spanned by the voltammograms of the interfering agent (Fig. 1). Consequently, $d_{\bar{\bar{k}}}$ cannot be unique for the analyte of interest because a mixture of interfering agents could have produced it. The other part, $d_k^{\perp}$, is orthogonal to the voltammograms of the interferences reflecting the part of the voltammogram only depending on the analyte k present in the mixture. This part, called the net analyte signal vector ($\mathbf{d}_{\text{NAS}}$), can therefore be used for quantification of the analyte k.[12,17,18] The shape of $d_k^{\perp}$ only depends on the presence of the interferences in the mixture, not on their specific concentrations. Only addition or deletion of electro-active components can change $d_k^{\perp}$. In the following, it as assumed that the spectra and\or voltammograms of samples without the analyte are available and during the determination they do not change. The net analyte signal of the kth component, $\mathbf{d}_{\text{NAS}}$, can be found by the following orthogonal projection:

$$\mathbf{d}_{\text{NAS}} = (\mathbf{I} - \mathbf{R}^{+}\mathbf{R})\mathbf{d}_{\text{k}} \tag{3}$$

where $\mathbf{d}_k$ is the component vector of the kth component with unity concentration and **R** is a matrix containing sensitivities to all components except to the kth component.

The NAS of the kth component may be used for concentration prediction of unknown samples using the previously derived equation:

$$c_{un} = \mathbf{d}^T_{un}\, \mathbf{d}_{NAS} / (\mathbf{d}^T_{NAS}.\mathbf{d}_{NAS}) \quad (4)$$

By comparing Eqs. (1) and (4), the relation between the regression vector and the net analyte signal of the component of interest can easily be seen:

$$\mathbf{b}_k = \mathbf{d}_{NAS} / (\mathbf{d}^T_{NAS}\, \mathbf{d}_{NAS}) \quad (5)$$

Clearly, the regression vector $\mathbf{b}_k$ is a part of the component vector (pure spectrum or voltammogram of the kth component with unity concentration), which is orthogonal to the subspace spanned by the pure spectra of all other components, multiplied by a scaling coefficient $(\mathbf{d}^T_{NAS}\, \mathbf{d}_{NAS})^{-1}$.

In binary and/or ternary mixtures when the interferences are known, the $\mathbf{d}_{NAS}$ can be calculated for analyte. The norm of this vector is proportional to the concentration of analyte, therefore this parameter was calculated before and after the addition of standard solutions of analyte and by using standard addition equations, the concentration of the analyte can be obtained. In other words, the norm of the NAS vector ($\mathbf{d}_{NAS}$) can be used to construct a univariate calibration model, where this parameter is plotted against the analyte concentration and a linear relationship is observed.

In this study, the standard addition method was used in order to eliminate calibration and prediction steps and the determination was realized in a single step. In addition, the other advantage of this method as compared with multivariate calibrations, such as principal component regression (PCR) and partial least squares (PLS), is the elimination of the necessity of choosing an optimum factor number during calibration.

Modeling

To demonstrate the analytical applicability of the proposed method for the analysis of binary mixtures, two voltammograms were created. The curves are two polarograms covering the potential rang –200 to –700 mV *versus* the SCE reference electrode (Fig. 2A) and five percent random noise was added to the data. The polarograms after addition of standards from component X are shown in Fig. 2B. Also, the NAS curve for component X and Y are demonstrated in Fig. 2C and Fig. 2D, respectively. The norm NAS for component X versus the standard concentration is shown in Fig. 2E, from which the concentration of the unknown sample can be calculated from the intercept. In this case, the concentration of the unknown sample was 0.50 μM and the calculated amount was 0.52 μM.

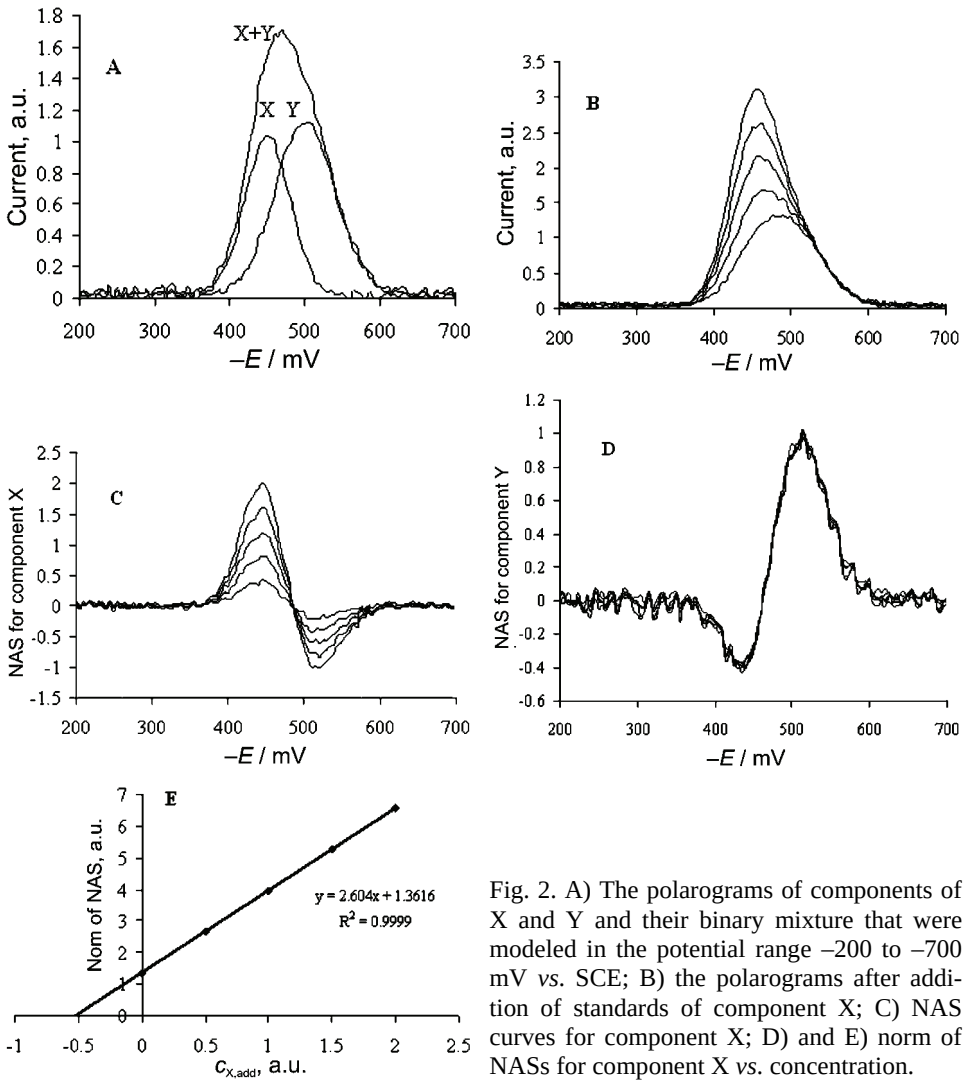

Fig. 2. A) The polarograms of components of X and Y and their binary mixture that were modeled in the potential range –200 to –700 mV *vs.* SCE; B) the polarograms after addition of standards of component X; C) NAS curves for component X; D) and E) norm of NASs for component X *vs.* concentration.

EXPERIMENTAL

Apparatus and software

The polarograms were obtained with a Metrohm 747 VA processor. A Metrohm 694 VA stand was used in the dropping mercury electrode (DME) mode. The three electrodes system was completed by means of a platinum wire as the counter electrode and a saturated calomel electrode (SCE) served as the reference electrode (both obtained from Azar Electrode Co., Urmia, Iran). All potentials in the text refer to the SCE. The pH measurements were performed by means of a Metrohm pH-Meter 691. Data of polarograms were firstly converted to an EXCEL file, in the next step they were converted to MATLAB format. All calculations were realized in MATLAB medium.[19]

Reagents

All reagents were of analytical/reagent grade and were used without further purification. A stock solution of Ni^{2+} (1.0×10^{-2} M) was prepared by dissolving 0.2910 g of the nitrate salt of Ni^{2+} in water and diluting to the mark in a 100 ml volumetric flask. A stock solution of Cd^{2+} (1.0×10^{-2} M) was prepared by dissolving 0.3080 g of the nitrate salt of Cd^{2+} in water and diluting to the mark in a 100 ml volumetric flask. Britton–Robinson buffer (pH 2.87) solution was prepared from phosphoric acid, acetic acid, boric acid and sodium hydroxide. Potassium thiocyanate solution (1.0 M) was prepared by dissolving 9.7200 g of crystals in water and diluting to the mark in a 100 ml volumetric flask. Doubly distilled water was used throughout. All experiments were performed at room temperature (≈ 25 °C).

Procedure

The analysis was performed by pipetting a suitable amount of a mixture of cadmium and nickel, together with 2.0 ml of Britton–Robinson buffer (pH 2.87) and 4.0 ml of potassium thiocyanate solution (1.0 M). Standard addition 1, 2, 3 and 4 ml of Cd^{2+} and Ni^{2+}(1.0×10^{-4} M) were individually carried out to the above solution (Figs. 3 and 4). The initial solution was purged with nitrogen gas for 330 s. The optimum values for the pulse amplitude potential, the drop time interval and the scan rate were –50 mV, 2 s and 2.0 mV s^{-1}, respectively. A computer sampled 150 data points in the range of –500 to –800 mV.

RESULTS AND DISCUSSION

Influence of effective variables

The effect of potassium thiocyanate concentration on the peak potential and peak current was investigated. The peak currents of both Ni^{2+} and Cd^{2+} reached their maximum with a potassium thiocyanate concentration of 0.40 M, but the potassium thiocyanate concentration in range 0.010 to 1.2 M had no significant effect on the peak potentials of Ni^{2+} and Cd^{2+}. Additionally, it was found that the best peak separation can be obtained with a potassium thiocyanate concentration of 0.40 M.

The effect of pH on the peak currents of Ni^{2+} and Cd^{2+} was investigated, whereby the maximum peak currents for both ions were obtained in pH 2.87, while the peak potentials did not change with increasing pH. Thus, a potassium thiocyanate concentration of 0.40 M and pH 2.87 were selected as a suitable medium.

Under the optimum conditions, the peak currents of the differential pulse polarograms linearly depended on the Cd^{2+} and Ni^{2+} concentrations. The differenttial pulse polarograms at different concentrations of Cd^{2+} and Ni^{2+} are shown in Figs. 3 and 4, respectively.

Plots of the peak current values as a function of the concentration were drawn. The plots were linear in the concentration range of 2.06×10^{-6} to 9.26×10^{-4} and 2.83×10^{-6} to 1.15×10^{-3} mol dm^{-3} for Cd^{2+} and Ni^{2+}, respectively. Also, the norm of individual polarograms were plotted *versus* concentration and linearity was obtained (see Figs. 3 and 4, Insets B). The lack of bilinearity and additivity

of data are some of difficulties encountered in the application of multivariate calibra-

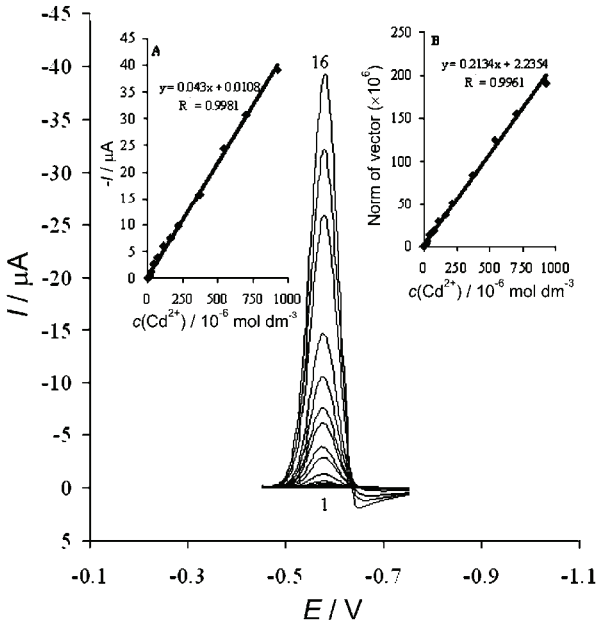

Fig. 3. DPPs for increasing concentrations of Cd^{2+} from 1) 2.60×10^{-6} to 16) 9.26×10^{-4} M in Britton–Robinson buffer (pH 2.87) and potassium thiocyanate (0.40 M) solution. Scan rate:2 mV/s and modulation amplitude –50 mV. Insets: A) variation of the peak current *vs*. concentration of Cd^{2+}; B) variation of the norm NAS for Cd^{2+} *vs*. concentration of Cd^{2+}.

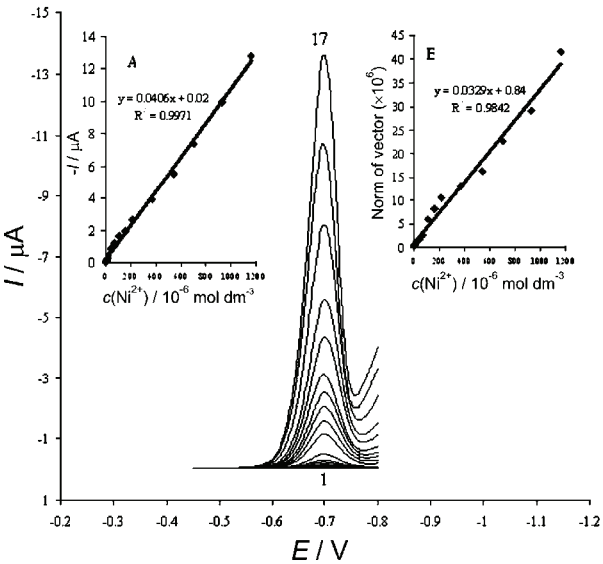

Fig. 4. DPPs for increasing concentrations of Ni^{2+} from 1) 2.83×10^{-6} to 17) 1.16×10^{-3} M in Britton–Robinson buffer (pH 2.87) and potassium thiocyanate (0.40 M) solution. Scan rate: 2 mV/s and modulation amplitude –50 mV. Insets: A) variation of the peak current *vs*. concentration of Cd^{2+}; B) variation of norm NAS for Ni^{2+} *vs*. concentration of Ni^{2+}.

tion methods in voltammetric data analysis. Therefore, the linearity and additivity of the voltammetric responses was checked. In the absence of an intermetallic

effect, the measured current of the binary sample at each potential will be equal to sum of the individual samples. Therefore, to check the additivity of the currents, a polarogram of a mixture (Fig. 5) was compared with the sum of the voltammetric signals of Cd^{2+} and Ni^{2+}. It can be seen from Fig. 5 that is no difference in the two curves. This means that there is no analyte–analyte interaction and/or intermetallic effect during the reduction. Therefore, the position of the peaks and/or shape of the polarograms do not change with these effects.

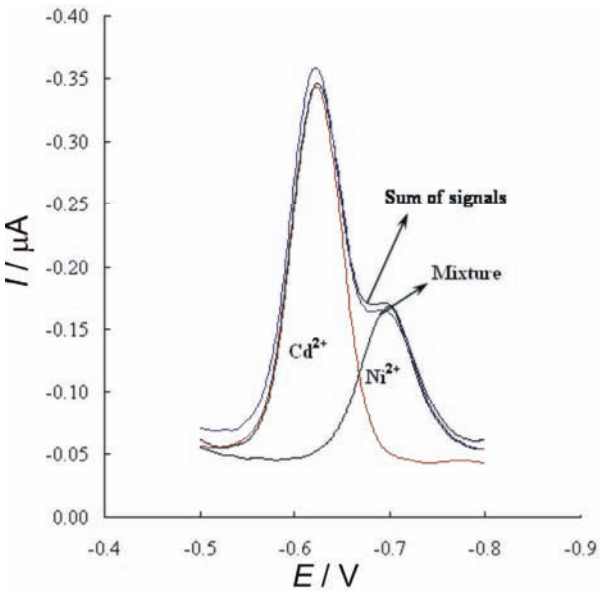

Fig. 5. DPP Ni^{2+} (10 μM) and Cd^{2+} (10 μM) and their mixture under theoretical (sum of the individual signals) and experimental (mixture) condition. Other conditions are as in Figs. 3 and 4.

NASSAM for determination of Ni^{2+} and Cd^{2+} in synthetic samples

The differential pulse polarograms of 10 μM Ni^{2+} and Cd^{2+} in Britton–Robinson buffer (pH 2.87) and potassium thiocyanate solution (0.40 M) in the range of −500 to −800 mV are shown in Fig. 6A, curve a, and after addition of known amounts of Ni^{2+} solutions in Fig. 6A, curves b to e. In this step, Ni^{2+} was considered as the analyte and Cd^{2+} as the interference. The part of the mixture polarograms that is orthogonal to the space of Cd^{2+} (*i.e.*, the NASs for Ni^{2+}) was calculated (see Eq. (3)) and their norms *versus* concentration are shown in the inset of Fig. 6A. The norm of the NAS vectors was attributed to the analyte concentration and only this changes with changes in the analyte concentration. Fig. 6B shows the same plots for the standard addition of Ni^{2+}. From these plots (Insets of Fig. 6A and B) and based on the equations of the univariate standard addition method, the concentrations of Ni^{2+} and Cd^{2+} in the solutions can be calculated.

Under optimum conditions, NASSAM was used for the determination of Cd^{2+} and Ni^{2+} in synthetic samples (the concentrations of the analytes were 10

μM). For three replicated experiments, the mean concentrations of Cd^{2+} and Ni^{2+} were found to be 10.4 and 10.3 μM, respectively.

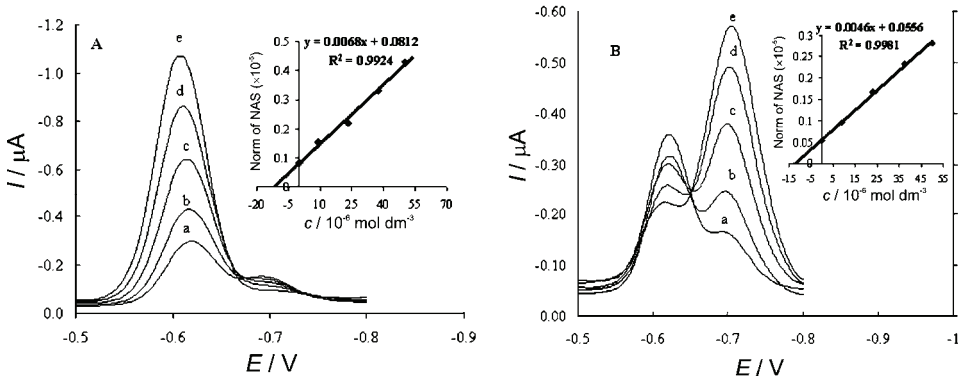

Fig. 6. A) DPP of unknown solution (curve a) and after addition of standard solutions (curves b–e) for the determination of Cd^{2+}. Inset: plot of norm NAS for Cd^{2+} *vs.* added standard concentration; B) same curves for Ni^{2+}. Conditions were as in Fig. 3 and 4.

Recovery of added metals

To determine the recovery of Cd^{2+} and Ni^{2+}, appropriate volumes of the standard solutions were added to the investigated samples. The results showed mean percentage recoveries of 103.4 and 104.0 % for Cd^{2+} and Ni^{2+}, respecttively.

Interferences

By the present method, the concentration of species can be determined in the presence of recognized interferences. Under the experimental conditions, the polarogram of vanadate overlaps with those of nickel and cadmium. Therefore, nickel and cadmium were assayed in the presence of vanadate as an interfering agent (concentrations of the analytes and interferent were 10 μM). In the determination of nickel, the interferent space was constructed with cadmium and vanadate and for the determination of cadmium this space was constructed with nickel and vanadate. The obtained results showed that the presence of vanadate as an interfering agent had negligible effect on the accuracy of the simultaneous determination of nickel and cadmium and their recoveries were 96.8 and 106.4 %, respectively.

CONCLUSIONS

Quantification of Cd^{2+} and Ni^{2+} was accomplished from differential pulse polarography data by a novel method based on the net analyte signal and standard addition method. When the interferents are known, the part of the overlapping voltammograms orthogonal to the interferents space can be calculated as the

net analyte signal and this is attributed to the analyte concentration. Two popular multivariate calibration methods, *i.e.*, PCR and PLS, require that the optimum number of factors or principal components are selected. This selection may lead to overfitting and/or underfitting. In this study, a factor analysis method that does not require factor selection was developed. The proposed method is useful for the determination of analytes in mixtures by DPP without the need for a prior separation or special conditions to resolve the analytes waves. The proposed method is simple, inexpensive, precise and affordable; it also requires no complex pretreatment. Hence, it is suggested for use in routine analysis of mixtures of analytes giving overlapped polarographic waves.

Acknowledgements. The authors acknowledge the financial support offered by the Research Affairs of the University of Tabriz.

ИЗВОД

"NET ANALYTE SIGNAL STANDARD ADDITION" МЕТОДА ЗА ИСТОВРЕМЕНО ОДРЕЂИВАЊЕ КАДМИЈУМА И НИКЛА

KARIM ASADPOUR-ZEYNALI, MIR REZA MAJIDI и MASOUD TAHMASEBPOUR

Department of Analytical Chemistry, Faculty of Chemistry, University of Tabriz, Tabriz 51666 16471, Iran

У раду је описана нова "net analyte signal standard addition" метода стандардног додатка за истовремено одређивање Cd^{2+} и Ni^{2+} у смеши, применом диференцијалне пулсне поларографије. Метода обједињује предности методе стандардног додатка са концептом (нето сигнал аналита) што омогућује екстраховање информације која се односи на одређени аналит из волтамограма мултикомпонентних смеша. Метода има предности јер користи целе волтамограме, добијене у једном кораку, па стога не изискује калибрацију и предвиђање. За одређивање је потребно само неколико мерења. Истовремено одређивање Cd^{2+} и Ni^{2+} у смеши изводи се у присуству Britton-Robinson-овог пуфера (pH 2,87), 0,40 M раствора калијум-тиоцијаната.

(Примљено 18. децембра 2008, ревидирано 10. априла 2009)

REFERENCES

1. M. Esteban, C. Arino, J. M. Dıaz-Cruz, *Crit. Rev. Anal. Chem.* **36** (2006) 295
2. M. Esteban, C. Arino, J. M. Dıaz-Cruz, *Trends Anal. Chem.* **25** (2006) 86
3. S. D. Brown, R. S. Bear Jr., *Crit. Rev. Anal. Chem.* **24** (1993) 99
4. M. R. Majidi, A. Jouyban, B. K. Asadpour-Zeynali, *Electroanalysis* **17** (2005) 915
5. M. R. Majidi, K. Asadpour-Zeynali, *J. Chin. Chem. Soc.* **52** (2005) 21
6. J. M. Palacios-Santander, L. M. Cubillana-Aguilera, I. Naranjo-Rodríguez, J. L. Hidalgo--Hidalgo-de-Cisneros, *Chemom. Intell. Lab. Syst.* **85** (2007) 131
7. Y. Ni, M. Selby, S. Kokot, M. Hodgkinson, *Analyst* **118** (1993) 1049
8. Y. Ni, J. Bai, L. Jin, *Anal. Chim. Acta* **329** (1996) 65
9. F. Bosch-Reig, P. Campins-Falco, *Analyst* **113** (1988) 1011
10. F. Bosch-Reig, P. Campins-Falco, *Analyst* **115** (1990) 111
11. E. Shams, H. Abdollahi, M. Yekehtaz, R. Hajian, *Talanta* **63** (2004) 359
12. L. Avraham, *Anal. Chem.* **58** (1988) 1167

13. A. J. Berger, T. W. Koo, I. Itzkan, M. S. Feld, *Anal. Chem.* **70** (1998) 623
14. L. Xu, I. Schechter, *Anal. Chem*. **69** (1997) 3722
15. H. C. Goicoechea, A. C. Olivieri, *Anal. Chem*. **71** (1999) 4361
16. H. C. Goicoechea, A. C. Olivieri, *Chemometr. Intell. Lab. Syst.* **56** (2001) 73
17. A. Lorber, K. Faber, B. R. Kowalski, *Anal. Chem.* **69** (1997) 1620
18. N. M. Faber, *Anal. Chem.* **70** (1998) 5108
19. MATLAB for Windows, The Language of Technical Computing, Ver. 6.1.0.450 Release 12.1, The MathWorks, Inc., 2001.

Journal of the Serbian Chemical Society
JSCS@tmf.bg.ac.rs • www.shd.org.rs/JSCS

J. Serb. Chem. Soc. 74 (7) 801–816 (2009)
JSCS–3878

UDC 54–148+66.063.61:532.135:543
Original scientific paper

Rheological and droplet size analysis of W/O/W multiple emulsions containing low concentrations of polymeric emulsifiers

DRAGANA D. VASILJEVIĆ*, JELENA V. PAROJČIĆ, MARIJA M. PRIMORAC and GORDANA M. VULETA

Faculty of Pharmacy, Department of Pharmaceutical Technology and Cosmetology, University of Belgrade, Vojvode Stepe 450, 11221 Belgrade, Serbia

(Received 19 December 2008, revised 30 March 2009)

Abstract: Multiple emulsions are complex dispersion systems which have many potential applications in pharmaceutics, cosmetics and the food industry. In practice, however, significant problems may arise because of their thermodynamic instability. In this study, W/O/W multiple emulsion systems containing low concentration levels of lipophilic polymeric primary emulsifiers cetyl dimethicone copolyol and PEG–30 dipolyhydroxystearate were evaluated. The concentrations of the primary emulsifiers were set at 1.6 and 2.4 % w/w in the final emulsions. Rheological and droplet size analysis of the investigated samples showed that the type and concentration of the primary lipophilic polymeric emulsifier markedly affected the characteristics of the multiple emulsions. The multiple emulsion prepared with 2.4 % w/w PEG–30 dipolyhydroxystearate as the primary emulsifier exhibited the highest apparent viscosity, yield stress and elastic modulus values, as well as the smallest droplet size. Furthermore, these parameters remained relatively constant over the study period, confirming the high stability of the investigated sample. The results obtained indicate that the changes observed in the investigated samples over time could be attributed to the swelling/breakdown mechanism of the multiple droplets. Such changes could be adequately monitored by rheological and droplet size analysis.

Keywords: W/O/W emulsions; polymeric emulsifiers; rheology; droplet size analysis.

INTRODUCTION

Multiple emulsions are complex dispersion systems, known also as “emulsions of emulsions”. The most common multiple emulsions are of the W/O/W type, although, for some specific applications O/W/O emulsions can also be prepared.

* Corresponding author. E-mail: vasilj@pharmacy.bg.ac.yu
doi: 10.2298/JSC0907801V

In W/O/W emulsions, oil globules containing small droplets of water, are dispersed in an aqueous continuous phase. Relatively high entrapment capacity for hydrophilic compounds, protection of the encapsulated substances from degradation, the ability to introduce incompatible substances into the same system and sustained active substance release are some of the advantages of these types of emulsion systems that make them potentially interesting for application in pharmaceutics, cosmetics and the food industry.[1–5] In practice, however, significant problems may arise because of their thermodynamic instability and strong tendency for coalescence, flocculation and creaming. The stability of W/O/W emulsions may be affected by a number of factors, including the method of preparation, the osmotic balance between the internal and external water phase, the phase volumes ratio and the type and concentration of the emulsifier.

Most literature data relates to multiple emulsions based on conventional non-ionic surfactants. However, most of these surfactant systems were reported to produce multiple emulsions with a limited shelf-life. Polymeric surfactants were shown to be superior to the conventional non-ionic surfactants in maintaining the physical stability of multiple emulsions.[6] According to Tadros,[7] to prepare a stable W/O/W multiple emulsion, the following criteria should be fulfilled: a) two emulsifiers (*i.e.*, one with a low and another with a high HLB value) should be used: one to produce the primary W/O emulsion and the other for the W/O/W multiple emulsion; b) polymeric emulsifiers that provide steric stabilization are necessary to maintain long-term physical stability; c) an optimum osmotic balance between the internal water droplets and the outer continuous phase should be accomplished.

The most often used primary lipophilic polymeric emulsifiers for the preparation of W/O/W emulsions are cetyl dimethicone copolyol (INCI name: cetyl PEG/PPG-10/1 dimethicone, CDC) and PEG 30-dipolyhydroxystearate (PHDS).[1–4,8–12] CDC is polymeric silicone surfactant composed of hydrophilic polyether groups, oriented into the inner water phase, and lipophilic polyalkyl groups, oriented into the oil phase. The polysiloxane backbone strengthens the whole molecule at the interface. The silicone surfactant contributes to distinct physical stability of W/O systems by steric stabilization and reduction of interfacial tension.[13] With CDC, it is possible to prepare W/O emulsions using different emulsifying procedures: hot/hot, hot/cold and cold/cold. PHDS is a triblock copolymer of polyhydroxystearic acid (PHS) / poly(ethylene oxide) (PEO) / / polyhydroxystearic acid. The PEO chain dissolves in water droplets and provides a strong “anchor” to the interface, whereas the PHS chains are highly soluble in most hydrocarbon solvents as well as in some polar ones. These PHS chains provide a strong repulsion upon approach of water droplets. PHS/PEO/ /PHS molecules also lower the interfacial tension of the W/O interface to very low values and, hence, the emulsification of water in oil is very efficient, al-

lowing the preparation of highly concentrated W/O emulsions having a low viscosity.[6] The film formed by CDC and PHDS at the W/O interface was described as reversibly expandable and compressible, while irreversibly adsorbed, which enables the formation of stable W/O/W multiple emulsions.[9,10] These emulsifiers are used in W/O/W emulsions usually at a concentration of about 4 % (in the primary W/O emulsions formulation), however the use of higher concentrations (*i.e.*, 5–15 %) has also been reported.[8] Low emulsifier concentrations are advantageous and preferred in pharmaceutical and cosmetic applications with respect to relevant toxicological, economic and environmental issues.

The objective of this study was to formulate, characterize and compare W/O/W emulsions, based on two different primary polymeric emulsifiers (cetyl dimethicone copolyol and PEG 30–dipolyhydroxystearate) at low concentration levels. The concentrations of the primary emulsifiers were set to 2.0 and 3.0 % w/w in the W/O emulsions, *i.e.*, to 1.6 and 2.4 % w/w in the final emulsions. The prepared sample formulations were characterized by dynamic and oscillatory rheological measurements and microscopic analysis and the obtained results were employed to evaluate the stability of the samples.

EXPERIMENTAL

Materials

The oil phase consisted of medium chain triglycerides (Myritol® 318, Fina, Belgium); two lipophilic polymeric surfactants were used: cetyl dimethicone copolyol (Abil® EM 90, Degussa-Goldschmidt, now Evonik, Germany) and PHS/PEO/PHS block copolymer (PEG 30-dipolyhydroxystearate, Arlacel® P135, ICI, now Croda, Belgium). Ethoxylated propylene oxide copolymer (2-methyloxirane; oxirane; INCI name: Poloxamer 407, Lutrol® PE/F127, BASF, Germany) was used as the hydrophilic surfactant. The other substances used were magnesium sulfate heptahydrate (Zorka Šabac, Serbia) and purified water.

Sample preparation

Both the primary and multiple emulsions were prepared with a high content of inner phase ($\Phi_1 = \Phi_2 = 0.80$). The compositions of the primary emulsions (PE 1 and PE 1a; PE 2 and PE 2a) are given in Table I.

TABLE I. Composition of the primary emulsions (% w/w)

Component	Emulsion			
	PE 1	PE 1a	PE 2	PE 2a
Cetyl dimethicone copolyol	2.0	3.0	–	–
PEG 30-dipolyhydroxystearate	–	–	2.0	3.0
Medium chain triglycerides	18	17	18	17
Magnesium sulfate, heptahydrate	0.70	0.70	0.70	0.70
Purified water to:	100	100	100	100

The general formulation of the multiple emulsions was as follows: primary emulsion: 80.0 g; poloxamer 407: 0.80 g; preservative q.s.; purified water: q.s. to 100.0 g.

A two-step procedure was used for the sample preparation. The first step consisted of the preparation of the primary emulsion; the second step entailed dispersing a given amount of primary emulsion in the external phase containing the secondary emulsifier.

Preparation of the primary emulsions

The primary W/O emulsions containing CDC (samples PE 1 and PE 1a) were prepared by slowly adding the aqueous phase at room temperature (22±2 °C) to the oil phase (containing the lipophilic surfactant) at the same temperature. Stirring was performed using a mechanical stirrer (Heidolph RZR 2020, Heidolph Elektro GmbH & Co. KG, Germany) at 500 rpm (6 min), 1000 rpm (1 min) and 1500 rpm (1 min).

The primary W/O emulsions containing PHDS (samples PE 2 and PE 2a) were prepared by slowly adding the aqueous phase preheated to 80±2 °C to the oil phase (containing the lipophilic surfactant) preheated to the same temperature. Stirring was performed using a mechanical stirrer (Heidolph RZR 2020, Heidolph Elektro GmbH & Co. KG, Germany) at 1000 and 1500 rpm until cooling to approximately 25 °C.

Preparation of the W/O/W emulsions

In the second step, the primary emulsion was added slowly to the aqueous phase containing the hydrophilic surfactant, while the system was stirred at 500 rpm at room temperature. After complete introduction of the primary emulsion, the stirring was continued for 20 min. The prepared multiple emulsions were designated as ME 1 and 1a and ME 2 and 2a, analogous to the designation of the primary emulsions.

Microscopic analysis

Microscopic analysis of the investigated samples was conducted in order to gain information about the multiple character of the prepared emulsions and their droplet size. An optical microscope (Olympus® BX 50, Olympus Optical Co., Tokyo, Japan) with a camera (DXC-151 Single Chip Sony CCD Camera, Sony Corporation, Tokyo, Japan) was used throughout the study. Measurements of 300 droplets per sample were performed (software Microimage, version 4.0; Olympus, Japan). For the selected samples, the measurements were repeated after different storage times. The mean droplet diameter and standard deviation were calculated for each sample.

Stability studies

The emulsions were observed for consistency, color, homogeneity and eventually phase separation during storage at room temperature (22±2 °C). Centrifugation was performed with 5 g of the samples at 1500 rpm using a laboratory centrifuge (LC 320, Tehnica, Zelezniki, Slovenia). The testing was replicated at predetermined time intervals (*i.e.*, 24 and 48 h and 7, 15 and 30 days). After 30 min of centrifugation, the samples were inspected for eventual phase separation.

Conductometric analysis was performed on selected samples to examine the release of the electrolyte initially entrapped in the internal water phase. The specific conductivity of the emulsions was measured directly using a Conductivity Meter CDM 230 (Radiometer, Copenhagen, Denmark) at 22±2 °C.

Rheological measurements

Rheological measurements were performed using a rheometer Rheolab MC 120 (Paar Physica, Stuttgart, Germany) coupled with a cone and plate measuring device MK 22 (diameter 50 mm, cone angle 1° with a 50 μm gap in the middle of the cone) for rotational and a

MK 24 (diameter 75 mm, cone angle 1° and a 50 µm gap) for oscillatory measurements, at 20±0.2 °C. The rheological measurements were performed in triplicate.

In the steady-state measurements, the shear stress was measured as a function of the shear rate. The shear rate was changed from 0 to 200 s^{-1}, and then from 200 to 0 s^{-1}. The values of the apparent viscosities (at the shear rates 10.5 and 200 s^{-1}) were used for an analysis of the samples flow.

Oscillatory measurements were performed in order to determine the linear viscoelastic region of the samples (amplitude sweep). After the linear viscoelastic region had been determined, the frequency sweep procedure was performed at a constant strain within the frequency range 0.10–10 Hz. The values of the storage modulus (G'), loss modulus (G'') and loss tangent or damping factor (tan δ) were used for sample characterization.

The relationship between G', G'' and tan δ is given by Eq. 1:

$$\tan \delta = G''/G' \quad (1)$$

RESULTS AND DISCUSSION

Immediately after preparation, the multiple emulsions were apparently white and homogenous creams. Samples ME 1 and 1a, prepared with Abil® EM 90 were notably softer than those prepared with Arlacel® P135 (samples ME 2 and 2a) at the same concentration level. The samples did not show any change in appearance and homogeneity over the investigated time period. Centrifugation testing revealed certain phase separation only in the case of sample ME 1, containing the lipophilic emulsifier Abil® EM 90 at the lower concentration level (Table II). It may be assumed that the applied emulsifier concentration was insufficient to efficiently stabilize the W/O/W emulsion.

TABLE II. Separated phase volume after centrifugation test

Samples	Volume, ml				
	24 h	48 h	7 days	15 days	30 days
ME 1	0.20	0.20	0.20	0.20	0.30
ME 1a	0.0	0.0	0.0	0.0	0.0
ME 2	0.0	0.0	0.0	0.0	0.0
ME 2a	0.0	0.0	0.0	0.0	0.0

Microscopic analysis revealed that the investigated W/O/W emulsions contained droplets with a large number of small internal droplets, *i.e.*, the samples belonged to type C multiple emulsions, as described by Florence and Whitehill.[14] The photomicrographs of the multiple emulsions ME 1a and ME 2a 48 h after preparation are shown in Fig. 1.

Rheological measurements

Steady-state rheological measurements. Rheological analysis represents the most important tool for the evaluation of multiple emulsions. These analyses have allowed, by their great versatility and power, the behavior of multiple emulsions to be characterize, changes in them induced by ageing, shear and tempe-

rature to be followed and their stability to be predicted. Moreover, the rheological properties allow the disruption mechanisms of the oily globules, which occur either by osmotic swelling or simple shear flow to be described and controlled.[15,16]

The results of the steady-state rheological measurements have shown that all the investigated samples exhibited non-Newtonian plastic flow behavior, as demonstrated by the stress-shear rate curves given in Figs. 2 and 3. Such flow behavior is typical of very concentrated emulsions, with a volume fraction $\Phi >$ > 0.74.[16] All the samples showed shear-thinning behavior: the apparent viscosity decreased with increase in shear rate.

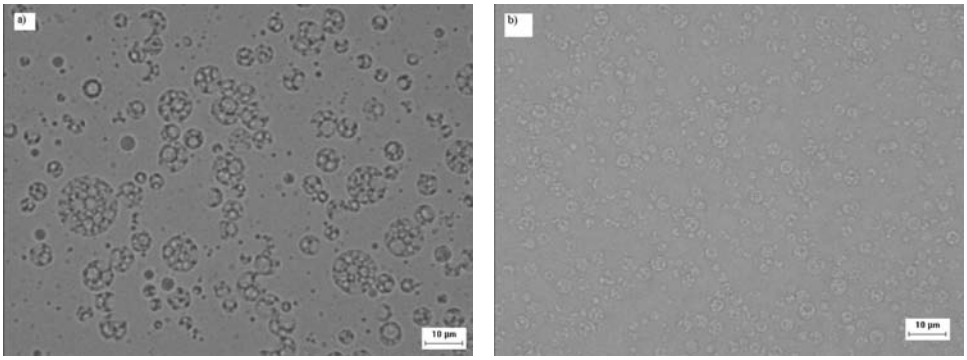

Fig. 1. Photomicrographs of the multiple emulsions, 48 h after preparation (magnification 1000×): a) ME 1a and b) ME 2a.

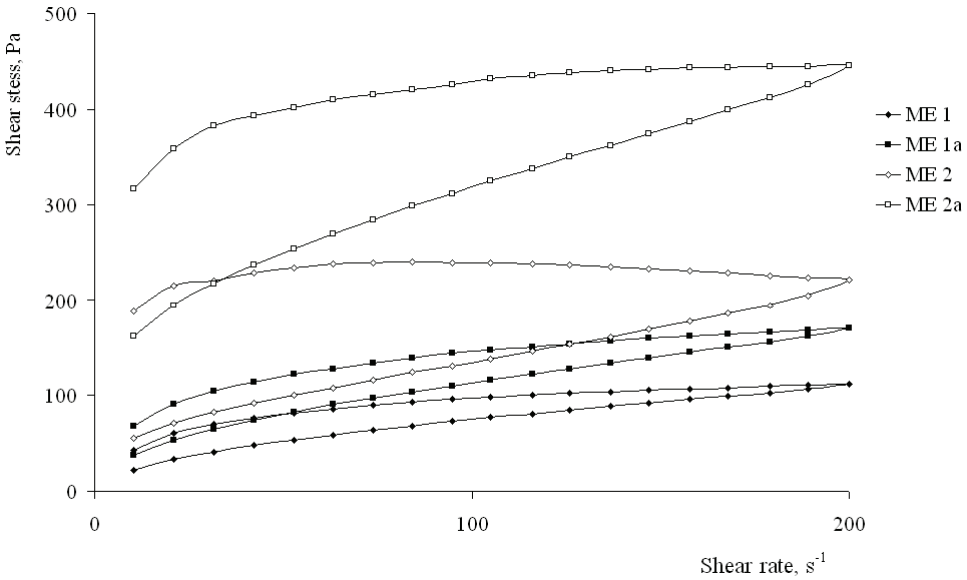

Fig. 2. Flow curves of the multiple emulsion samples, 24 h after preparation.

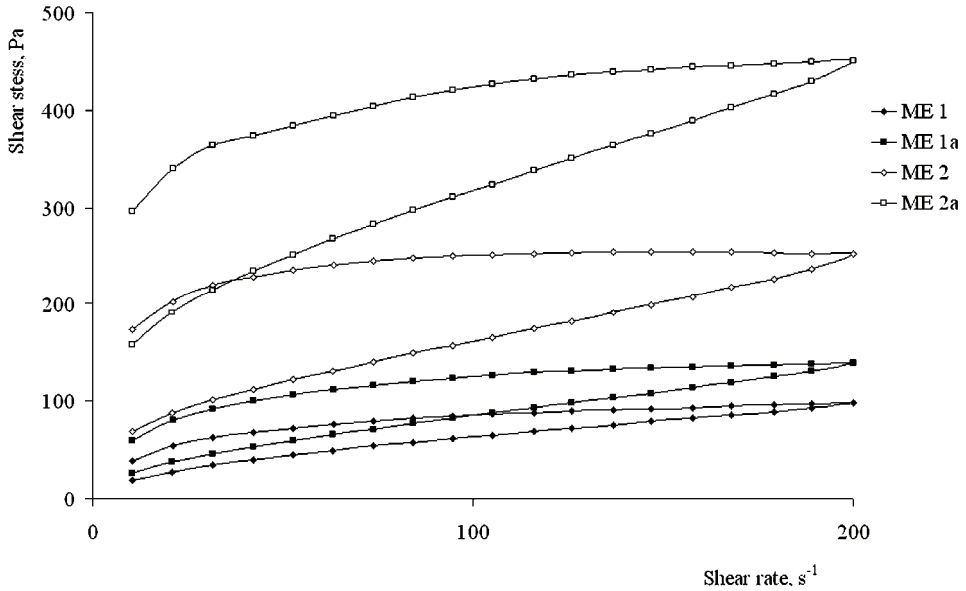

Fig. 3. Flow curves of the multiple emulsion samples, 30 days after preparation.

It can be observed that the download curve is below the upward curve, indicating thixotropy in the system. In such a case, the shear stress induces structural changes, *i.e.*, a break of multiple droplets – the maximum shear produces a decrease in the volume fraction, which results in a decrease in the viscosity.[16]

The upward curves were analyzed by applying different mathematical models using data analysis software (US 200, Paar Physica, Stuttgart, Germany). The best fit ($R > 0.99$) was obtained by the 3rd order polynomial:

$$\tau = a + b\gamma + c\gamma^2 + d\gamma^3 \quad (2)$$

where τ is the shear stress, γ is shear rate, and a, b, c and d are coefficients of the 0th, 1st, 2nd and 3rd order, respectively. The 0th order coefficient represents the yield stress (yield point or yield value) which can be used to detect the maturation process of emulsions.[17,18]

The values of the yield stress calculated according to the mathematical model described above and the apparent viscosity values extrapolated from the flow curves are given Table III.

The apparent viscosities and yield stress values of the investigated W/O/W emulsions were markedly influenced by the type and concentration of the lipophilic emulsifier. For both the investigated emulsifiers, higher apparent viscosity and yield stress values were obtained for the W/O/W emulsion prepared with the higher emulsifier concentration. At the same concentration level, the W/O/W emulsions prepared with PHDS exhibited a significantly higher apparent visco-

sity and yield stress values. As can be seen from Table III, there was a general trend towards a decrease of the apparent viscosity and yield stress values of the samples with time. This could be attributed to the coalescence of the internal water droplets with the external water phase, as discussed by Jiao and Burgess.[19] The subsequent increase in the volume of the external water phase of the W/O/W emulsions may lead to a decrease of the apparent viscosities and yield stresses. This phenomenon was less pronounced at the higher concentration level for both the investigated emulsifiers. The constancy of the apparent viscosity and yield stress values was the highest for the sample ME 2a.. Therefore, samples prepared with 2.4 % w/w primary emulsifier were selected for further comparative characterization.

TABLE III. Apparent viscosities (η_{app}) and yield value (τ_0) of the W/O/W emulsions during storage

Time	η_{app}[a] / Pa s (at 10.5 s^{-1})	η_{app}[a] / Pa s (at 200.0 s^{-1})	τ_0[a] / Pa
	Sample ME 1		
24 h	4.1 (0.30)	0.56 (0.020)	31 (2.9)
48 h	4.0 (0.06)	0.57 (0.010)	29 (1.1)
7 days	4.1 (0.21)	0.53 (0.032)	32 (1.4)
15 days	3.9 (0.06)	0.52 (0.052)	31 (1.3)
30 days	3.6 (0.06)	0.48 (0.020)	27 (0.9)
	Sample ME 1a		
24 h	6.5 (0.21)	0.85 (0.006)	52 (2.8)
48 h	6.6 (0.46)	0.83 (0.035)	54 (5.1)
7 days	6.3 (0.51)	0.80 (0.061)	50 (1.0)
15 days	6.0 (0.11)	0.78 (0.025)	51 (6.1)
30 days	6.1 (0.20)	0.79 (0.076)	50 (1.9)
	Sample ME 2		
24 h	17.9 (0.65)	1.11 (0.110)	177 (7.8)
48 h	17.9 (0.25)	1.32 (0.035)	174 (2.7)
7 days	17.3 (0.72)	1.10 (0.154)	172 (2.3)
15 days	17.3 (0.68)	1.21 (0.157)	167 (3.3)
30 days	16.5 (0.72)	1.26 (0.139)	158 (3.4)
	Sample ME 2a		
24 h	30.1 (0.80)	2.23 (0.011)	299 (9.0)
48 h	30.0 (0.76)	2.10 (0.100)	296 (3.4)
7 days	30.4 (0.64)	2.24 (0.216)	301 (3.1)
15 days	29.2 (0.91)	2.15 (0.334)	292 (3.9)
30 days	29.4 (1.65)	2.25 (0.196)	294 (20.4)

[a]$\pm SD$ (n = 3)

Oscillatory rheological measurements. The storage modulus (G') and loss angle (δ) provide quantitative characterization of the balance between the viscous and elastic properties of multiple emulsions.[16] The loss angle (δ) is a very precise

indicator of this balance, the lower the δ value, the more pronounced is the elastic character, and *vice versa*.

The values of the basic viscoelastic parameters of the investigated samples ME 1a and ME 2a are given in Table IV.

TABLE IV. Storage modulus (*G*'), loss modulus (*G*'') and tan δ of the samples ME 1a and ME 2a during storage (at 1 Hz)

Time	*G*'[a] / Pa	*G*''[a] / Pa	tan δ[a]
	Sample ME 1a		
24 h	740 (96.0)	232 (26.2)	0.31 (0.032)
48 h	642 (22.3)	268 (28.0)	0.42 (0.035)
7 days	581 (31.7)	203 (16.0)	0.35 (0.035)
30 days	692 (51.6)	240 (14.4)	0.35 (0.014)
90 days	463 (51.1)	252 (12.5)	0.55 (0.074)
	Sample ME 2a		
24 h	1220 (66.6)	290 (40.6)	0.24 (0,020)
48 h	1320 (32.1)	440 (64.2)	0.33 (0.055)
7 days	1380 (122.9)	503 (12.6)	0.36 (0.020)
30 days	1260 (68.0)	440 (21.8)	0.35 (0.040)
90 days	1120 (17.3)	370 (10.1)	0.33 (0.010)

[a]$\pm SD$ (n = 3)

The storage (*G*') and loss (*G*'') moduli values of the multiple emulsion systems are presented as a function of frequency for the samples evaluated 24 h, 48 h and 90 days after the preparation are shown in Figs. 4–6, respectively. When a stable sample is stressed in the linear viscoelastic range, the storage modulus (*G*') predominates and is larger than the loss modulus (*G*''). For stable samples, the curves for both moduli are nearly parallel over the entire measured frequency range.[17]

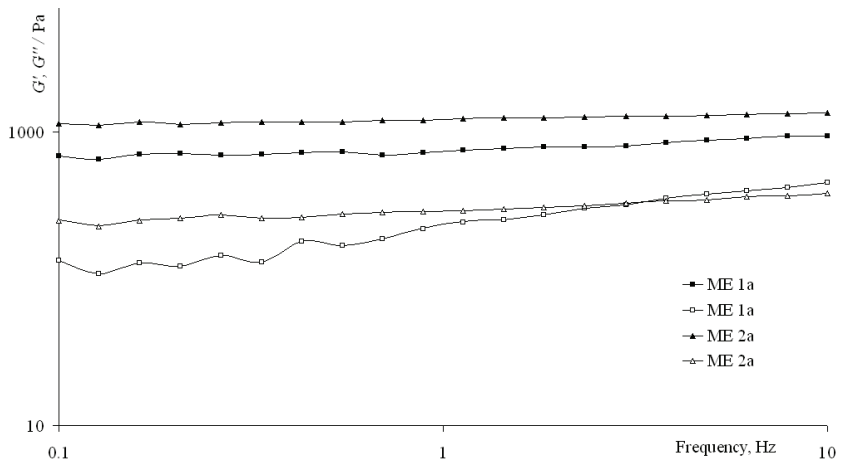

Fig. 4. Storage moduli (*G*') (filled symbols) and loss moduli (*G*'') (open symbols) of the multiple emulsion samples, 24 h after preparation.

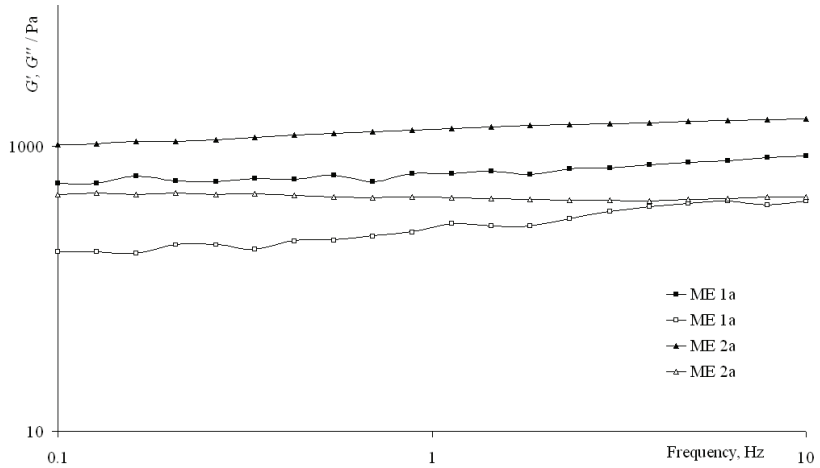

Fig. 5. Storage moduli (*G'*) (filled symbols) and loss moduli (*G''*) (open symbols) of the multiple emulsion samples, 48 h after preparation.

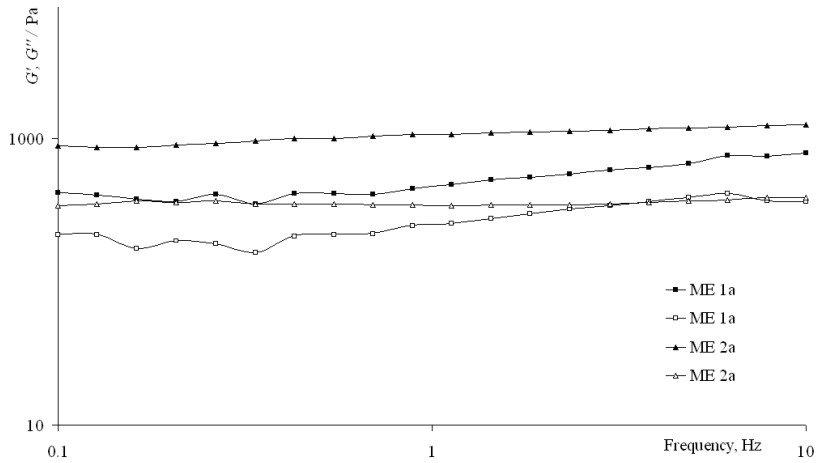

Fig. 6. Storage moduli (*G'*) (filled symbols) and loss moduli (*G''*) (open symbols) of the multiple emulsion samples, 90 days after preparation.

The high elasticity of these systems is a result of the high volume fraction of the multiple emulsions (0.80) and hence droplet interactions are significant, resulting in predominantly elastic systems.[20]

The type of the primary emulsifier had a significant impact on the oscillatory parameters of the investigated samples. At the same concentration of lipophilic polymeric emulsifier, the formulation with PHDS showed a markedly higher elasticity. The formulation ME 2a was highly viscoelastic or "solid-like", as indicated by the considerably higher *G'* values and lower tan δ values.

The observed higher value of the storage modulus of the sample ME 2a was accompanied by smaller droplet sizes in this sample (Table V). It was reported that, the smaller the diameter of the multiple emulsion droplets, the greater the number of contact points between them, which leads to an increase in storage modulus values.[21]

TABLE V. Droplet size of the samples ME 1a and ME 2a during storage

Time	Droplet size[a], μm
Sample ME 1a	
48 h	7.7 (1.29)
30 days	8.9 (2.09)
90 days	10.6 (1.94)
Sample ME 2a	
48 h	4.6 (0.70)
30 days	4.6 (0.82)
90 days	4.9 (1.19)

[a]±S.D. (n = 300)

As may be seen from Table IV, there were relatively large changes in the oscillatory characteristics of the investigated samples during the first 48 h after preparation. Such changes describe a classical "ripening step" of emulsions.[16] Following this initial period, the sample ME 1a exhibited acceptable stability only during the first month, while in the case of the sample ME 2a, the changes observed were negligible over the whole storage time evaluated.

When analyzing the droplet size (Table V) and the oscillatory rheological parameter values (Table IV) for the sample ME 1a, it is noticeable that the droplet size increases both 30 and 90 days after preparation, while the elasticity initially increases and then decreases. Water may penetrate from the outer water phase into the inner one by virtue of the osmotic pressure difference. The resulting water flow produces an increase in the internal water droplets size. Consequently, the oil globules swell, until a critical size is reached. Beyond this critical size, the multiple globules may split by breakdown of the oily membrane, as described by Grossiord and Seiller[16] and Geiger *et al.*[22] It may be assumed that the swelling of the multiple globules observed 30 days after preparation leads to an increase in the elasticity of the system, due to the decrease in the volume of the external water phase volume.

Ninety days after preparation, the increase in the droplet size was still pronounced, the storage modulus was markedly reduced and tan δ was higher. The observed elasticity reduction may be explained by the breakup of the oily membrane and expulsion of the internal water droplets into the continuous medium, which results in a decrease in the volume fraction of the multiple emulsion and increase in the external aqueous phase.[21] Although a continuous increase in the

multiple droplets size with time was evident, it may be postulated that the observed discrepancy in the elastic characteristics of the samples 30 and 90 days after preparation is the consequence of the reduced number of multiple droplets per unit volume. In the case of sample ME 2a, the changes in its elastic characteristics with time were less pronounced.

Conductometric analysis

The stability of sample ME 2a during storage was also confirmed by conductometric analysis (Table VI).

TABLE VI. Specific conductivity values (μS/cm) of the samples ME 1a and ME 2a during storage

Sample	Storage time				
	24 h	48 h	7 days	30 days	90 days
ME 1a	115.2	116.6	127.0	130.6	141.0
ME 2a	19.1	20.6	21.4	22.2	23.2

At the same level of the preservative concentration, differences in the specific conductivity of the samples occurred as a consequence of magnesium sulfate heptahydrate release from the inner water phase in which it was initially incorporated. Rupture of some multiple droplets, which could occur in the second phase of the emulsification process, could lead to mixing of the outer water phase with some amount of the inner water phase. Probably, it may be assumed that this phenomenon is more likely to occur in sample ME 1a, prepared with the lipophilic emulsifier CDC, and that this is the reason for the high initial conductivity values recorded in this sample (Table VI). During storage, the specific conductivity values of the samples increased slightly. Such observations could be attributed to the further rupture of multiple droplets with time. The degree of change observed was lower in the case of the multiple emulsion ME 2a, indicating its superior stability.

Droplet size analysis

The results of droplet size analysis of the investigated samples are given in Table V and Fig. 7.

Particle size analysis gives useful information about the stability of multiple emulsions. It also enables the observation of the growth process of particles dispersed in multiple emulsions; accordingly, the evolution of their dimension with time.[23] It may be observed (Table V) that the type of lipophilic polymeric emulsifies had a significant influence on the droplet size of the investigated W/O/W emulsions. The average particle diameters in samples ME 1a and ME 2a 48 h after preparation were 7.7 and 4.6 μm, respectively. At the same concentration level, in the case of the PHDS-based emulsions, both the inner water droplets and

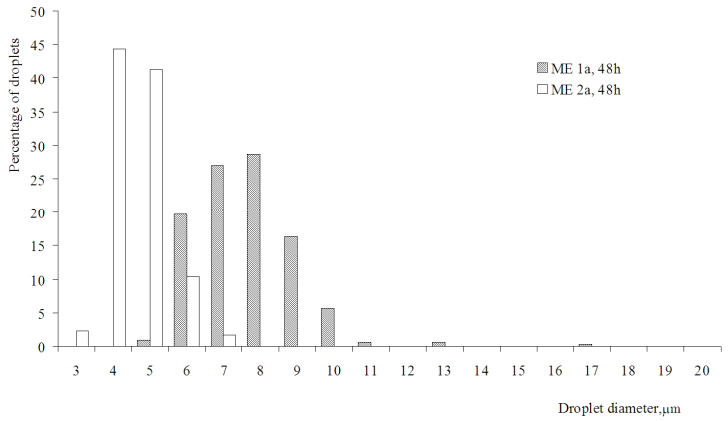

(a)

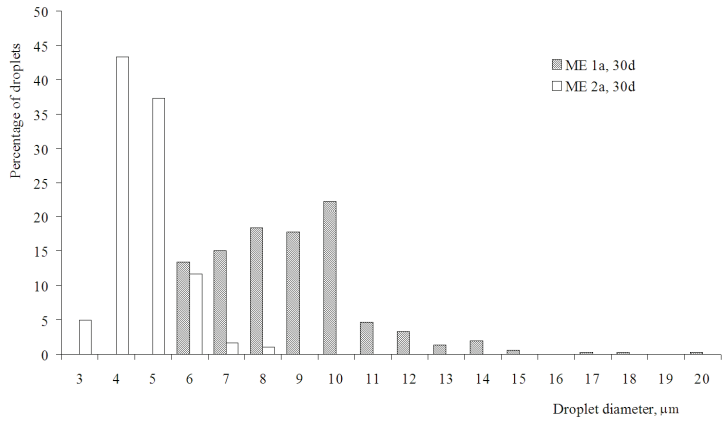

(b)

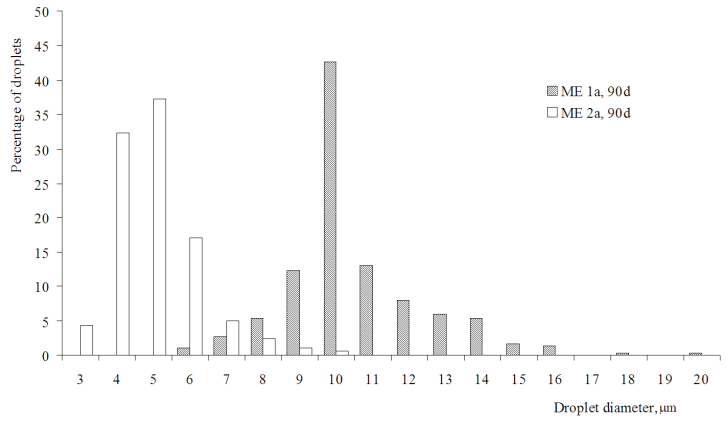

(c)

Fig. 7. Distribution histograms of the multiple droplet size for emulsion ME 1a and ME 2a: 48 h (a), 30 days (b) and 90 days (c) after preparation.

multiple droplets size were smaller compared to the CDC-based emulsions. The inner water droplets size was about 1.5 and 0.70 μm for samples ME 1a and ME 2a, respectively, although the size of the droplets that were in contact could not be determined accurately. It may be noticed that the range order of the estimated droplet size correlated with the apparent viscosity of the primary emulsions, as the apparent viscosity values were 16.0 and 2.80 Pa s (at 10.5 s^{-1}) for samples PE 1a and PE 2a, respectively. The less viscous primary emulsion (PE 2a) was also easier to re-emulsify compared to the semi-solid primary emulsion PE 1a.

As discussed above, a continuous increase in droplet size with time was observed in the case of sample ME 1a, while the droplet size remained almost constant for sample ME 2a. A certain increase in droplet size, observed 90 days after preparation, may be attributed to droplet swelling. It appears that PHDS more efficiently prevents multiple droplets swelling than CDC used at the same concentration level.

The distribution histograms of the multiple droplet size for ME 1a and ME 2a are presented in Fig. 7. In the case of sample ME 1a, 48 h after preparation, about 55 % of the droplets had a diameter between 7 and 8 μm. However, their increase with time resulted in more than 40 % of the droplets having a diameter of 10 μm 90 days after preparation. In the case of sample ME 2a, more than 85 % of the droplets had a diameter between 4 and 5 μm 48 h after preparation. The droplet size distribution remained almost unchanged with time.

CONCLUSIONS

W/O/W multiple emulsions containing low concentrations (1.6 and 2.4 %) of the primary polymeric emulsifier (cetyl dimethicone copolyol or PEG–30 dipolyhydroxystearate) were prepared and characterized with respect to their droplet size and rheological behavior. The type and concentration of the applied lipophilic polymeric emulsifier markedly affected the characteristics of the W/O/W multiple emulsions. CDC used at the lower concentration level was found insufficient to efficiently stabilize the W/O/W emulsion. The sample containing 2.4 % PHDS exhibited consistent storage and loss moduli values and droplet size over a 90-day time span, indicating the favorable long-term stability of the resulting emulsion. The results obtained indicate that this semi-solid W/O/W emulsion offers potential advantages as a vehicle for dermopharmaceutical and cosmetic preparation development and merits further investigation.

ИЗВОД

ОДРЕЂИВАЊЕ РЕОЛОШКИХ КАРАКТЕРИСТИКА И ВЕЛИЧИНЕ КАПИ W/O/W ВИШЕСТРУКИХ ЕМУЛЗИЈА ДОБИЈЕНИХ ПРИ НИСКОЈ КОНЦЕНТРАЦИЈИ ПОЛИМЕРНИХ ЕМУЛГАТОРА

ДРАГАНА Д. ВАСИЉЕВИЋ, ЈЕЛЕНА В. ПАРОЈЧИЋ, МАРИЈА М. ПРИМОРАЦ и ГОРДАНА М. ВУЛЕТА

Фармацеутски факултет, Институт за фармацеутску технологију и козметологију, Универзитет у Београду, Војводе Степе 450, 11221 Београд

Вишеструке емулзије су сложени дисперзни системи, са великим могућностима примене у фармацији, козметици и прехрамбеној индустрији. Међутим, у пракси се јављају значајни проблеми због њихове изражене термодинамичке нестабилности. У овом раду су испитиване W/O/W вишеструке емулзије које садрже ниску концентрацију липофилних полимерних емулгатора цетил диметикон кополиола и PEG-30 диполихидроксистеарата. Концентрације наведених емулгатора у W/O/W емулзијама су износиле 1,6 и 2,4 mas %. Врста и концентрација липофилног полимерног емулгатора веома утиче на реолошке карактеристике и величину капи испитиваних емулзија. Вишеструка емулзија добијена при 2,4 mas % PEG-30 диполихидроксистеарата има највеће вредности испитиваних реолишких параметара (привидна вискозност, напон попуштања, еластични модул) и најмању величину капи. Наведени параметри се током испитиваног временског периода незнатно мењају, што указује на добру стабилност W/O/W емулзије са 2,4 mas % PEG-30 диполихидроксистеарата. Такође, добијени резултати указују да се промене, које се дешавају током времена у испитиваним вишеструким емулзијама, могу приписати механизму бубрења/пуцања сложених капи, што је праћено одређивањем реолошких карактеристика и величине капи.

(Примљено 19. децембра 2008, ревидирано 30. марта 2009)

REFERENCES

1. M. Bonnet, M. Cansell, A. Berkaoui, M. H. Ropers, M. Anton, F. Leal-Calderon, *Food Hydrocoll.* **23** (2009) 92
2. J. W. Kim, H. H. Kang, K. D. Suh, S. G. Oh, *J. Dispersion Sci. Technol.* **24** (2003) 833
3. G. M. Tedajo, S. Bouttier, J. Fourniat, J. L. Grossiord, J. P. Marty, M. Seiller, *Int. J. Pharm.* **288** (2005) 63
4. D. Vasiljević, J. Parojčić, M. Primorac, G. Vuleta, *Int. J. Pharm.* **309** (2006) 171
5. S. Farahmand, H. Tajerzadeh, E. S. Farboud, *Pharm. Dev. Technol.* **11** (2006) 255
6. T. F. Tadros, M. C. Taelman, J. C. Dederen, in *Multiple Emulsions: Structure, Properties and Applications*, J. L. Grossiord, M. Seiller, Eds., Editions de Sante, Paris, 1998, p. 117
7. T. F. Tadros, in *Colloids in Cosmetics and Personal Care*, T. F. Tadros, Ed., Wiley-VCH Verlag GmbH & Co. KG., Weinheim, 2008, p. 1
8. Ö. Özer, E. Baloglu, G. Ertan, *Int. J. Cosmetic Sci.* **22** (2000) 459
9. M. Kanouni, H. L. Rosano, N. Naouli, *Adv. Colloid Interface Sci.* **99** (2002) 229
10. M. Kanouni, H. L. Rosano, in *Delivery System Handbook for Personal Care and Cosmetic Products*, M.R. Rosen, Ed., William Andrew Inc., Norwich, 2005, p. 473
11. A. Kovács, I. Csóka, M. Kónya, E. Csányi, A. Fehér, I. Erős, *J. Therm. Anal. Calorim.* **82** (2005) 491
12. D. Vasiljević, G. Vuleta, M. Primorac, *Int. J. Cosmetic Sci.* **27** (2005) 81
13. M. Gašperlin, L. Tušar, M. Tušar, J. Kristl, J. Šmid-Korbar, *Int. J. Pharm.* **168** (1998) 243
14. A. T. Florence, D. Whitehill, *Int. J. Pharmacol.* **11** (1982) 277

15. I. Terrisse, M. Seiller, A. Rabaron, J. L. Grossiord, A. Magnet, C. Le Hen-Ferrenbach, *Int. J. Cosmetic Sci.* **15** (1993) 53
16. J. L. Grossiord, M. Seiller, in *Multiple Emulsions: Structure, Properties and Applications*, J. L. Grossiord, M. Seiller, Eds., Editions de Sante, Paris, 1998, p. 169
17. R. Brummer, *Rheology Essentials of Cosmetic and Food Emulsions*, Springer, Berlin, Heidelberg, 2006
18. T. G. Mezger, *The Rheology Handbook*, Vincenty Network, Hannover, 2006
19. J. Jiao, D. J. Burgess, *AAPS Pharm. Sci*. **5** (2003) 62
20. C. Py, J. Rouviere, P. Loll, M. C. Taelman, T. F. Tadros, *Colloids Surf. A* **91** (1994) 215
21. T. F. Tadros, C. Py, J. Rouviere, M. C. Taelman, P. Loll, in *Proceeding of In-Cosmetics Conference*, (1995), Barcelona, Spain, (1994), p. 447
22. S. Geiger, S. Tokgoz, A. Fructus, N. Jager-Lezer, M. Seiller, C. Lacombe, J. L. Grossiord, *J. Controlled Release* **52** (1998) 99
23. L. Ursica, D. Tita, I. Palici, B. Tita, V. Vlaia, *J. Pharmaceut. Biomed.* **37** (2005) 931.

Journal of the Serbian Chemical Society
JSCS@tmf.bg.ac.rs • www.shd.org.rs/JSCS

J. Serb. Chem. Soc. 74 (7) 817–831 (2009)
JSCS–3879

UDC 54.02.004.12:621.793:544.654.2+546.74:539.4
Original scientific paper

Micromechanical and structural properties of nickel coatings electrodeposited on two different substrates

JELENA LAMOVEC[1*#], VESNA JOVIĆ[1#], RADOSLAV ALEKSIĆ[2] and VESNA RADOJEVIĆ[2]

[1]*Institute of Chemistry, Technology and Metallurgy – Center of Microelectronic Technologies and Single Crystals, Njegoševa 12, Belgrade and* [2]*Faculty of Technology and Metallurgy, University of Belgrade, Karnegijeva 4, Belgrade, Serbia*

(Received 23 December 2008, revised 14 April 2009)

Abstract: Fine-structured nickel coatings were electrodeposited from a sulfamate-based electrolyte onto different substrates: polycrystalline cold-rolled copper and single crystal silicon with (111) orientation. The influence of the substrate layers and chosen plating conditions on the mechanical and structural properties of these composite structures were investigated by Vickers microhardness testing for different loads. Above a certain critical penetration depth, the measured hardness value was not the hardness of the electrodeposited film, but the so-called "composite hardness", because the substrate also participated in the plastic deformations during the indentation process. Two composite hardness models (Chicot–Lesage and Korsunsky), constructed on different principles, were chosen and applied to the experimental data in order to distinguish film and substrate hardness. The microhardness values of the electrodeposited nickel layers were mainly influenced by the current density. Increasing the current density led to a decrease in grain size, which resulted in higher values of the microhardness.

Keywords: Vickers microhardness; composite hardness; hardness models; nickel electrodeposition; sulfamate-based electrolyte.

INTRODUCTION

One of the areas of microelectromechanical systems (MEMS) is to fabricate small integrated systems containing sensors, actuators, signal conditioning circuits and additional functional devices with physical dimensions ranging from a couple to a few hundred micrometers. These micromechanical parts are fabriccated by selected combinations of different materials and technologies and may be represented as composite structures of substrate (bulk) materials and thin

* Corresponding author. E-mail: jejal@nanosys.ihtm.bg.ac.rs
# Serbian Chemical Society member.
doi: 10.2298/JSC0907817L

films/coatings. Due to this, good mechanical material properties are critical for the integrity of microsystems. Tribology (friction and wear) is an important factor affecting the performance and reliability of MEMS.

Electrodeposition is a promising technology, especially for the realization of different movable structures for MEMS applications. It is important that it is possible to fabricate movable structures consisting of layers with a very low level of internal (residual) stress. This can be achieved with various materials with widely diverse properties, such as composition, crystallographic orientation and grain size. The properties of electrodeposited materials are affected by the processing parameters. Through controlling the grain size and microstructure, metals can be strengthened and hardened with little or no loss of ductility. Electrodeposition is an IC compatible, low-temperature and high rate deposition technology.

Nickel is widely used material for electrodeposition. Conventional, large--grained nickel is expected to deform whereas electrodeposited fine-grain-structured nickel will resist. Electrodeposited nickel has good mechanical properties, such as high yield strength and hardness, which are beneficial in high-aspect--ratio microstructures.

As a guide to the ability of a material to resist deformation, especially for thin films and coatings, the indentation hardness test is commonly used. An evaluation of the hardness of thin films and coatings (for some materials up to 50 μm-thick films) is difficult to realize because the influence of the substrate must be considered. The measured hardness varies continuously with indentation depth, film thickness and the hardness of the film and the substrate. The substrate commences to contribute to the measured hardness at indentation depths of the order of 0.07–0.20 times the coating thickness. Above a certain critical penetration depth, the measured hardness is called composite hardness and includes a component of the substrate hardness.

COMPOSITE HARDNESS MODELS

There is a necessity to obtain the hardness of the coating alone from experimental composite hardness measurements. Several models which operate on a number of different principles exist. The predictive model advanced by Chicot––Lesage and descriptive model by Korsunsky will be examined and applied to different types of composite systems.

The model proposed by Chicot and Lesage (the C–L model) avoids knowledge or choice of any data other than that obtained easily from standard measurements (thickness and apparent hardness).[1,2] They constructed a model based on the analogy between the variation of the Young modulus of reinforced composites as a function of the volume fraction of particles and the variation of the composite hardness between the hardness of the substrate and that of the film.[3]

The value of hardness deduced from an indentation test is not constant because hardness is load-dependent. The Meyer law expresses the variation of the size of the indent, *d*, as a function of the applied load, *P*. For the particular case of a film-substrate couple, the evolution of the measured diagonal and the applied load can be expressed by a similar relation to that of Meyer:

$$P = a * d^{n*} \tag{1}$$

The variation part of the hardness number with load is represented by the factor n^*. They then adopted the following expression:

$$f\left(\frac{t}{d}\right) = \left(\frac{t}{d}\right)^m = f \quad \text{where}: m = \frac{1}{n^*} \tag{2}$$

Now the composite hardness can be expressed by the following relation:

$$H_C = (1-f)/\left(1/H_S + f\left(\frac{1}{H_F} - \frac{1}{H_S}\right)\right) + f\left(H_S + f\left(H_F - H_S\right)\right) \tag{3}$$

The hardness of the film is the positive root of the following equation:

$$AH_F^2 + BH_F + C = 0 \tag{4}$$

with:

$$A = f^2(f-1)$$

$$B = \left(-2f^3 + 2f^2 - 1\right)H_S + (1-f)H_C$$

$$C = fH_C H_S + f^2(f-1)H_S^2$$

The value of *m* (composite the Meyer index of the composite) is calculated by a linear regression performed on all the experimental points obtained for a given film substrate couple and deduced from the relation:

$$\ln d = m \ln P + b \tag{5}$$

With the value of *m* known, only the hardness of the films remains to be calculated.

Korsunsky and co-workers[4,5] advanced a different approach to analyze hardness data for coated materials, employing dimensionless parameters. The model is applicable to either plasticity- or fracture-dominated behavior, with all scales measured relative to the coating thickness. The approach is based on the assumption that the total work-of-indentation during a hardness test is composed of two parts: the plastic work of deformation in the substrate and the deformation and/or fracture energy in the coating. The composite hardness, H_C, according to this model is given by:

$$H_C = H_S + \left[\frac{1}{1+k'd^2/t}\right](H_F - H_S), \quad k' = \frac{k}{49t} \tag{6}$$

where k represents a dimensionless materials parameter related to the composite response mode to indentation, d is the indent diagonal and t is the thickness of the film. It is not possible to compute the film hardness at each indentation diagonal value since the magnitude of k should also be determined simultaneously from the experimental measurements of the composite hardness. This model does not allow the change in the film hardness with the indentation diagonal to be computed from the individual measurements of this property.

EXPERIMENTAL

The materials chosen for the experimental investigation were electrodeposited nanocrystalline Ni on two different substrates: polycrystalline cold-rolled copper and single crystal Si wafers with (111) orientation. The plating base for the silicon wafers were sputtered layers of 100 Å Cr and 800 Å Ni. Electroplating was performed using the direct current galvanostatic mode from a sulfamate bath consisting of 300 g/l $Ni(NH_2SO_3)_2$ $4H_2O$, 30 g/l $NiCl_2$ $6H_2O$, 30 g/l H_3BO_3 and 1.0 g/l saccharine. The pH value and the temperature of the process were maintained at 4.00 and 50 °C, respectively. The current density values were maintained at 10 and 50 mA cm^{-2}, which resulted in variations in the microstructures and thus in the mechanical properties. The deposition time was determined according to the plating surface and projected thickness of the deposit (2–50 μm).

In order to observe the coating microstructure, a solution of 25 ml water, 25 ml acetic acid and 50 ml nitric acid was used as an etchant. Coating microstructures were characterized by conventional scanning electron microscopy (SEM).

The mechanical properties of the films were characterized using a Vicker's microhardness tester "Leitz, Kleinharteprufer DURIMET I" using up to 15 loads, ranging from 4.9 down to 0.049 N. Three indentations were made at each load, yielding six measurements of the indentation diagonals, from which the average hardness could be calculated. The indentation was performed at room temperature. The experimental data were fitted with GnuPlot, version 4.0 (http://www.gnuplot.info/).

Following the mechanical testing, the samples were prepared for examination by metallographic microscopy (Carl Zeiss microscope "Epival Interphako").

The topographic details were investigated by means of an atomic force microscope (AFM) named "TM Microscopes – Veeco", operating in the non-contact mode.

RESULTS AND DISCUSSION

Surface morphology

The structure of the electrodeposited nickel is related to the plating variables, such as type of electrolyte bath, current density, pH value and temperature.

An SEM image of the surface morphology of an as-plated sample deposited at a current density of 10 mA cm^{-2} is shown in Fig. 1. According to the literature, plated structures consist of small substructures, named "colonies", with deep, large crevices between them.[6] They were defined as series of very fine grains that tend to form groups.

An SEM picture of an etched plated surface under a higher magnification than previous one is shown in Fig. 2, from which very fine substructures can be seen The size of these structures are of the order of 0.5–3 μm. From this Figure, it is not possible to determine whether the observed structures are grain boundaries or colonies. A colony boundary may be a grain boundary, but a grain boundary is not necessarily defined by a colony boundary, which may contain finer grains.[6]

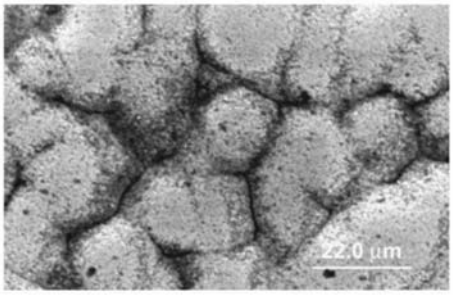

Fig. 1. SEM Image of the as-plated surface morphology that can be seen in samples deposited at a current density of 10 mA·cm^{-2}. The plated structures consist of small substructures, named "colonies", and deep, large crevices among them. They were defined as a series of very fine grains that tend to form groups.

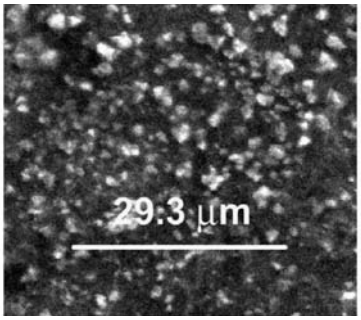

Fig. 2. With increasing depth moving towards the Ni film-substrate interface, the film structures become smaller. The dimensions of these structures are of the order of 0.5–3 μm. A colony boundary may be a grain boundary, but a grain boundary is not necessarily defined by a colony boundary, which may contain finer grains.

From the AFM of the etched surface of a nickel film (10 μm, 50 mA cm^{-2}) shown in Fig. 3, the colonies appear like columnar grains with deep crevices among them.

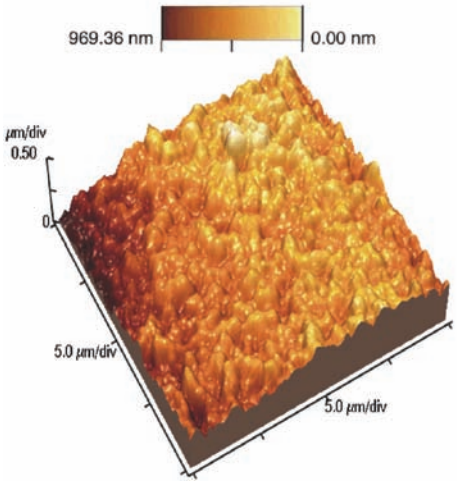

Fig. 3. Topographic AFM image of an electrodeposited Ni film (10 μm, 50 mA cm^{-2}) etched for 60 s showing structures of columnar grains.

Determination of the absolute hardness of the substrates

Tests were performed with a Vickers diamond pyramidal indenter both on uncoated substrates and various coated substrates. Vickers microhardness indentation tests were performed on a Si single crystal substrate in such a way that the indent diagonal was parallel with the prime flat (*i.e.*, the diagonals were parallel to the <110> orientations). It is well known that the mechanical properties of single crystals depend on the crystallographic orientation and this indenter orienttation procedure was strictly applied during indentation.[8]

The average values of the impression diagonals, d, were calculated from several independent measurements on every specimen for different applied loads P. The composite hardness, H_C, was calculated using the formulae:

$$H_C = 0.01854 P d^{-2} \tag{7}$$

where 0.01854 is a geometrical factor for the Vickers pyramid.

The classical Meyer Law, Eq. (1), is insufficient for a description of the experimental data but it was found that the proportional specimen resistance (PSR) model is suitable for analyzing the variation of microhardness with load.[9] According to the PSR model, the indentation test load, P, is related to indentation size, d, as follows:

$$P = a_1 d + d^2 P_c / d_0^2 \tag{8}$$

In Eq. (8), P is the critical applied test load above which the microhardness becomes load independent and d_0 is the corresponding diagonal length of the indent. A plot of P/d against d will give a straight line, the slope of which gives the value for the calculation of the load independent microhardness.

The P/d values are plotted against d for the two tested substrates: polycrystalline cold-rolled Cu and single-crystalline (111)-oriented Si in Figs. 4a and 4b, respectively. A linear relationship was confirmed for both substrates. The slope gives the value of P/d_0^2, which, when multiplied by the Vicker's conversion factor, 0.01854 from Eq. (7) gives the value of the load independent microhardness, H_S. These calculated values are given in Fig. 4 for each substrate.

Composite hardness and film hardness

Two different composite systems were investigated: a hard film of electrodeposited nickel on a soft polycrystalline Cu substrate and a soft film of electrodeposited nickel on a hard single crystal substrate of (111)-oriented Si.

Hard film on a soft substrate. The change of the composite hardness, H_C, of the Ni film on Cu substrate system with the relative indentation depth, expressed as indentation depth h through film thickness t, h/t, is shown in Fig. 5. Nickel films with different thicknesses, ranging from 1.2 up to 50 μm, were obtained with two current densities (10 and 50 mA cm^{-2}).

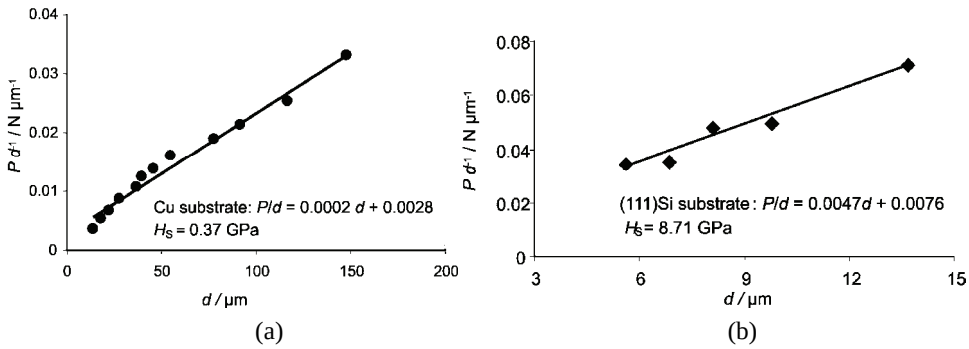

(a) (b)

Fig. 4. PSR Plot of applied load through indent diagonal, *P*/*d* *vs*. indent diagonal, *d*, for a) cold-rolled Cu substrate and b) (111)-oriented single crystal substrate.

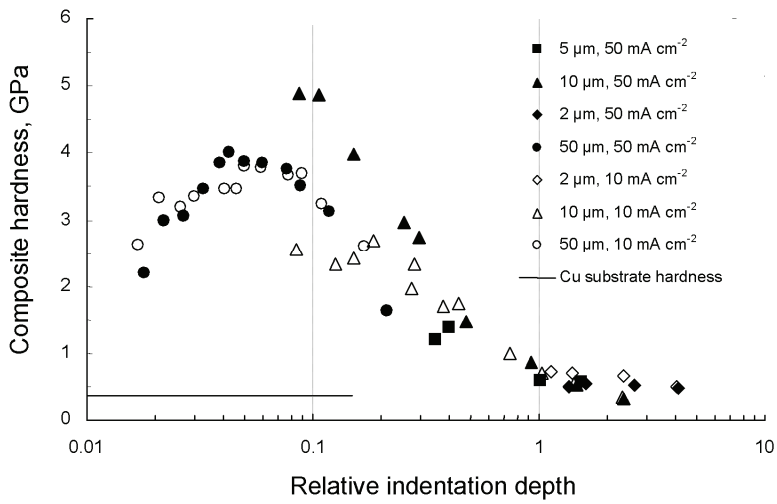

Fig. 5. Variation of the composite hardness, H_C, with the relative indentation depth, *h*/*t*, for electrodeposited Ni films on a Cu substrate. Film thickness and deposition current densities are given in the diagram. The thick line represents the hardness of the Cu substrate (H_S = 0.37 GPa).

For shallow penetration depths ($h/t \leq 0.10$), it was found that the response was that of the film only. The hardness of the film then increased until a certain relative indentation depth (< 0.1). The films obtained with the higher current density (50 mA·cm^{-2}) appeared harder than those deposited with 10 mA cm^{-2}. As the relative indentation depths increased ($h/t > 0.10$), the composite hardness decreased until it attained the substrate hardness H_S, indicated by the solid line in Fig. 5.

The change in the composite hardness H_C, with indentation diagonal *d* on a cold-rolled Cu substrate is shown in Fig. 6. The experimental data for these systems were fitted with the composite hardness model of Korsunsky, Eq. (6). H_S was taken as 0.37 GPa, according to the experimentally obtained value.

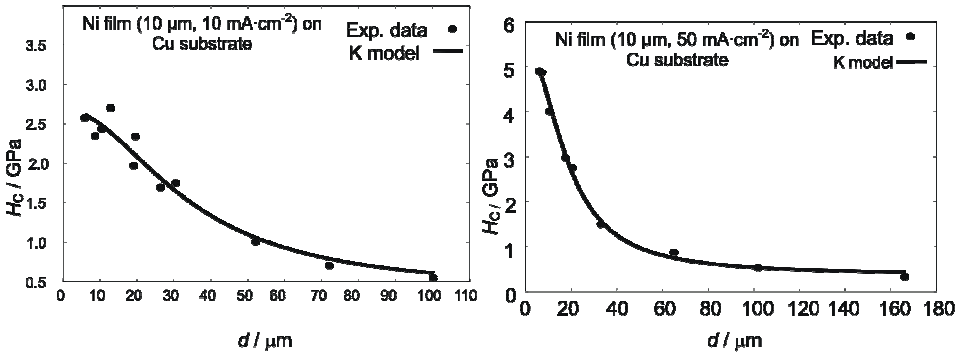

(a) (b)

Fig. 6. Experimental values of the composite hardness H_C as a function of the indent diagonal length, *d*, for two different Ni films on a cold-rolled Cu substrate. The films had the same thickness of 10 μm but were obtained with two differrent current densities: a) 10 and b) 50 mA cm^{-2}. Theoretical description (lines), according to the Korsunsky hardness composite model is given in the diagram.

This model provides a good fit of the experimental data. The indentation tests over the chosen sample covered a large enough range to describe adequately the change in the behavior from near-substrate to film only. In curve-fit data produced from the model validation process for two electrodeposited films are given in Table I.

TABLE I. Values of the fitting results according to the Korsunsky (K) model for the nickel film of 10 μm thickness on a cold-rolled Cu substrate

Quantity	K model	Asymptotic standard error
Electrodeposited Ni film (10 μm, 10 mA cm^{-2}) on Cu substrate		
H_F / GPa	2.68	±0.11 (4.1%)
k’	0.0087	±0.0017 (20 %)
Electrodeposited Ni film (10 μm, 50 mA cm^{-2}) on Cu substrate		
H_F / GPa	5.4	±0.12 (4.1%)
k’	0.029	±0.002 (8.2 %)

According to the C–L model, Eq. (3), it is possible to calculate the hardness of the film only from the microhardness testing results (*i.e.*, the diagonal of the indent). For this system, it is valid that the limit of the substrate influence corresponds to $t/d = 1$.[1,2] Due to this, the model is applicable to film thickness of up to 10 μm for such a particular case. The dependence of the film hardness, H_F, calculated according to the C–L model on the relative indentation depth, h/t, for different film thickness *t*, different applied loads and different current densities is given in Fig. 7.

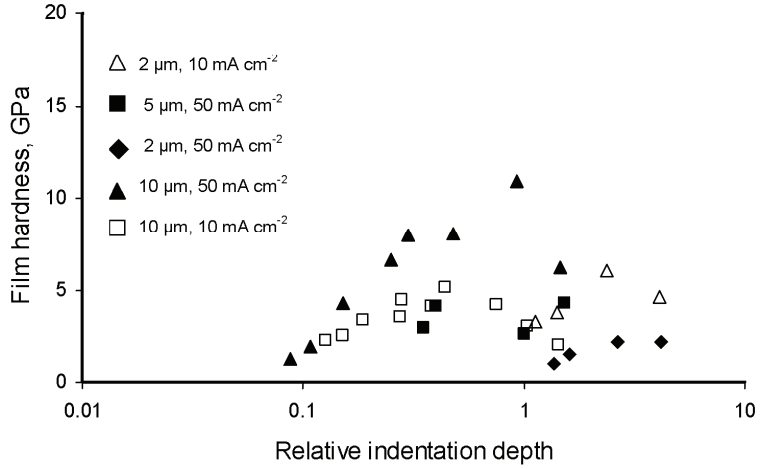

Fig. 7. Calculated film hardness according to the Chicot–Lesage composite hardness model for electrodeposited Ni films of different thicknesses on a Cu substrate. Films of different thicknesses were electrodeposited with two current densities (10 or 50 mA cm^{-2}) as indicated in the diagrams.

Soft film on a hard substrate. The change of the composite hardness, H_C, with relative indentation depth, h/t, for Ni films of different thicknesses (2–50 μm) on Si(111) substrates and two values of the current density (10 and 50 mA cm^{-2}) is shown in Fig. 8.

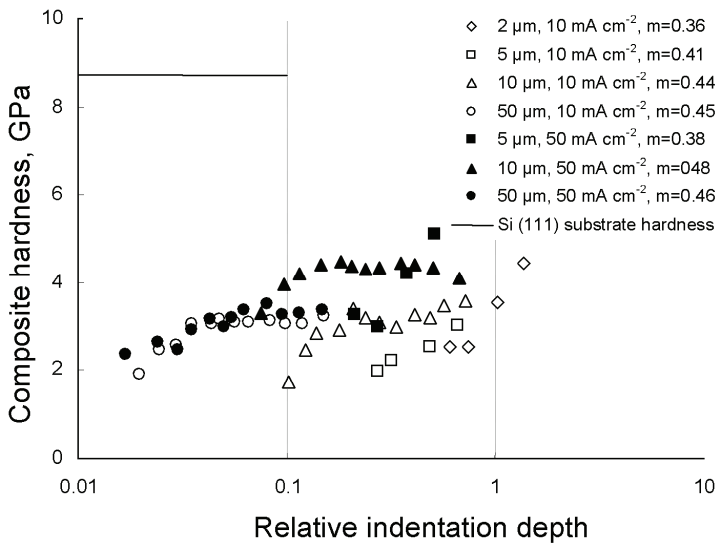

Fig. 8. Variation of composite hardness, H_C, with relative indentation depth, h/t, for electrodeposited Ni films on a (111)-oriented Si substrate. The solid line indicates the hardness of the Si(111) substrate.

It is found that for shallow penetration depths, ($h/t \leq 0.10$), the response was that of the film only. The hardness of the film the increased until a certain relative indentation depth (< 0.10). Films obtained with the higher current density (50 mA cm^{-2}) appear harder than those deposited with 10 mA cm^{-2}.

The change in the composite hardness H_C with indentation diagonal d, for Ni films of 10 μm thickness electrochemically deposited with 10 mA cm^{-2} current density on a single crystal Si(111) substrate is shown in Fig. 9. This is the case of a soft coating on a hard substrate. The experimental data for this system was fitted with the composite hardness models of Korsunsky (K-model) and Chicot–Lesage (C–L model). H_S was taken as 8.71 GPa, which is the experimentally determined value for a Si(111) oriented substrate.

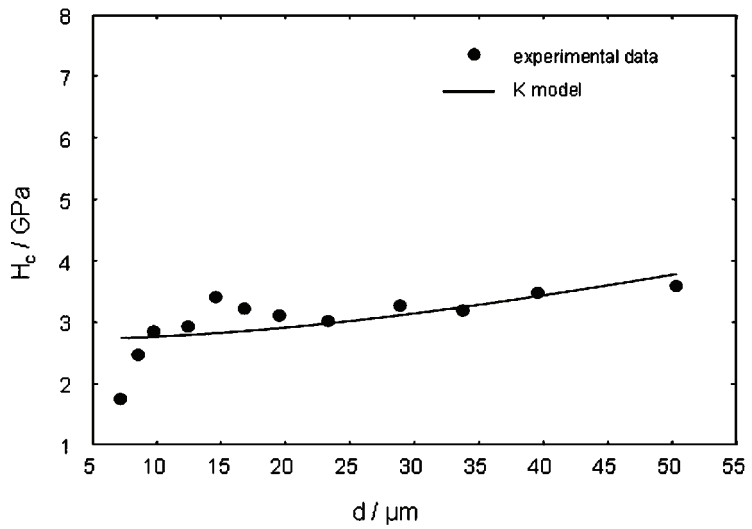

Fig. 9. Experimental values of the composite hardness, H_C, as a function of the indent diagonal length, d, for a 10 μm-thick Ni film on a Si(111) substrate. The film was obtained with a current density of 10 mA cm^{-2}. The theoretical description (lines) according to the Korsunsky composite hardness model is indicated in the diagram.

The curve-fit data produced from the K-model validation process for the two electrodeposited films are given in Table II. The standard fitting error given in the same Table indicates that the model does not fit the experimental data for this composite system of a soft coating on a hard substrate well.

TABLE II. Values of the fitting parameters involved in the Korsunsky (K) model for the nickel film of 10 μm thickness on a (111)-oriented Si substrate

Quantity	K model	Asymptotic standard error, %
H_F / GPa	2.71	6.27
k'	0.0008	43.1

The Chicot–Lesage model (C–L) based on the model for reinforced composites can be applied to experimental data even for the thick coatings (50 μm).[1,2] This model (Eq. (3)) applied to nickel film of different thicknesses, as indicated on the graph, is shown in Fig. 10. The films were obtained with two current densities.

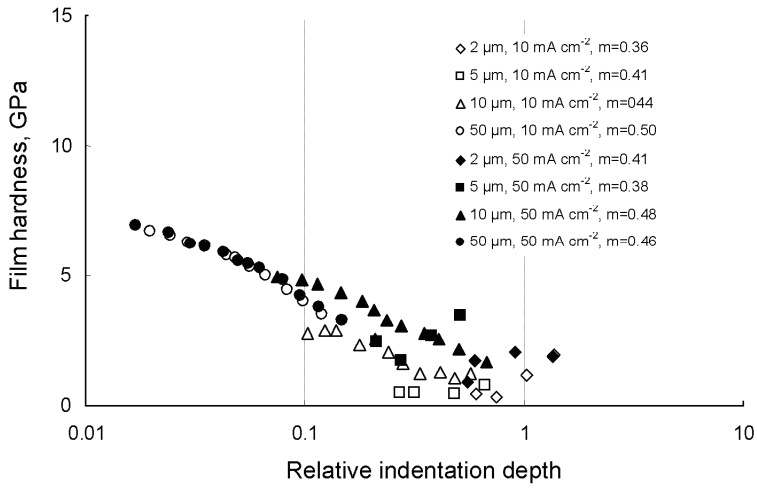

Fig. 10. Variations of the film hardness, H_F, with relative indentation depth, h/t, for the system which consisted of an electrodeposited Ni film on a Si (111) substrate according to the Chicot-Lesage composite hardness model.

As can be seen from Figs. 7 and 10, the values obtained for the film hardness, H_F, were not constant but influenced by the applied load, thickness of the film and current density. The variations should be related to physical phenomena, such as the indentation size effect, cracking in the neighborhood of the indent, the elastic contribution of the substrate for the lowest loads, or the crushing of the film for the highest loads.[1,2]

Comparison and analysis of the parameter $(t/d)^m$

The Meyer index or work hardening exponent, n^*, describes the variation of hardness with load. The model of Chicot–Lesage gives the parameter m, which is called the composite Meyer index.[1] The composite Meyer index characterizes the manner in which the composite hardness varies with load. Table III shows that the composite Meyer index depended on the composite structure (especially on the substrate type) and had a higher value for the composite Ni film–Cu substrate than for the Ni film–Si(111) composite system.

Figure 11 shows that $(t/d)^m$ is a parameter that can express the difference in tendency of the composite hardness with the indentation load for different composite systems.[7] For the low loads, the composite hardness tends to that of the

film, and parameter $(t/d)^m$ is independent of the substrate type. With increasing load, the influence of the substrate becomes dominant and parameter $(t/d)^m$ depends mostly on the substrate type. It can be seen that increasing the film thickness above a critical thickness (for these systems, this is 50 μm), leads to insensitivity of this parameter on the substrate type.

TABLE III. Comparison of the composite Meyer index, *m*, calculated according to the Chicot and Lesage model for different substrates and electrodeposited Ni films obtained with different current densities and with different thicknesses. Ni layer thickness and deposition current density are indicated for every particular layer

Ni films on Cu substrate j / mA cm^{-2}, d / μm	m	Ni films on Si(111) substrate j / mA cm^{-2}, d / μm	m
10, 2	0.58	10, 2	0.36
10, 10	0.61	10, 10	0.44
10, 50	0.49	10, 50	0.45
50, 2	0.51	50, 2	0.41
50, 5	0.71	50, 5	0.38
50, 10	0.86	50, 10	0.48
50, 50	0.50	50, 50	0.46

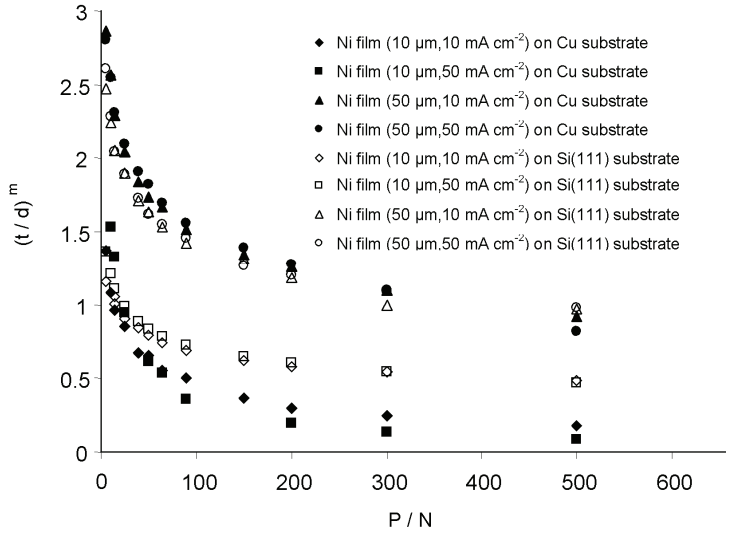

Fig. 11. Comparison of the parameter $(t/d)^m$ with the indentation load, *P*, for electrodeposited Ni films on a cold-rolled Cu substrate and a single crystal Si(111) substrate. The Ni films, grown with current densities of 10 and 50 mA cm^{-2}, of different thicknesses of 10 and 50 μm.

Hardness and yield strength of fine-grained nickel

The mode of deformation under the indenter described by Tabor follows the results of the slip line field theory for a rigid-plastic material.[10] In this case, it was found that the hardness is related to the yield strength, *Y*, by:

$$H/Y = 3 \quad (9)$$

It was found that the samples deposited with a current density above 10 mA cm^{-2} obeyed the Hall–Petch relationship. The Hall–Petch plot of yield strength *vs*. grain size for nickel is shown in Fig. 12 from three studies with an experimental procedure similar to that employed in this study (the different symbols indicate different studies).[11]

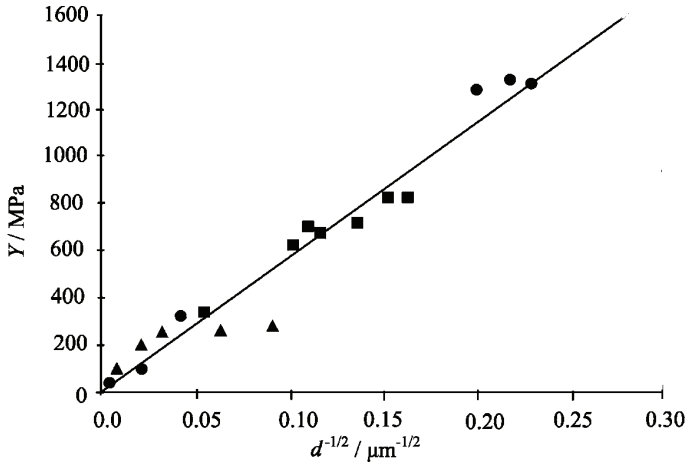

Fig. 12. Yield strength *vs*. grain size for nickel.

With the results of the film hardness fitted according to the Korsunsky model (Tables I and II), the values of the yield strength were calculated. For the 10-μm Ni films on Cu and (111) Si substrates deposited with a current density of 10 mA cm^{-2}, the yield strengths were 0.893 and 0.903 GPa, respectively (the film microstructure is shown in Figs. 2 and 3). These values of yield strength belong to nanocrystalline nickel with an average grain size of ≈ 30 nm.[11]

CONCLUSIONS

In order to analyze the hardness of different composite systems, nickel films were electrodeposited on a soft substrate of polycrystalline cold-rolled copper and a hard substrate of single crystal silicon with (111) orientation.

A microstructure of columnar grains, called colonies, with a grain size of the order of 0.5–3 μm was observed.

It was shown that the tendency of the composite hardness primary depends on the type of the composite system, *i.e.*, the differences in the mechanical properties of the film and substrate: the hardness of the substrate, the hardness of the film, their relative difference and, especially, the thickness of the film.

A nickel film on a Cu substrate represents a composite system of a hard film on a soft substrate. The Korsunsky and Chicot–Lesage composite models were

applied to the experimental data for films of up to 10 μm thickness. The Korsunsky model gave a good fit of the results for this type of system. The quality of the fits relied on obtaining experimental hardness data over a wide range of h/t values and almost always this will have to include nano-indentation data. The C–L model was also applicable to this system but there is a necessity for more experiments to be performed and the results of the application verified for this composite system.

Nickel films on a Si(111) substrate can be considered as a soft film on a hard substrate. Korsunsky composite hardness model (K-model) did not fit the experimental data for this composite system well. The Chicot–Lesage model (C–L model), based on the model for reinforced composites, can be applied to the experimental data, even for thick coatings (50 μm). The Chicot–Lesage model was chosen for the system Ni film–Si substrate for all specimens and the film hardness was calculated for each indentation diagonal.

The values obtained for the film hardness, H_F, were influenced by the applied load. In case of the Ni film on Cu substrate system, the film hardness lines exhibited a change of slope, but in case of the Ni film on Si substrate system, the film hardness lines had a descending character. According to Chicot and Lesage explanation, the variations should be related to physical phenomena, such as the indentation size effect, cracking in the neighborhood of the indent, the elastic contribution of the substrate for the lowest loads or the crushing of the film for the highest loads.

The composite Meyer index, m, characterizes the way in which the composite hardness varies with load. When the composite hardness tends to that of the film (for low loads), the parameter $(t/d)^m$ is almost independent of the substrate type. With increasing load, the influence of the substrate became dominant and the parameter $(t/d)^m$ depended mostly on the type of substrate. In addition, with increasing thickness of the film, the influence of the substrate increased for both composite systems. There are not sufficient experimental results concerning the parameter $(t/d)^m$ yet, but it is thought that it deserves more attention in hardness investigations of composite system.

Acknowledgments. This work was performed within the frame of the projects “Micro and Nanosystems Technologies, Structures and Sensors” and “Designing of nanocrystalline magnetic materials of (Nd, Pr)FeB type and smart magnetic materials components”, supported by grants from the Ministry of Science and Technological Development of the Republic of Serbia, Grant No. TR-6151 B and 142035 B, respectively.

ИЗВОД

МИКРОМЕХАНИЧКА И СТРУКТУРНА СВОЈСТВА ЕЛЕКТРОДЕПОНОВАНИХ ПРЕВЛАКА НИКЛА НА РАЗЛИЧИТИМ СУПСТРАТИМА

ЈЕЛЕНА ЛАМОВЕЦ[1], ВЕСНА ЈОВИЋ[1], РАДОСЛАВ АЛЕКСИЋ[2] и ВЕСНА РАДОЈЕВИЋ[2]

[1]*Институт за хемију, технологију и металургију – Центар за микроелектронске технологије и монокристале, Његошева 12, Београд и* [2]*Технолошко–металуршки факултет, Карнегијева 4, Београд*

Ситнозрне превлаке никла су електродепоноване из сулфаматног купатила на различитим супстратима: хладно-ваљаном поликристалном бакру и монокристалном силицијуму (111) оријентације. Утицај супстрата и одабраних параметара електродепозиције на механичка и структурна својства ових композитних структура испитиван је тестовима микротврдоће по Vickers-у при различитим оптерећењима. Изнад критичне дубине утискивања, измерена вредност тврдоће није тврдоћа електродепонованог филма, већ такозвана «композитна микротврдоћа», јер супстрат учествује у пластичној деформацији током процеса утискивања. Одабрана су два модела композитне тврдоће базирана на различитим принципима (модел Chicot–Lesage и Korsunsky) и примењена на експерименталне резултате у циљу израчунавања тврдоће филма. Вредности микротврдоће електродепонованих превлака никла зависе од вредности густине струје. Повећање густине струје води смањењу величине зрна и повећању вредности микротврдоће.

(Примљено 23. децембра 2008, ревидирано 14. априла 2009)

REFERENCES

1. J. Lesage, D. Chicot, *Surf. Coat. Technol*. **200** (2005) 886
2. J. Lesage, A. Pertuz, E. S. Puchi-Cabrera, D. Chicot, *Thin Solid Films* **497** (2006) 232
3. W. D. Callister Jr., *Fundamentals of Materials Science and Engineering, An interactive E-text*, 5th ed., Wiley, New York, 2001, p. S-166
4. A. M. Korsunsky, M. R. McGurk, S. J. Bull, T. F. Page, *Surf. Coat. Technol*. **99** (1998) 171
5. J. R. Tuck, A. M. Korsunsky, D. G. Bhat, S. J. Bull, *Surf. Coat. Technol*. **137** (2001) 217
6. S. W. Banovic, K. Barmak, A. R. Marder, *J. Mater. Sci*. **33** (1998) 639
7. J. Lamovec, V. Jović, D. Randjelović, R. Aleksić, V. Radojević, *Thin Solid Films* **516** (2008) 8646
8. M. Tanaka, K. Higashida, H. Nakashima, H. Takagi and M. Fujiwara, *Int. J. Fract.* **139** (2006) 383
9. H. Li, R. C. Bradt, *Mater. Sci. Eng. A* **142** (1991) 51
10. D. Tabor, *The Hardness of Metals*, Clarendon, London, 1951, p. 107
11. J. Guidry, *M.Sc. Thesis*, Lousiana State University, Baton Rouge, LA, 2002, p. 14.

Journal of the Serbian Chemical Society
JSCS@tmf.bg.ac.rs • www.shd.org.rs/JSCS

J. Serb. Chem. Soc. 74 (7) 833–843 (2009)
JSCS–3880

UDC 666.32+66–96+577.112.386:549.25/.28+66.081
Original scientific paper

Sorption performance of cysteine-modified bentonite in heavy metals uptake

HOSSEIN FAGHIHIAN* and MASSOUD NEJATI-YAZDINEJAD

Department of Chemistry, University of Isfahan, Isfahan 81746-73441, I. R. Iran

(Received 27 December 2008, revised 12 March 2009)

Abstract: A local clay, bentonite (N-Ben), was modified by the biologically--based ligand, cysteine (Cys), through a simple sorption technique. The modified sorbent (Cys–Ben) demonstrated affinity for soft and moderately soft heavy metal ions (HMI), such as Cd(II) and Pb(II), probably as a result of the soft basic character of the thiol ligand side chains. The resulting modified system was effective for metal binding with capacities of 0.503 and 0.525 mmol g^{-1}, for Pb(II) and Cd(II), respectively. Comparative batch experiments were performed for removing lead and cadmium from aqueous solutions. The sorption parameters were derived from a Langmuir fit to the sorption isotherms of the studied ions. The study showed that the sorption capacity of Cys–Ben was higher than that of N-Ben for these ions. The effect of pH was examined over the range 2.0–6.0. The sorption capacities of Cys–Ben showed that this modified clay is a good sorbent for the examined heavy metal ions.

Keywords: bentonite; modification; sorption; cysteine; heavy metal ions.

INTRODUCTION

Contamination of soil and groundwater with toxic metals at trace levels is a complex and common problem, and it is well known that heavy metal pollution is a serious threat to the environment. Pb, Cd, Cu, Hg, Cr, Ni and Zn are the main trace elements that are of greatest concern. Although many heavy metals are necessary in small amounts for the normal development of the biological cycle, most of them become toxic at high concentrations. Many studies were devoted to their elimination, the objective being to develop an effective and economic process for their removal. The methods for the removal of heavy metals cited in the literature generally involve sorption processes, ion exchange mechanism, or complexation by natural and synthetic reagents. Among the different adsorptive materials that have been used for the capture metal ions from solutions are activated carbon, zeolites and clays.[1–4]

* Corresponding author. E-mail: h.faghih@sci.ui.ac.ir
doi: 10.2298/JSC0907833F

Effective sorbents with a strong affinity and, consequently, a high loading capacity for the targeted metal ions were prepared by modifying the surface of silica gel, zeolites and clays.[5–7] Due to their high specific surface areas, low cost and ubiquitous presence in most soils, clays are usually chosen for the prevention of the release of heavy metals into the environment. One such clay is bentonite, which is a 2:1 type of clay, and its unit layer structure consists of one Al^{3+} octahedral sheet placed between two Si^{4+} tetrahedral sheets. The isomorphous substitution of Al^{3+} for Si^{4+} in the tetrahedral layer and Mg^{2+} or Zn^{2+} for Al^{3+} in the octahedral layer results in a net negative surface charge on the clay, which give ion exchange property to it.[8]

Modification may be required to make clay minerals possessing specific sorption and catalytic properties. One of these modification processes is the interaction of the clay mineral with various organic cations and molecules under defined conditions. These modifications are caused by chemical and thermal activation,[9] pillaring with inorganic cations[10] and surfactant insertion in the interlayer space of the clay.[11,12] The association of the clay with complexing reagents (polyphosphate, mercaptobenzothiazole) is a research field which opens interesting perspectives for selectivity of the removal of heavy metals.[13] These organic compound can bind to the surface and/or penetrate into the interlayer space of clay minerals as a ligand.[14–16] One group of these ligands can be amino acids.[17]

The concerns of this investigation are divided into two parts: first, the preparation and characterization of modified bentonite and second, an investigation of sorption due to the specific affinity of the thiol group of Cys for the two environmentally important divalent cations Pb(II) and Cd(II) and to examine the practical usability of these modified sorbent in the sorption of these heavy metals from aqueous media. The adsorption features of the studied sorbent were evaluated on the base of sorption parameters derived from the compatibility of the sorption isotherms to the Langmuir model.

EXPERIMENTAL

Materials and methods

Bentonite sorbent was obtained from deposits of the Semnan Region, Iran. The sample was ground in a ball mill and only particles smaller than 71 μm (200 mesh) were used for the sorption experiments. The employed L-cysteine (Merck) had a purity of > 99 %. All the compounds used to prepare the reagent solutions were of analytic reagent grade. The stock solutions of Cd(II) and Pb(II) (1000 mg L^{-1} for each ion) were prepared by dissolving a weighed quantity of the respective nitrate salt in distilled water.

Chemical analysis was performed by X-ray fluorescence (XRF) spectroscopy using a Bruker S4 PIONEER spectrometer. X-Ray powder diffraction (XRD) patterns were collected on a Bruker D8 Advance X-ray diffractometer (CuK_{α}). The specific surface area was determined by the BET method, using a Monosorb surface area analyzer. The IR spectra were recorded in air at room temperature on a Shimadzu infrared spectrophotometer (IR-435). The spectra were measured in KBr pellets. The chemical, mineralogical and physico–chemical charac-

teristics of the natural sample are summarized in Table I. The cations in solution were analyzed by a Shimadzu atomic absorption spectrophotometer (AA-670).

TABLE I. Physico–chemical, chemical and mineralogical characteristics of the natural sorbent

Specific surface area, $m^2\ g^{-1}$	34.6
CEC / meq g^{-1}	0.76
Chemical composition, mass %	
SiO_2	60.33
Al_2O_3	15.63
Fe_2O_3	2.54
CaO	2.86
K_2O	2.52
MgO	1.44
Na_2O	1.60
TiO_2	0.43
MnO	0.11
SrO	0.08
Loss on ignition	12.51
Mineralogical composition, mass %	
Montmorillonite	52.2
Quartz	25.4
Feldspar	9.6
Mordenite	6.4
Calcite	4.8
Gypsum	1.5

Preparation of modified bentonite

Natural bentonite (5.0 g) was suspended in a 100 mM solution of cysteine, the pH of which had previously been adjusted to 4.0 with HNO_3 or NaOH. The obtained suspension was stirred at room temperature for 12 h. The solid phase (Cys–Ben) was separated by centrifugation, washed with distilled water and then dried at room temperature and stored for subsequent studies. The modified bentonite was designated as Cys–Ben.[18]

Sorption experiments

A solution of metal nitrate (100 mL) with a concentration in the range 0.10–10.0 mmol dm^{-3} was placed in a polyethylene bottle. The pH of the solution was adjusted to the desired value using HNO_3 or NaOH solution. An accurately weighed amount of N-Ben or Cys–Ben (1.0 g) was then added to the solution. A series of such bottles was then agitated at a constant speed in a shaking water bath, the temperature of which was kept constant at 25 °C. After a contact time of 12 h (the equilibrium time determined by preliminary experiments), the solid phase was separated by centrifugation. The progress of the sorption was assessed by determining the concentration of metal ion remaining in an aliquot by AAS. All experiments were performed in duplicate.

RESULTS AND DISCUSSION

Sorbent characterization

The XRD pattern of bentonite is shown in Fig. 1, which indicates that the raw bentonite consisted of montmorillonite and quartz.

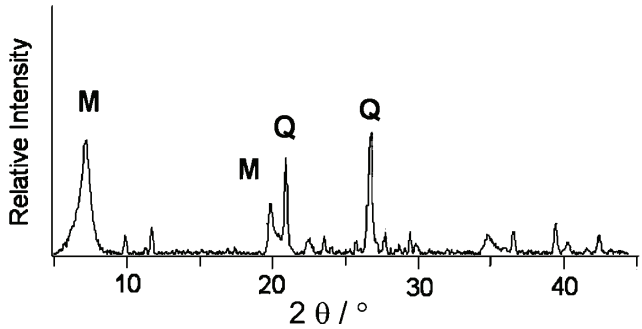

Fig. 1. XRD Pattern of bentonite (M = montmorillonite, Q = quartz).

According to the literature, the sorption of an organic material onto a negatively charged surface is a complex process involving both cation exchange and hydrophobic bonding.[19]

The modification of the sorbent material after treatment with the cysteine solution was verified by the IR spectra of the materials, which are shown in Fig. 2. The wavenumbers and vibration type of bentonite are given in Table II. The Cys–Ben spectrum is dominated by the bands of the host material but the presence of the amino acid (on the surface or between the layers) is also observed. Nevertheless, a closer inspection of the 1700–1300 cm^{-1} of the Cys–Ben and comparison with the same wavenumber interval of the amino acid and that of the host material revealed that the guest species were adsorbed by the sample.

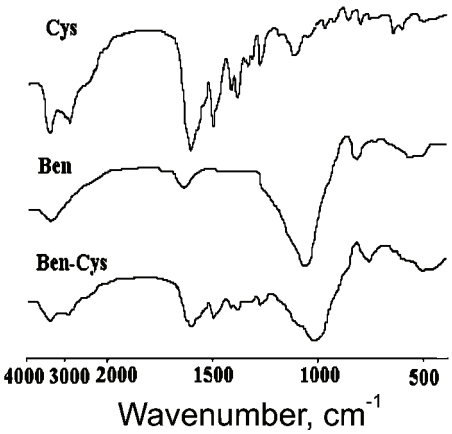

Fig. 2. IR Spectra of bentonite, cysteine and Cys–Ben.

TABLE II. IR vibrations of bentonite

Wavenumber, cm^{-1}	Vibration type
≈ 3600	O–H stretching (Si,Al)–OH
≈ 3400	O–H stretching H–OH
≈ 1650	H–O–H deformation
≈ 1150	Si–O stretching
≈ 1050	Si–O–Si stretching
≈ 520	Si–O–Si deformation

In relation to the interaction between bentonite and cysteine, the peaks at 3500–2500 cm^{-1} are probably N–SH stretching vibration. The broad O–H band (≈ 3500 cm^{-1}) belonging to the carboxyl in the structure is invisible because it is masked by the O–H stretching of the amino acid and water in the bentonite. The spectrum of Cys–Ben showed that the bands at 1340 (symmetric deformation of the NH_3 group), 1520 (deformation of the N–H group), 1740 (stretching of C=O), 680 (stretching of C–S) and 2560 cm^{-1} (stretching of S–H) decreased in intensity.[20,21] All these results may be caused by the interaction between bentonite and the NH_2 group of cysteine.

The TG/DTG curves of bentonite, cysteine and Cys–Ben are shown in Figs. 3 and 4. The bentonite showed a weight loss between 25–200 °C, corresponding to the desorption of internal and external water of hydration.[22] Between 200 and 550 °C, the bentonite did not undergo any thermally induced changes. Therefore, the peaks in this region for the organo–bentonite are attributable to the decomposition of the amino acid. The observed weight losses above 450 °C are attributable to dehydroxylation.[23]

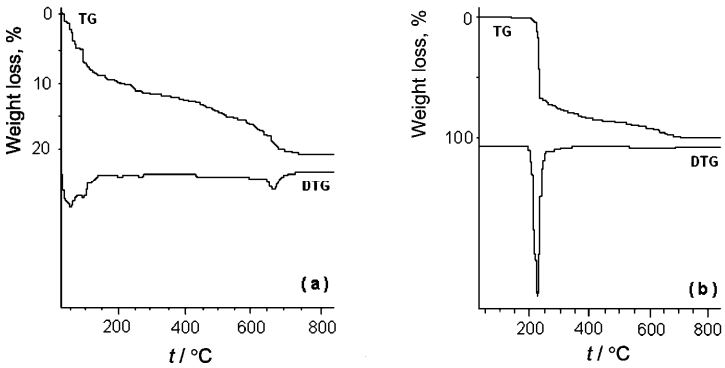

Fig. 3. TG and DTG curve of a) bentonite and b) cysteine.

Effect of pH

The effect of pH was studied at a constant metal ion concentration (7.0 mmol dm^{-3}) and solid ratio (100 ml g^{-1}) at 25 °C. The pH is an important pa-

rameter for the sorption of metal ions from aqueous solutions because it affects the solubility of the metal ions, the concentration of the counter ions on the functional groups of the sorbent and the degree of ionization of the sorbate during the reaction. The sorptions of Cd(II) and Pb(II) onto Cys–Ben and N-Ben as a function of pH are shown in Fig. 5. Cd(II) and Pb(II) were adsorbed on these sorbents over the pH range 2.0–5.5. It can be seen that the sorption of Cd(II) and Pb(II) is markedly pH-dependent. It is obvious that the amount of the metal ions adsorbed on the solid phase (q) was low at low pH values for both metal ions. This can be explained by the competition of protons for sites on the sorbents. In aqueous solutions, sorbents (bentonite and/or Cys–Ben) with charged groups are susceptible to the experimental conditions such as pH. This usually causes noticeable changes in the sorption of ions onto charged solid sorbents. As the pH of the aqueous phase was lowered (pH < 4), the surface usually become less negative because of protonation of the charged sites. This leads to a decrease in the sorption of cations depending on the sign of the surface charge. The reverse is

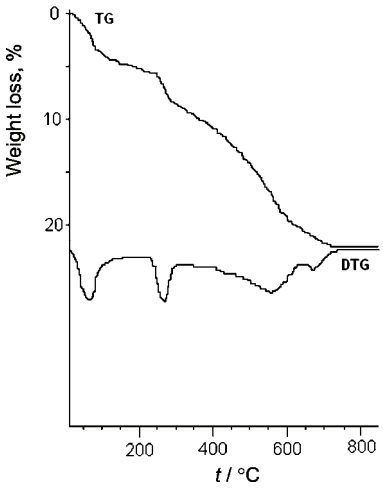

Fig. 4. TG and DTG curve of Cys–Ben.

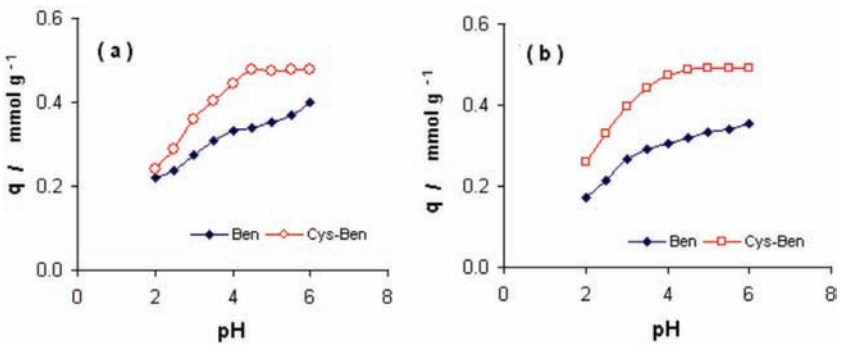

Fig. 5. Effect of pH on the sorption of a) Pb(II) and b) Cd(II) by the two sorbents. c_i = 7.0 mmol dm^{-3}; contact time: 12 h, at 25 °C.

true when the pH of the aqueous solution is increased (pH > 4). The value of q increased with increasing initial pH value for both lead and cadmium ions, with a more profound effect in the case of lead ions. It is apparent that using solutions with an initial pH of 4–5 gave the highest q values.

Effect of contact time

The effect of contact time was studied at a constant metal ion concentration (1.0 mmol dm^{-3}) and a liquid to solid ratio (100 ml g^{-1}) at 25 °C. The obtained results are shown in Fig. 6. It can be seen that the amount of Pb(II) and Cd(II) adsorbed per unit mass of adsorbent (q) showed increased with interaction time. The rate of uptake of Pb(II)/Cd(II) was maximal during the first 12 h, after which it leveled off and equilibrium was attained after 24 h. Maximum metal ion removal values were observed at this contact time.

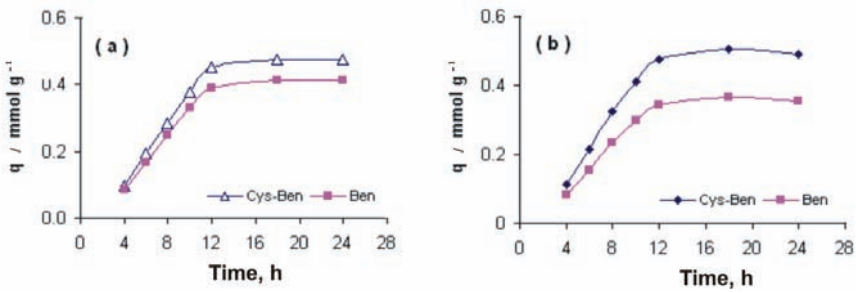

Fig. 6. Effect of contact time on the sorption of a) Pb(II) and b) Cd(II) by the two sorbents. c_i = 7.0 mmol dm^{-3}, pH 4.0, at 25 °C.

Effect of temperature and thermodynamic parameters

When the adsorption equilibrium of the studied systems was established, the metal cation adsorbed was in equilibrium with the residual metal cation remaining in the liquid phase. The values of equilibrium constant (K_d) of the sorption process at different temperatures were calculated from the relation:[24]

$$K_d = \frac{q_e}{c_e}\frac{m}{V} \tag{1}$$

where q_e is the equilibrium amount of the metal ions adsorbed on the solid phase, c_e is the concentration of the metal ions remaining in solution at equilibrium, m is the mass of the sorbent and V is the volume of the solution. The standard Gibbs free energy ($\Delta G^{\ominus}$) was calculated from the relation:[25]

$$\Delta G^{\ominus} = -RT\ln K_d \tag{2}$$

The values of the entropy ($\Delta S^{\ominus}$) and enthalpy ($\Delta H^{\ominus}$) changes of the sorption process were calculated by plotting of ln K_d *vs.* 1/T according to the van't Hoff equation:

$$\ln K_d = (1/R)(\Delta S^{\ominus} + \Delta H^{\ominus}/T) \quad (3)$$

The values obtained for K_d, $\Delta S^{\ominus}$, $\Delta H^{\ominus}$ and $\Delta G^{\ominus}$ are given in Table III. The value of K_d decreased with temperature for both metal ions. The Gibbs free energy change is the driving force and the fundamental criterion of spontaneity. The obtained values of $\Delta G^{\ominus}$ were –3.64 and –2.12 kJ mol^{-1} at 25 °C for Cd(II) and Pb(II), respectively. The negative values of $\Delta G^{\ominus}$ imply that the sorption of these metal ions on the organo–bentonite is spontaneous and becomes more favorable with decreasing temperature. It was reported that $\Delta G^{\ominus}$ values down to –25 kJ mol^{-1} are consistent with electrostatic interaction between sorption sites and the metal ions.[26,27]

TABLE III. Values of the thermodynamic parameters for the sorption of the studied metal ions

Sorbent	HMI	T / K	ln K_d	$\Delta H^{\ominus}$ / J mol^{-1}	$\Delta S^{\ominus}$ / J mol^{-1} K^{-1}	$\Delta G^{\ominus}$ / kJ mol^{-1}
Cys–Ben	Cd(II)	298	1.477	–5.97	–7.81	–3.64
		303	1.427			–3.60
		313	1.356			–3.52
		323	1.277			–3.44
		333	1.224			–3.37
	Pb(II)	298	0.859	–2.27	–0.490	–2.12
		303	0.837			–2.12
		313	0.817			–2.12
		323	0.788			–2.11
		333	0.759			–2.11
N-Ben	Cd(II)	298	0.033	10.7	35.9	–0.020
		303	0.046			–0.16
		313	0.178			–0.52
		323	0.301			–0.87
		333	0.484			–1.23
	Pb(II)	298	0.367	0.370	4.30	–0.91
		303	0.372			–0.93
		313	0.375			–0.97
		323	0.381			–1.01
		333	0.383			–1.06

The obtained values of $\Delta S^{\ominus}$ were –7.81 and –2.12 J mol^{-1} K^{-1} for Cd(II) and Pb(II), respectively. The negative values of $\Delta S^{\ominus}$ for both metal ions indicate the decrease in randomness as a consequence of sorption.[28] The values of $\Delta H^{\ominus}$ were –5.97 and –2.27 kJ mol^{-1} for Cd(II) and Pb(II), respectively. These results show that the sorption of these ions by modified bentonite is an exothermic process.

Sorption isotherms

The sorption isotherms can be described by a Langmuir-type isotherm, which is described by the following equation:

$$q_e = \frac{Kq^0 c_e}{1 + Kc_e} \tag{4}$$

where q^0 is the maximum capacity of the sorbent and K is the Langmuir constant, related to the energy of sorption. The Langmuir equation can be rearranged to a linear form for the convenience of plotting and determining the Langmuir constants as follows:

$$\frac{c_e}{q_e} = \frac{c_e}{q^0} + \frac{1}{Kq^0} \tag{5}$$

The sorption of Cd(II) and Pb(II) from solution by N-bentonite and Cys–Ben was studied at room temperature at pH 4.0. The sorption isotherms for Cd(II) and Pb(II) were established to compare the sorption capacity of Cys–Ben with that of N-bentonite (Fig. 7).

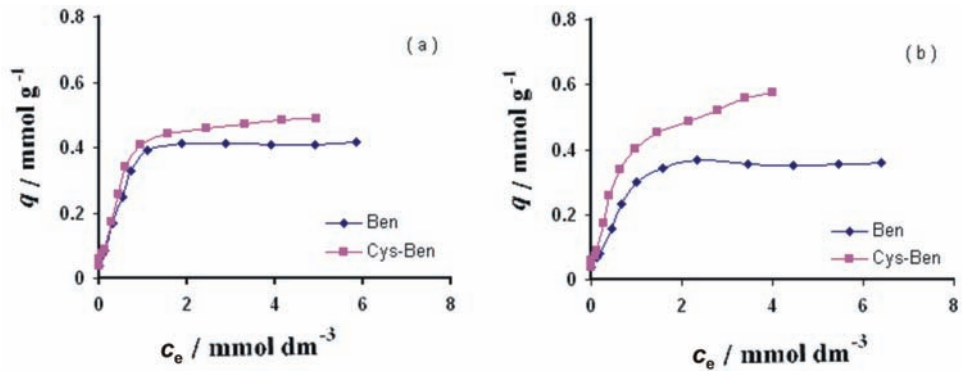

Fig. 7. Sorption isotherms of a) Pb(II) and b) Cd(II) at pH 4.0,; contact time: 12 h, at 25 °C.

The equilibrium sorption data were fitted to the linear form of the Langmuir equation, and the determined sorption parameters (q^0, K and r^2) are given in Table IV. In all cases, the degree of fit, r^2, for the linear regression fits were found to be > 0.99, which is a measure of the goodness-of-fit of the experimental data to the Langmuir isotherm model. For both Cd and Pb, higher K values were observed for Cys–Ben than for N-bentonite. The values of q^0 and K were calculated from the intercept and slope of the linear plots, respectively.

TABLE IV. Lamgmuir parameters for the sorption of the studied metal ions

Solute	Sorbent	K / dm^3 mmol^{-1}	q^0 / mmol g^{-1}	r^2
Pb(II)	N-Ben	3.91	0.436	0.9928
	Cys–Ben	10.3	0.503	0.9917
Cd(II)	N-Ben	3.07	0.381	0.9905
	Cys–Ben	5.08	0.525	0.9911

The values of q^0 (0.503 and 0.525 mmol g^{-1} for Pb(II) and Cd(II, respectively) are consistent with the experimentally obtained values (Table IV). The values of the Langmuir binding constant (K) were 10.3 and 5.08 dm^3 $mmol^{-1}$ for Pb(II) and Cd(II), respectively.

The sorption mechanism of Cys–Ben is complex and the proposed mechanism is probably composed of two successive steps:

– an ion exchange step, during which cadmium/lead ions in solution are exchanged with framework ions;

– a complexation step, in which the remaining cadmium/lead ions in the solution react with the Cys to form a cadmium/lead cysteine complex.[17]

Accordingly, the sorption process can be described as follows:

$$A^{n+} + n\text{M-Ben} \rightleftharpoons n\text{M}^{+} + \text{A-Ben} \quad (6)$$

where M refers to the exchangeable alkali metal ions (*i.e.* Na^+ and K^+) of the clay framework, A^{n+} represents heavy metal ions (Cd^{2+} or Pb^{2+}) and Ben refers to ion-exchange sites of bentonite.

CONCLUSIONS

Cysteine-modified bentonite (Cys–Ben) was prepared from N-bentonite. The structure and sorption performance of N-bentonite and Cys–Ben were evaluated. Using Cd(II) and Pb(II) as heavy metal indicators for sorption, the experiments proved that the sorption capacities of Cys–Ben were enhanced in comparison to N-bentonite. The pH is an important factor affecting the sorption of heavy metals by bentonite, and it can change the affinity of the sorption sites for heavy metals. The modified mineral had a higher removal efficiency for cadmium than for lead ions, regardless of the operating conditions. A high metal uptake can be achieved using an initial solution pH of 4–5 with a careful selection of the other conditions, especially the metal ion and slurry concentrations, to avoid masking of sorption by chemical precipitation. The Langmuir isotherm provides a good fit for the studied temperature and concentration ranges.

Acknowledgements. This study was completed at the University of Isfahan and supported by the Office of Graduate Studies. The authors are grateful to the Office for their support.

ИЗВОД

СОРПЦИОНЕ КАРАКТЕРИСТИКЕ БЕНТОНИТА МОДИФИКОВАНОГ ЦИСТЕИНОМ ПРИ УКЛАЊАЊУ ТЕШКИХ МЕТАЛА

HOSSEIN FAGHIHIAN и MASSOUD NEJATI-YAZDINEJAD

Department of Chemistry, University of Isfahan, Isfahan 81746-73441, I. R. Iran

Локална глина бентонит (N-Ben) модификована је биолошким лигандом цистеином (Cys) једноставном сорпционом техником. Модификовани сорбент (Cys–Ben) показао је афинитет према јонима меких и умерено меких тешких метала као што су Cd(II) и Pb(II), што је вероватно резултат умерено базног карактера периферних тиолних ланаца лиганда.

Резултујући модификовани систем био је ефикасан за везивање метала капацитетима од 0,503 и 0,525 mmol g^{-1} за Pb(II) и Cd(II), редом. Изведене су упоредне групе експеримената уклањања олова и кадмијума из водених раствора. Сорпциони параметри добијени су уз претпоставку да сорпција испитиваних јона одговара Langmuir-овој адсорпционој изотерми. Испитивање је показало да је сорпциони капацитет сорбента Cys–Ben за ове јоне већи у односу на капацитет сорбента N-Ben. Утицај pH испитиван је у опсегу 2,0–6,0. Добијени сорпциони капацитети показали су да је Cys–Ben добар сорбент за испитиване јоне тешких метала.

(Примљено 27. децембра 2008, ревидирано 12. марта 2009)

REFERENCES

1. A. M. Garcia, V. G. Serrano, M. F. Franco, C. V. Calahorro, *J. Hazard. Mater*. **103** (2003) 141
2. J. Perić, M. Trgo, N. Medvidović, *Water Res*. **38** (2004) 1893
3. T. Saitoh, F. Satoh, M. Hiraide, *Talanta* **61** (2003) 811
4. S. E. Bailey, T. J. Olin, R. M. Bricka, D. D. Adrian, *Water Res*. **33** (1999) 2469
5. H. H. Tran, F. A. Roddick, J. A. O'Donnell, *Water Res*. **33** (1999) 2992
6. C. F. Lin, S. S. Lo, H. Y. Lin, Y. Lee, *J. Hazard. Mater*. **60** (1998) 217
7. F. Barbier, G. Duc, M. P. Ramel, *Colloids Surf. A*. **166** (2000) 153
8. D. W. Breck, *Zeolite Molecular Sieves*, John Wiley Inc., New York, 1974
9. E. G. Pradas, M. V. Sanchez, F. C. Cruz, *J. Chem. Technol. Biotechnol*. **59** (1994) 289
10. W. Matthes, F. T. Madsen, G. Kahr, *Clays Clay Miner*. **47** (1999) 617
11. S. H. Lin, R. S. Juang, *J. Hazard. Mater*. **92** (2002) 315
12. A. A. Atia, *Appl. Clay Sci*. **41** (2008) 73
13. Y. I. Tarasevich, G. M. Klimova, *Appl. Clay Sci*. **19** (2001) 95
14. V. Balek, Z. Malek, U. Ehrlicher, K. Gyoryova, *Appl. Clay Sci*. **21** (2002) 295
15. F. Bergaya, G. Lagaly, *Appl. Clay Sci*. **19** (2001) 1
16. A. Parbhakar, J. Cuadros, M. A. Sephton, W. Dubbin, *Colloids Surf. A* **307** (2007) 142
17. L. G. Sillen, A. E. Martell, *Stability Constants of Metal-ion Complexes*, Chem. Soc., London, Alden, Oxford, 1971
18. H. Faghihian, M. Nejati-Yazdinejad, *Clay Miner*. **44** (2009) 125
19. Z. Li, R. S. Bowman, *Environ. Sci. Technol*. **31** (1997) 2407
20. A. Pawlukojc, J. Leciejewicz, A. J. Ramirez, *Spectrochim. Acta A* **61** (2005) 2474
21. L. O. B. Benetoli, C. M. D. Souza, D. A. M. Zaia, *Origins Life Evol. B*. **37** (2007) 479
22. H. He, Z. Ding, J. Zhu, *Clays Clay Miner*. **53** (2005) 287
23. W. Xie, Z. Gao, K. Liu, W. P. Pan, R. Vaia, *Thermochim. Acta* **368** (2001) 339
24. G. W. Beall, *Appl. Clay Sci*. **24** (2003) 11
25. A. Seker, T. Shahwan, A. E. Eroglu, S. Yilmaz, Z. Demirel, M. C. Dalay, *J. Hazard. Mater*. **154** (2008) 973
26. G. M. Haggerty, R. S. Bowman, *Environ. Sci. Technol*. **28** (1994) 452
27. K. Al-Dalama, B. Aravind, A. Stanislaus, *Appl. Catal. A* **296** (2005)49
28. S. I. Lyubchik, A. I. Lyubchik, O. L. Galushko, L. P. Tikhonova, J. Vital, I. M. Fonseca, S. B. Lyubchik, *Colloids Surf. A* **242** (2004) 151.

Journal of the Serbian Chemical Society
JSCS@tmf.bg.ac.rs • www.shd.org.rs/JSCS

J. Serb. Chem. Soc. 74 (7) 845 (2009)

Erratum (printed version only)

Issue No. 6 (2009), Vol. **74**, page 669:
– Line 2 from the bottom should read: “doi: 10.2298/JSC0906669M”.